WARSAW UNIVERSITY OF TECHNOLOGY

Faculty of Physics

Ph.D. THESIS

Barbara Trzeciak, M.Sc. Eng.

Polarization of hidden charm particles in relativistic proton-proton collisions measured in the STAR experiment

Supervisors

Professor Grażyna Odyniec, Ph.D.

Professor Jan Pluta, Ph.D., D.Sc.

Warsaw 2013

Streszczenie

Polaryzacja cząstek o ukrytym powabie w relatywistycznych zderzeniach proton-proton mierzona w eksperymencie STAR

Istnieje wiele różnych modeli produkcji cząstki J/ψ w zderzeniach proton-proton, które dobrze opisują mierzony w eksperymentach przekrój czynny na produkcję J/ψ. Dlatego potrzebna jest inna obserwabla pozwalająca na rozróżnienie pomiędzy różnymi modelami produkcji J/ψ. Taką obserwablą może być ustawienie spinu cząstki J/ψ, nazywane polaryzacją J/ψ, ponieważ różne modele przewidują różną zależność polaryzacji J/ψ od pędu poprzecznego (p_T).

Przewidywania modelu $NRQCD$, które zawierają wkład od stanów oktetu kolorowego, (COM) są w zgodzie z obserwowanym w eksperymentach widmem J/ψ p_T przy różnych energiach. Jednak model ten nie opisuje dobrze polaryzacji J/ψ zmierzonej przez eksperyment CDF w FermiLab przy energii zderzenia $\sqrt{s}$ = 1.96 TeV i dla wysokich pędów poprzecznych J/ψ. Dla niskich p_T model jest w zgodzie z pomiarem polaryzacji J/ψ w eksperymencie PHENIX przy energii zderzenia $\sqrt{s}$ = 200 GeV. Te pomiary nie są jednak rozstrzygająca, ponieważ dla niskich pędów poprzecznych modele Color Octet Model i Color Singlet Model mają podobne przewidywania.

Model NLO Color Singlet Model (CSM) przewiduje podłużną polaryzację J/ψ dla niskich i średnich pędów poprzecznych. Dla niskich p_T przewidywania jakościowo zgadzają się z pomiarami widma J/ψ p_T w eksperymentach przy RHIC. Ten model również dobrze opisuje polaryzację J/ψ zmierzoną w eksperymencie PHENIX dla niskich pędów poprzecznych.

Dla niskich p_T modele COM i CSM mają podobne przewidywania odnośnie polaryzacji J/ψ. Jednak wraz ze wzrostem pędu poprzecznego trend przewidywań modelu COM jest w kierunku poprzecznej polaryzacji J/ψ, natomiast model CSM przewiduje podłużną polaryzację, prawie niezależną od p_T. Szczególnie ważny jest więc pomiar polaryzacji J/ψ przy wysokich pędach poprzecznych, gdzie modele mają rożne przewidywania.

W niniejszej pracy przedstawiony jest opis pierwszego pomiaru polaryzacji J/ψ w eksperymencie STAR przy energii $\sqrt{s} = 200$ GeV, dla pośpieszności J/ψ z przedziału $|y| < 1$ i p_T z przedziału $2 < p_T < 6$ GeV/c. W analizie zostały użyte dane z roku 2009, triggerowane przez elektron z wysokim p_T. J/ψ jest rekonstruowane w elektronowym kanale rozpadu. Współczynnik rozkładu kątowego elektronów z rozpadu J/ψ (parametr polaryzacji) λ_θ jest wyznaczony w układzie odniesienia *helicity*, w funkcji pędu poprzecznego J/ψ. Kąt polarny θ jest kątem pomiędzy wektorem momentu pędu pozytonu, w spoczynkowym układzie odniesienia J/ψ, a wektorem pędu J/ψ w laboratoryjnym układzie odniesienia. Pomiar polaryzacji J/ψ w układzie odniesienia *helicity* pozwolił na porównanie otrzymanych wyników z przewidywaniami różnych modeli produkcji J/ψ, z modelem NLO^+ Color Singlet Model ($NLO^+\,CSM$) i z obliczeniami $NRQCD$ zawierającymi wkład od stanów oktetu kolorowego (COM).

Otrzymana polaryzacja J/ψ w funkcji pędu poprzecznego pokazuje trend w kierunku podłużnej polaryzacji wraz ze wzrostem p_T. Trend ten jest innymi niż w przewidywaniu modelu COM. Otrzymany wynik jest natomiast w zgodzie z przewidywaniem modelu $NLO^+\,CSM$, w ramach obecnych niepewności eksperymentalnych i teoretycznych.

Pomiar polaryzacji J/ψ przedstawiony w niniejszej pracy wyjaśnia nieco mechanizm produkcji J/ψ poprzez wyeliminowanie modelu COM. Analiza nowych danych z roku 2011 przy energii zderzenia $\sqrt{s} = 500$ GeV umożliwi dalsze postępy w rozróżnieniu pomiędzy różnymi modelami. Dane te mogą również umożliwić przeprowadzenie analizy pełnego rozkładu kątowego elektronów z rozpadu J/ψ. Warto również zaznaczyć, iż w celu wyciągnięcia precyzyjniejszych wniosków dotyczących mechanizmu produkcji J/ψ, niepewności przewidywań teoretycznych muszą być zmniejszone.

Abstract

Different models of the J/ψ production mechanism are able to describe the measured in experiments J/ψ production cross section rather well. Therefore other observable is needed to discriminate among different J/ψ production models. J/ψ spin alignment, commonly known as J/ψ polarization, can be used as such an observable since various models predict its different dependence on p_T.

The prediction of $NRQCD$ calculations with the color octet contributions (COM) is in good agreement with observed J/ψ p_T spectra in experiments at different energies but fails to describe the observed J/ψ polarization measured at $\sqrt{s} = 1.96$ TeV at high p_T in the CDF experiment at FermiLab. For low-p_T region, the model is in agreement with the PHENIX J/ψ polarization measurement at $\sqrt{s} = 200$ GeV. However, the PHENIX measurement is limited to small p_T, where the data are not able to distinguish between the Color Octet Model and Color Singlet Model predictions.

The NLO Color Singlet Model (CSM) predicts longitudinal J/ψ polarization in the helicity frame at low and mid p_T at mid-rapidity. The NLO CSM prediction for the p_T spectrum is in qualitatively agreement with RHIC data at low p_T but misses the higher p_T part. The prediction for the J/ψ polarization from this model is in good agreement with the PHENIX data, which are only for low p_T.

For lower p_T COM and CSM models have similar predictions of longitudinal J/ψ polarization. But with increasing p_T a trend of the COM model is towards the transverse polarization while the CSM predicts longitudinal polarization with almost no p_T dependence. Thus, it is especially important to measure the J/ψ polarization at higher p_T, where CSM and COM predict different polarization.

In this thesis, the first J/ψ polarization measurement in the STAR experiment at RHIC, in $p + p$ collisions at $\sqrt{s} = 200$ GeV at $|y| < 1$ and in p_T range $2 < p_T < 6$ GeV/c, is reported. The analysis is done using data from 2009 year, with a high-p_T electron trigger. The J/ψ is re-

constructed via its di-electron decay channel. The angular distribution coefficient (polarization parameter) λ_θ of the J/ψ decay into electrons is extracted in the helicity frame as a function of J/ψ p_T. The polar angle θ is defined as an angle between the positron's momentum vector in the J/ψ rest frame and J/ψ momentum vector in the laboratory frame. The measurement of λ_θ in the helicity frame allow us compare the measured J/ψ polarization with different model predictions of the J/ψ production: NLO^+ Color Singlet Model (NLO^+ CSM) and $NRQCD$ calculations with the color octet contributions (COM).

Our analysis of the J/ψ polarization in the helicity frame indicates a trend towards the longitudinal J/ψ polarization as p_T increases. It is in contrary to the prediction of the COM model. The result is consistent with the prediction of NLO^+ CSM model, within the current experimental and theoretical uncertainties.

The J/ψ polarization analysis, that is presented in the thesis, sheds already some light on the J/ψ production mechanisms by elimination of the COM mechanism. Further progress in distinguishing between the J/ψ production mechanisms may be possible with analysis of a newer data at $\sqrt{s} = 500$ GeV, taken in 2011 with much higher luminosity. This data may also allow to perform analysis of the full angular distribution. On the theoretical side, one needs to stress that the uncertainties of the models need to be reduced in order to draw more precise conclusions.

Contents

List of Figures

List of Tables

Chapter 1

Theoretical motivation

Quarkonia production in high-energy hadron collisions allows to investigate the Quantum Chromodynamics.

Initial tests of quarkonia production mechanisms using cross section measurements are inconclusive since different models have similar predictions regarding the cross-section. It suggests that other observables are needed to discriminate among the models. The quarkonia spin alignment, commonly named as polarization, provide a very important information that may help to pin down the mechanism of heavy quarkonia production and the bound state formation.

In this chapter we will briefly introduce the Standard Model and its theory of the strong interactions, Quantum ChromoDynamics (QCD). Then, we will show a method of the J/ψ polarization extraction in the experiment. Finally, different models of the J/ψ production will be discussed, along with their predictions regarding the cross section and polarization.

1.1 Standard Model and Quantum Chromodynamics

1.1.1 Standard Model

The Standard Model of the particle physics contains description of all known fundamental particles and their interaction via three, out of the four, known forces of nature: electromagnetism, the weak force and the strong force. The gravity is not included in the model. Particles described within the Standard Model are: fermions with spin 1/2, gauge bosons with spin 1, and Higgs boson with spin 0.

There is three generations of fermions, which are matter particles. Each of them contain two quarks, one lepton and a neutrino, see Fig. 1.1. Each fermion has a corresponding antipar-

Figure 1.1: Elementary particles in the Standard Model.

ticle. Gauge bosons are force carriers that mediate fundamental interactions. A very successful quantum field theory of the electromagnetic (EM) interactions, the Quantum Electrodynamics (QED), describes the electromagnetic force between charged fermions as the exchange of massless photons. Massive $W^{\pm}$ and Z^0 gauge bosons mediate the weak interaction between particles of different flavors. The electromagnetic and weak forces are described in the unified framework of the electroweak model. The Strong interaction between color charged particles is mediated by gluons, that themselves have a color charge. The strong interactions are described by a theory called Quantum Chromodynamics. The hypothesized Higgs boson [5] is a consequence of a spontaneous symmetry breaking. The particle is linked to a mechanism that gives mass to elementary particles. Lately, the Higgs boson existence was tentatively confirmed by the LHC experiments [6].

1.1.2 Quantum Chromodynamics

Quantum Chromodynamics (QCD) [1, 2] describes, within the Standard Model, the strong interaction of colored quarks and gluons. Since massless gluons carry the color charge they can interact also with each other. QCD is an extension of QED, it is a non-abelian gauge quan-

tum field theory, and it is the $SU(3)$ component of the $SU(3) \times SU(2) \times SU(1)$ Standard Model of the particle physics. Quarks are color triplets, with three colors: red, green and blue. Anti-quarks have analogous anti-colors. Gluons are color octets.

The quark-gluon potential has a form:

$$V_s = -\frac{4}{3}\frac{\alpha_s}{r} + kr, \tag{1.1}$$

where r is a distance between quarks, α_s is (running) coupling constant and $k \sim 1 \, \text{GeV}/fm$ [2]. The value of α_s depends on the energy scale of a studied process, it decreases with increasing four momentum Q^2 transferred in the interaction.

Two important properties of the QCD are: asymptotic freedom and confinement. Asymptotic freedom refers to the weakness of the short-distance interaction, while the confinement of quarks follows from its strength at long distances.

Confinement

Free quarks are not observed in the nature. They are confined in hadrons, barions (qqq) or mesons ($q\bar{q}$). At large r, the kr term becomes dominant. When one try to separate quarks by pulling them apart, the gluon field forms a string of the color field between them. With increasing r energy in the system increases, and at some point it is energetically more favourably to create a new pair of quarks, $q\bar{q}$, than to allow the string to extend further.

Asymptotic freedom

For large Q^2, $\alpha_s(Q) \to 0$, and for small distances the first Coulomb-like part of Eq. 1.1, $-\frac{4}{3}\frac{\alpha_s}{r}$, becomes dominant. As a consequence, at large energies or on small distances, bonds between quarks are asymptotically weak and quarks act like free particles. If the coupling constant is small, $\alpha_s \ll 1$, perturbative calculations can be applied. The perturbative QCD successfully describes hard processes (with high momentum transfer) in high energy collisions, for example production of $c\bar{c}$ pairs in a hard scattering.

At low-energy regime, $Q \lesssim 1 \, \text{GeV}$, the coupling is so strong that the perturbation theory breaks down. The QCD is facing difficulties associated with non-perturbative calculations of soft process (with small momentum transfer), such as hadronization. To solve some of the mathematical difficulties, other techniques have to be developed, e.g. the lattice QCD or effective theories.

1.1.3 Summary

The Standard Model developed in early 1970s, successfully explains most of experimental results and precisely predicted a wide variety of phenomena. Over time the Standard Model has become a well established and tested physics theory. In this section, a brief description of the Standard Model and the Quantum Chromodynamics, was presented. It is used to describe the J/ψ meson and models of its production mechanisms in hadron collisions. The calculations and predictions regarding various J/ψ properties are based on the Quantum Chromodynamics, as the formation of $c\bar{c}$ pairs can be described using the perturbative QCD.

1.2 J/ψ meson

In this work, we will focus on the J/ψ meson. J/ψ is a charmonium [7] (a hidden charm particle), i.e. bound state of a charm quark (c) and its antiquark ($\bar{c}$). The bound states of a heavy quark Q and its antiquark $\bar{Q}$ are generally referred to as quarkonia.

The first charmed particle, J/ψ, was discovered in November 1974, simultaneously by Samuel Ting et al. at BNL [9] (J) and Burton Richter et al. at SLAC [10] (ψ). They were both awarded the Nobel prize in 1976 for the discovery. The impact of this discovery on the particle physics was so important that is known as the *November Revolution*. The existence of the fourth quark[1] had been speculated by Bjorken and Glashow in 1964 [11]. The charm quark was also predicted in 1970 by the Glashow, Iliopoulos and Maiani. It was required by the Glashow, Iliopoulos and Maiani (GIM) mechanism [12], in order to cancel the anomaly in week decays. And the prediction of the charm quark is usually credited to them.

The various charmonia states differ in their total angular momentum (J), parity (P), charge conjugation (C), and principal quantum number (n). The most abundantly produced charmonium is J/ψ. It is a heavy and "sharp" resonant state, with the width of (92.9±2.8)keV [1], and mass approximately 3.1 GeV. The J/ψ is a vector meson in an s-wave orbital state, and its quantum numbers are the same as those of the photon, $J^{PC} = 1^{--}$. Its isospin is 0 and G-parity is -1. The spectroscopic arrangement of the charmonium family is shown in Fig. 1.2, and properties of different charmonia states are gathered in Tab. 1.1.

Main J/ψ decay modes, with their Branching Ratios (BR), are [1]:

- $J/\psi \longrightarrow hadrons \quad BR = (87.7 \pm 0.5)\%$

---

[1] u, d and s quarks had been known before

- $J/\psi \longrightarrow e^+e^-$ $BR = (5.94 \pm 0.06)\%$

- $J/\psi \longrightarrow \mu^+\mu^-$ $BR = (5.93 \pm 0.06)\%$
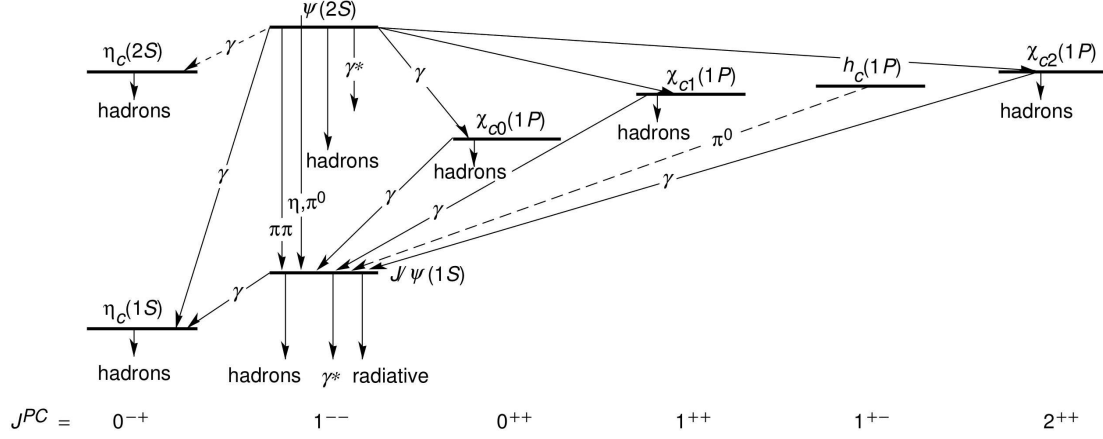
Figure 1.2: Spectrum and transitions of the charmonium family [4].

Meson	$n^{2S+1}L_J$	J^{PC}	Mass (MeV)
η_C	$1\,^1S_0$	0^{-+}	2981.0 ± 1.1
J/ψ	$1\,^3S_1$	1^{--}	3096.916 ± 0.011
χ_{C0}	$1\,^3P_0$	0^{++}	3414.75 ± 0.31
χ_{C1}	$1\,^3P_1$	1^{++}	3510.66 ± 0.07
χ_{C2}	$1\,^3P_2$	2^{++}	3556.20 ± 0.09
h_C	$1\,^1P_0$	1^{+-}	3524.41 ± 0.16
$\eta_C(2S)$	$2\,^1S_0$	0^{-+}	3638.9 ± 1.3
ψ'	$2\,^3S_1$	1^{--}	$3686.108^{+0.011}_{-0.014}$

Table 1.1: Properties of charmonia [1].

The mentioned charmonium states are stable bound states. They are stable in a sense that their mass is less than that of two light-heavy mesons[2], so that strong decays into open charm are forbidden [8]. The mass of ψ' is just below the open charm threshold. Charmonium states that are above the ψ' can decay into $D\bar{D}$ pairs.

Quarkonium masses are largely determined by the bar quark masses. Due to large masses of those quarks, many basic quarkonium properties can be calculated using a non-relativistic potential theory [13].

---

[2]open charm mesons (D) contain charm quark (or antiquark) and light antiquark (or quark)

The Cornell confining potential [14] gives a good description of the observed charmonium bound states. The potential for a $Q\bar{Q}$ pair at separation distance r is:

$$V(r) = \sigma r - \frac{\alpha}{r}, \tag{1.2}$$

where σ is a string tension and α is a gauge coupling ($\alpha = \frac{4}{3}\alpha_s$). Ground states at the lower excitation levels of quarkonia are very tightly bound, and much smaller than the light hadrons.

Many of the J/ψ mesons observed at colliders are not directly produced from collisions but are a result of decays from heavier charmonium states or from B meson decays. The direct J/ψ production, which is found to be about 60% (59$\pm$10% [28]) of observed J/ψ, plus feed-down from heavier charmonium states, ψ' and χ_C, is called a prompt production. ψ' and χ_C account for about 10% and 30% of the prompt production, respectively. Estimations from different experiments are slightly different. The contribution from ψ' feed-down is 8.6$\pm$2.5% or 8.1$\pm$0.3% from PHENIX experiment [15] and from fixed-target experiments [16], respectively. χ_C accounts for 30$\pm$6 or 25$\pm$5 from CDF experiment [17] and from fixed-target experiments [16], respectively. The inclusive J/ψ production also contains the contribution from B meson decays, non-prompt J/ψ. It is strongly p_T dependent, and according to new STAR measurements, in hadron collisions at $\sqrt{s} = 200$ GeV the contribution from the B meson decay is 10-25% of the observed J/ψ, for $4 < p_T < 12$ GeV/c [18].

1.3 J/ψ **polarization**

The topic of this dissertation is the J/ψ polarization. A particle produced in a certain superposition of elementary mechanisms may be observed preferentially in a state belonging to a definite subset of the possible eigenstates of the angular momentum component J_z along the characteristic quantization axis. When this happens, the particle is said to be polarized [19].

A nomenclature used for the polarization of vector mesons is an analogy to the photon polarization, since these particles share the quantum numbers of the photon. The transverse polarization means that the spin projection is $J_z = \pm 1$, and $J_z = 0$ is for the longitudinal polarization. The same terms are used do describe the *spin alignment* of vector quarkonia not only with respect to their own momenta (HX frame), but also with respect to any other chosen reference frame (GJ or CS frames) [19].

For the J/ψ decay, the geometrical shape of the angular distribution of the two decay leptons, in the J/ψ rest frame, reflects the polarization of the J/ψ. A spherically symmetric distribution

would mean that the J/ψ is on average unpolarized, an anisotropic distribution would mean that the J/ψ is polarized. Figure 1.3 shows dilepton decay distribution of transversely (a) and longitudinally (b) polarized J/ψ in the *natural* frame (polarization axis z coincides with the $\vec{J}$).
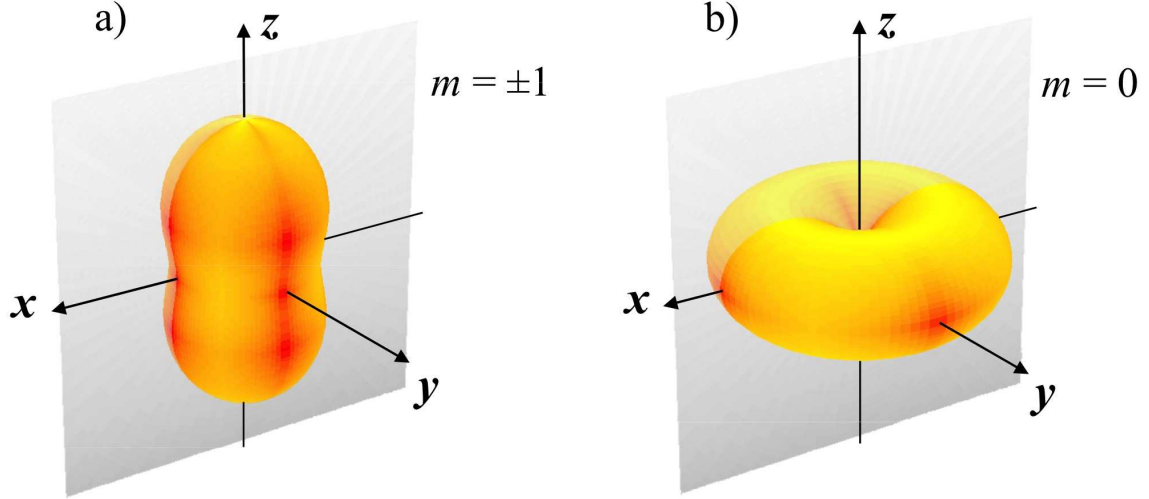
Figure 1.3: Representation of the dilepton decay distribution of transversely (a) and longitudinally (b) polarized J/ψ in the *natural* frame. The probability of the lepton emission in one direction is represented by the distance of the corresponding surface point from the origin. [19]

In an experiment, the coordinate system used for the J/ψ polarization studies, has to be defined. Figure 1.4 shows possible definition of the coordinate system, as seen from the J/ψ rest frame. The z axis is the polar axis, which depends on the chosen reference frame. The x axis lies on the production plane xz ($x = y \times z$), which contains momenta of colliding beams, and the y is the production plane normal. The polar angle, θ, is defined as the angle between momentum of a lepton from the J/ψ decay (usually it is l^+) in the J/ψ rest frame and the chosen polar axis z. The azimuthal angle, ϕ, is determined by the production plane.

1.3.1 Reference frames

There are three reference frames that are usually used for the J/ψ polarization measurements: helicity [58], Collins-Soper [59] and Gottfried-Jackson [60] frames. In all frames the polarization axis z belongs to the production plane (xz). Figure 1.5 shows the production plane definition on the left-hand side, and definitions of the polarization axis z in different rest frames are shown on the right-hand side of the Fig. 1.5
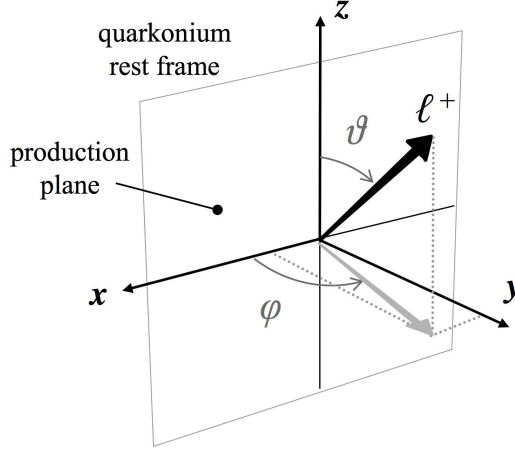
Figure 1.4: Representation of the coordinate system for the J/ψ polarization measurement, in the J/ψ rest frame. [19]
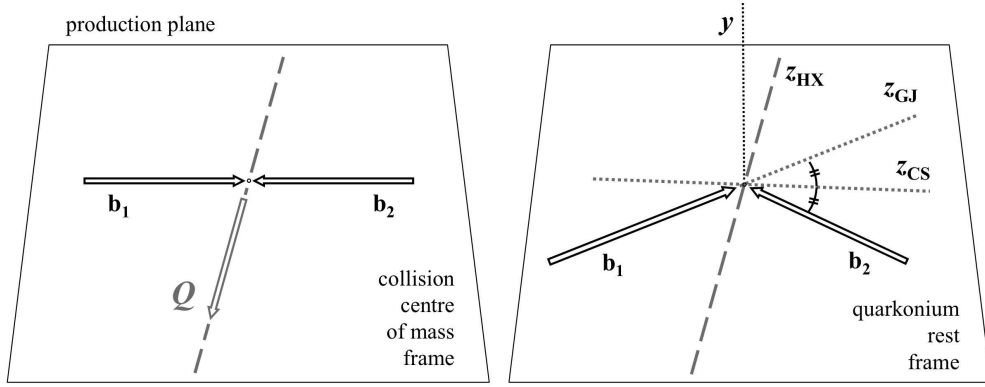
Figure 1.5: Definition of the production plane (left) and definitions of the polarization axis z in helicity (HX), Collins-Soper (CS) and Gottfried-Jackson (GJ) reference frames (right). [19]

In the helicity frame (HX) the z axis is along the J/ψ momentum in the center of mass frame. The Collins-Soper frame (CS) defines the z axis as a bisector of the angle formed by one beam direction and the opposite direction of the other beam, in the J/ψ rest frame:

$$z = \frac{\overrightarrow{P_b}}{|P_b|} - \frac{\overrightarrow{P_a}}{|P_a|}, \tag{1.3}$$

where $\overrightarrow{P_a}$ and $\overrightarrow{P_b}$ are the 3-momenta of each beam boosted into the J/ψ rest frame. In the Gottfried-Jackson frame (GJ), the polarization axis is chosen along the momentum vector of one beam boosted into the J/ψ rest frame.

In collider experiments, HX frame is usually used. Recently, also the CS[3] frame has been used in some collider experiments. The GJ frame is mostly applied in the fixed target experi-

---

[3]the CS frame was initially motived by Drell-Yan production

ments.

1.3.2 Decay angular distribution

The J/ψ polarization can be determined experimentally by measuring the dilepton decay angular distribution. The decay angular distribution can be derived from the J/ψ production density matrix using basic conservation rules, such as the parity conservation.

The information on the production polarization of the J/ψ meson is contained in the spin density matrix ρ:

$$\rho = \begin{pmatrix} \rho_{11} & \rho_{10} & \rho_{1-1} \\ \rho_{01} & \rho_{00} & \rho_{0-1} \\ \rho_{-11} & \rho_{-10} & \rho_{-1-1} \end{pmatrix} \tag{1.4}$$

The matrix is Hermitian and satisfies $Tr(\rho) \equiv \rho_{11} + \rho_{00} + \rho_{-1-1} = 1$. ρ_{00} it the longitudinal polarization fraction and $(\rho_{11} + \rho_{-1-1})$ is the transverse fraction. Using parity conservation rules: $\rho_{-1-1} = \rho_{11}$, $\rho_{-11} = \rho_{1-1}$, $\rho_{-10} = -\rho_{10}$ and $\rho_{0-1} = -\rho_{01}$. So there are only four independent real parameters in ρ, and a convenient set is:

$$\rho = \begin{pmatrix} \rho_{11} & Re(\rho_{10}) + iIm(\rho_{10}) & \rho_{1-1} \\ Re(\rho_{10}) - iIm(\rho_{10}) & 1 - 2\rho_{11} & -Re(\rho_{10}) + iIm(\rho_{10}) \\ \rho_{1-1} & -Re(\rho_{10}) - iIm(\rho_{10}) & \rho_{11} \end{pmatrix} \tag{1.5}$$

Let us assume, for a simplicity of the notation, that we have a two-body decay, $\gamma \longrightarrow \alpha + \beta$. The particle γ is in eigenstate j of the total angular momentum and eigenstate m of the magnetic sub-state. Particle α and β have momenta $\overrightarrow{p}$ and $-\overrightarrow{p}$ in the γ rest frame, and they helicities are λ_α and λ_β. z and x axis are in the production plane. The derivation of the angular distribution is based on [61].

The decay state, expanded into angular momentum eigenstates of γ is:

$$|\widehat{p}\lambda_\alpha\lambda_\beta\rangle = \sum_{j,m} |jm\lambda_\alpha\lambda_\beta\rangle \sqrt{\frac{2j+1}{4\pi}} D^{j*}_{m\lambda}(\phi, \theta, \phi), \tag{1.6}$$

where $\widehat{p}$ is a unity vector in the direction of $\overrightarrow{p}$, $\lambda = \lambda_\alpha - \lambda_\beta$, $D^j_{m\lambda}$ are *Wigner D-matrices* corresponding to matrix elements $\langle jm'|R(\phi, \theta, \psi)|jm\rangle$ of the rotation operator $R(\phi, \theta, \psi)$. The three Euler angles, ϕ, θ and ψ specify the direction of $\widehat{p}$. Wigner D-matrices written in therms of real-value d-functions:

$$D^j_{m,\lambda}(\phi, \theta, \psi) = e^{-im\phi} d^j_{m\lambda}(\theta) e^{-i\lambda\psi} \tag{1.7}$$

and:

$$d^j_{mm'} = (-1)^{m-m'} d^j_{mm'} = d^j_{-m-m'} \tag{1.8}$$

The amplitude of the decay is:

$$A_m(\widehat{p}, \lambda_\alpha, \lambda_\beta) = \langle \widehat{p}\lambda_\alpha\lambda_\beta | \widehat{U} | jm \rangle, \tag{1.9}$$

where $\widehat{U}$ is operator invariant under rotations and reflections. Using Eq. 1.6:

$$A_m(\widehat{p}, \lambda_\alpha, \lambda_\beta) = \sqrt{\frac{2j+1}{4\pi}} M(\lambda_\alpha, \lambda_\beta) D^j_{m\lambda}(\phi, \theta, \psi), \tag{1.10}$$

where $M(\lambda_\alpha, \lambda_\beta) = \langle jm\lambda_\alpha\lambda_\beta | \widehat{U} | jm \rangle$

The probability for $\gamma \longrightarrow \alpha + \beta$ with $\widehat{p}$ specified by Euler angles ϕ, θ and ψ in the γ rest frame:

$$\frac{d\sigma}{d^4q d\Omega} = \frac{2j+1}{4\pi} \sum_{m,m'} \sum_{\lambda_\alpha,\lambda_\beta} A_m(\widehat{p}, \lambda_\alpha, \lambda_\beta) \rho_{mm'} A^*_{m'}(\widehat{p}, \lambda_\alpha, \lambda_\beta)$$
$$= \frac{2j+1}{4\pi} \sum_{m,m'} \sum_{\lambda_\alpha,\lambda_\beta} |M(\lambda_\alpha, \lambda_\beta)|^2 D^{j*}_{m\lambda}(\phi, \theta, \psi) D^j_{m'\lambda}(\phi, \theta, \psi) \rho_{mm'} \tag{1.11}$$

J/ψ is spin-1 particle with $m = 0$, the helicity conservation requires $\lambda_\alpha \neq \lambda_\beta$, and for decay leptons, λ_α and λ_β can be either $\frac{1}{2}$ or $-\frac{1}{2}$. Also:

$$d^1_{11}(\theta) = \frac{1 - cos\theta}{2}, \quad d^1_{10}(\theta) = \frac{-sin\theta}{\sqrt{2}}, \quad d^1_{1-1}(\theta) = \frac{1 - cos\theta}{2} \tag{1.12}$$

The full amplitude can be written as:

$$\frac{d\sigma}{d^4q d\Omega} = \frac{3}{4\pi} |M(\frac{1}{2}, -\frac{1}{2})|^2 \{\rho_{11}(1 + cos^2\theta) + (1 - 2\rho_{11})(1 - cos^2\theta)$$
$$+ Re(\rho_{10})\sqrt{2}sin(2\theta)cos\phi + \rho_{1-1}sin^2\theta cos(2\phi)\} \tag{1.13}$$

The cross-section is parametrized as:

$$\frac{d\sigma}{d^4q d\Omega} = \frac{3}{4\pi} |M(\frac{1}{2}, -\frac{1}{2})|^2 \{W_T(1 + cos^2\theta) + W_L(1 - cos^2\theta)$$
$$+ W_\triangle \sqrt{2}sin(2\theta)cos\phi + W_{\triangle\triangle}sin^2\theta cos(2\phi)\} \tag{1.14}$$

W_T and W_L are the transverse and longitudinal components, respectively. W_T corresponds only to the ρ_{11} and ρ_{-1-1} elements of the density matrix, and W_L corresponds to the ρ_{00} element. $W_\triangle$ and $W_{\triangle\triangle}$ are called the *single-spin flip* and *double-spin flip* components, respectively.

Decay angular coefficients

The angular distribution can be written as:

$$\frac{d\sigma}{d(cos\theta)d\phi} \propto 1 + \lambda_\theta cos^2\theta + \lambda_{\theta\phi}sin(2\theta)cos\phi + \lambda_\phi sin^2\theta cos(2\phi), \tag{1.15}$$

where

$$\begin{aligned}
\lambda_\theta &\equiv \frac{W_T - W_L}{W_T + W_L} = -\frac{1 - 3\rho_{11}}{1 - \rho_{11}} \\
\lambda_{\theta\phi} &\equiv \frac{\sqrt{2}W_\triangle}{W_T + W_L} = \frac{\sqrt{2}Re(\rho_{10})}{1 - \rho_{11}} \\
\lambda_\phi &\equiv \frac{2W_{\triangle\triangle}}{W_T + W_L} = \frac{2\rho_{1-1}}{1 - \rho_{11}}
\end{aligned} \tag{1.16}$$

the λ_θ parameter is often called the polarization parameter. Following constraints can be put on the parameters: $|\lambda_\theta| < 1$, $|\lambda_{\theta\phi}| < \frac{\sqrt{2}}{2}$, $|\lambda_\phi| < 0.5$ for $\lambda_\theta = 0$ and $\lambda_\phi \to 0$ for $\lambda_\theta \to -1$ [65].

The angular distribution coefficients can be extracted form 1-dimensional distributions. The angular distribution integrated over ϕ:

$$W(cos\theta) \propto 1 + \lambda_\theta cos^2\theta \tag{1.17}$$

And the distribution integrated over θ:

$$W(\phi) \propto 1 + \frac{2\lambda_\psi}{3 + \lambda_\theta}cos(2\phi) \tag{1.18}$$

The diagonal term, $\lambda_{\theta\phi}$, vanishes in both integrations, but can be extracted by defining variable $\tilde{\phi}$:

$$\tilde{\phi} = \begin{cases} \phi - \frac{3}{4}\pi & \text{for } cos\theta < 0 \\ \phi - \frac{1}{4}\pi & \text{for } cos\theta > 0 \end{cases} \tag{1.19}$$

The $W(\tilde{\phi})$ distribution is:

$$W(\tilde{\phi}) \propto 1 + \frac{\sqrt{2}\lambda_{\theta\phi}}{3 + \lambda_\theta}cos\tilde{\phi} \tag{1.20}$$

In general, $\lambda_\theta = -1$ means full longitudinal polarization and $\lambda_\theta = 1$ full transverse polarization.

Frame invariant approach

In an experiment, the *natural* polarization axis is unknown, and a measured polarization depends on the observable frame. As is was argued by P. Faccioli et al. [19, 62, 63, 64, 65], the chosen

polarization axis has a radical effect of the magnitudes and signs of the angular distribution coefficients. Therefore, in order to investigate the J/ψ polarization and understand its origin, without depending on a model, both the polar and azimuthal distributions with their kinematic dependence have to be determined. Also, it is the best if they are measured in at least two geometrically complementary reference frames. HX and CS frames are orthogonal (the frames differ by a 90°rotation around the y axis) when J/ψ is produced at high p_T and has a negligible longitudinal momentum ($p_T \gg |p_L|$).

For that purpose, a frame invariant approach has been developed. An frame-invariant quantity, $\tilde{\lambda}$, was proposed:

$$\tilde{\lambda} = \frac{\lambda_\theta + 3\lambda_\phi}{1 - \lambda_\phi} \tag{1.21}$$

Any arbitrary choice of the experimental observation frame will always give the same value of $\tilde{\lambda}$, independently of kinematics. Since this quantity is also less acceptance dependent, than the standard anisotropy parameters λ_θ, λ_ϕ and $\lambda_{\theta\phi}$, it can be used to directly compare the polarization measurement in different experiments.

1.4 J/ψ production

J/ψ hadroproduction proceeds through two stages. First, a $c\bar{c}$ pair is produced in a hard scattering of partons. The process is described by the perturbative QCD. This is followed by a hadronization process in which physical resonance, such as J/ψ is formed. J/ψ bound state is produced via color-singlet [4] or color-octet [5] intermediate state. Based on the different production mechanisms, theoretical models of the J/ψ production can be divided into three main groups, namely: Color Single Model, Color Evaporation Model and Non-Relativistic QCD calculations with color-octet components, which are described in next sub-sections.

Tests of the J/ψ production mechanism that use the measured J/ψ cross-sections are inconclusive since different models have similar predictions for the cross-section. Measurements of the J/ψ polarization may help to distinguish between the models. Competing mechanisms domination in the different theoretical approaches lead to very different expected polarizations of the quarkonia produced in the high-energy hadron collisions.

---

[4]color-singlet is a colorless state

[5]color octet is a coloured state

1.4.1 Color Singlet Model

The Color Singlet Model (CSM) is an application of QCD to heavy-quarkonium production in the high-energy regime [20, 21]. In this model the only input, apart from the PDF [6], is a wave function which can be determined from data or calculated from potential models.

The production of a charmonium is divided into two processes that can be factorized. In the first one, two on-shell heavy quarks (c and $\bar{c}$) are created, then they are bounded and form the meson. The first process is perturbative (of a scale of approximately $M^2 + p_T^2$) with the cross section computable from the Feynman-diagrams. In high-energy hadronic collisions, the leading contribution comes from a gluon fusion process. Feynman diagrams for the $^3S_1$ states production associated with a gluon are shown in Fig.1.6. If the perturbative amplitude to produce the heavy-quark pair on shell ($M(p)$) is calculated at the leading order in α_s, it refers to Leading Order CSM (LO CSM). It is assumed that charmonium's quarks are created at rest in the meson frame (static approximation) and that the color and the spin of the $c\bar{c}$ pair do not change during the binding. It is also required that the pair is produced in a color-singlet state, since physical states are colorless.
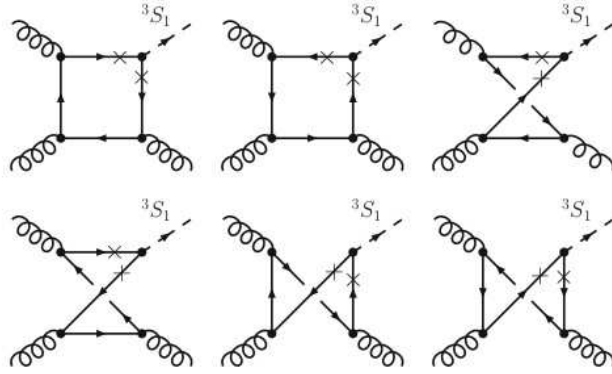
Figure 1.6: Diagrams for $gg \to^3 S_1 g$ at LO within the CSM [20].

The LO CSM prediction for the J/ψ cross section is more than order of magnitude below the CDF experiment measurements[23] . Figure 1.7 shows differential cross section as a function of p_T measured in the CDF experiment compared to predictions of LO CSM and LO CSM including the fragmentation processes [22]. Addition of the fragmentation improves the high-p_T part. This disagreement between the theoretical predictions and experimental results has led to further improvements of the CSM model and to development of new models, for example

---

[6]the Parton Distribution Function

with color-octet contributions.
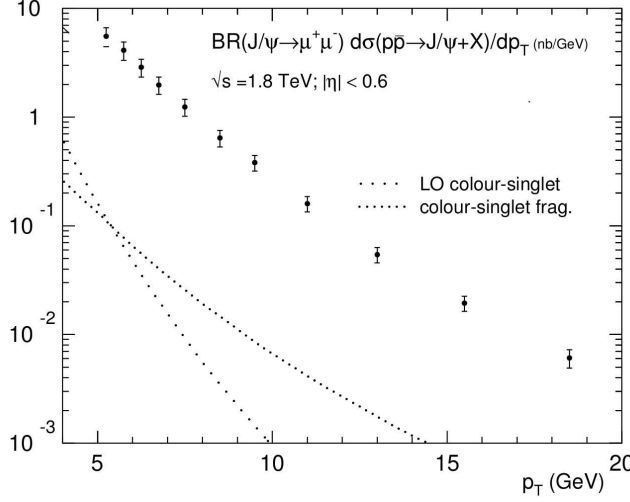
Figure 1.7: Differential cross-section as a function of p_T of the CSM (LO and fragmentation) compared with the direct production of J/ψ from CDF [20].

Next-to-leading Order (NLO) QCD corrections to color-singlet quarkonium production [24] show an important enhancement of the cross section, especially at high p_T, see Fig. 1.9. Also, CSM with s-channel cut contribution (off-shell quarks in the bound state) was proposed [25] [26].

It is now accepted that α_s^4 and α_s^5 corrections to the CSM are essential for understanding the J/ψ p_T spectrum in high-energy hadron collisions [27]. The predictions at LO and NLO accuracy are sufficient to account for the observed magnitude of the p_T-integrated cross section [28] (see Fig. 1.8), however the NLO CSM under-predicts the cross section differential in p_T and the slope is too steep (see Fig. 1.9) [27]. Figure 1.9 also shows a newer CSM model prediction, NNLO*, which is in a much better agreement with the RHIC data for $p_T > 5$ GeV/c. This calculations include contributions from gg and gq fusion at NLO (up to α_s^4), cg fusion at LO (at α_s^3) and the leading p_T contributions from gg and gq fusion at α_s^5 (NNLO*) [27]. Since the CSM predictions are for direct J/ψ production, PHENIX and STAR inclusive J/ψ production data shown in Fig. 1.9 are multiplied by the expected fraction of direct J/ψ (59 $\pm$ 10)% [28].

The J/ψ polarization in the helicity frame is drastically modified at NLO, comparing to LO CSM predictions. At LO J/ψ is predicted to have transverse polarization, which is in disagreement with measurements of CDF [35] and PHENIX [32] experiments. In NLO calculations, the polarization is increasingly longitudinal with increasing p_T ($J_z = 0$), along the J/ψ momentum direction [27]. The most recent NLO$^+$ CSM prediction for the polarization of prompt J/ψ ,
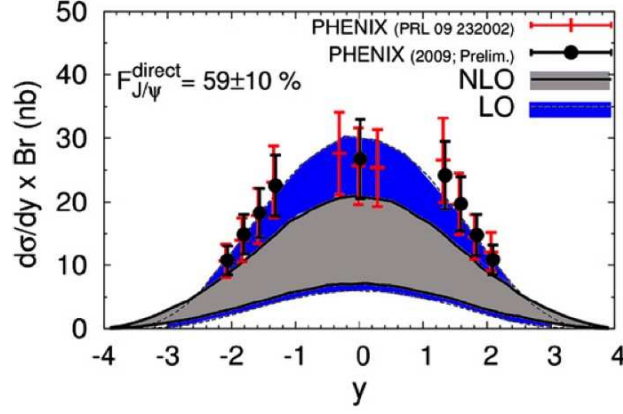
Figure 1.8: $d\sigma/dy \times Br$ in p+p collisions at $\sqrt{s} = 200\,\text{GeV}$ from CSM at LO and NLO accuracy [27] compared to the PHENIX data [29][30].
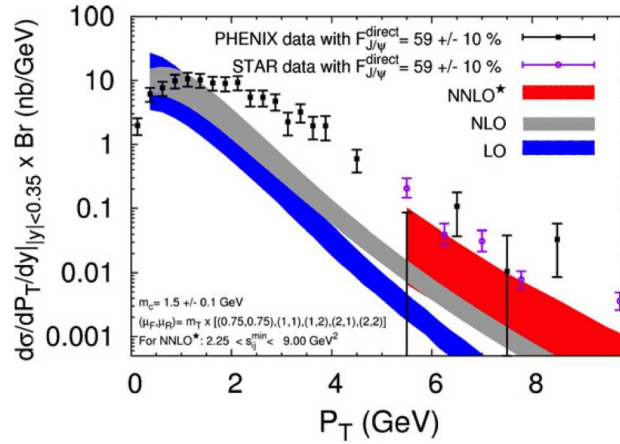
Figure 1.9: $d\sigma/dp_T \times Br$ in p+p collisions at $\sqrt{s} = 200$ GeV and $|y| < 0.35$ from CSM at various orders of α_s [27] compared to the PHENIX [29] and STAR [31] data.

which is shown in Fig. 1.10, is consistent with the PHENIX polarization measurement at low p_T. The NLO$^+$ contains the yield at NLO accuracy from gg and gq fusion added to the yield from cg fusion at LO accuracy. This calculation does not include all contributions which may influence the polarization. gg and gq fusion at NNLO* and cg fusion at LO (or NLO*) at large p_T could influence the yield, and the polarization may end up to be strongly longitudinal or slightly transversal. But, in contrary to the NRQCD calculations with color-octet transitions, the polarization in the CSM is not expected to become strongly transverse with increasing p_T [27].
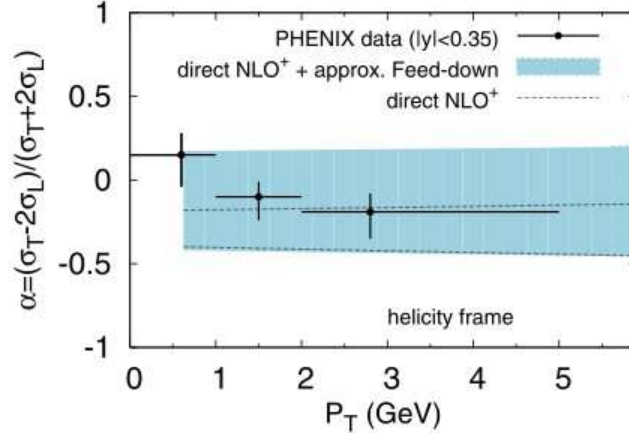
Figure 1.10: Comparison between the extrapolation of α (λ_θ) for prompt J/ψ in p+p collisions at $\sqrt{s} = 200$ GeV (blue band), the range of α for the direct NLO$^+$ (two dashed lines) [27] and the PHENIX measurements at mid-rapidity [32].

1.4.2 Non-Relativistic QCD calculations with color-octet mechanism

Non-Relativistic Quantum Chromodynamic (QCD) [40, 41, 42, 43, 44, 45] is an effective field theory. In this formalism intermediate $c\bar{c}$ color-octet states, in addition to color-singlet states, can bind to form the charmonium. The transition from the intermediate color-octet state to the final color-singlet state is possible by emitting a low energy gluon. The theory is based on a systematic expansion in both α_s and v (v is a quark velocity within the bound state, $v_c^2 \approx 0.23$). The important quantity of the formalism, is the factorization between the short-distance, perturbative contributions and the hadronization of $c\bar{c}$ described by non-perturbative matrix elements defined within NRQCD [20]. J/ψ production cross section associated with some hadron X is [20, 21]:

$$d\sigma(J/\psi + X) = \sum_n d\widehat{\sigma}(c\bar{c}[n] + X)\langle O_n^{J/\psi}\rangle, \tag{1.22}$$

where $d\widehat{\sigma}$ is the inclusive cross section for producing the $c\bar{c}$ pair in the color and angular momentum state n. $\langle O_n^{J/\psi}\rangle$ are the long distance matrix elements (LDME), which take account of the transition between the $c\bar{c}$ pair and the final physical state of J/ψ. The $\langle O_n^{J/\psi}\rangle$ parameters are determined in powers of v. In principal, there is unlimited number of the matrix elements with various values of n, but in calculations only the matrix elements at small powers of v are considered. The Fock-state decomposition of the J/ψ state, in powers of v is:

$$|J/\psi\rangle = O(1)|c\bar{c}[^3S_1^{(1)}]\rangle + O(v)|c\bar{c}[^3P_J^{(8)}]g\rangle + O(v^2)|c\bar{c}[^3S_0^{(8)}]g\rangle$$
$$+ O(v^2)|c\bar{c}[^3S_1^{(1,8)}]gg\rangle + O(v^2)|c\bar{c}[^3D_J^{(1,8)}]gg\rangle + \cdots^7 \tag{1.23}$$

34

There are color-singlet and color-octet LDME. The color-singlet ones are fixed by theory and can be find from the factorization formalism. They approximately represent the probability that perturbatively produced quark pair will evolve into the considered physical bound state. This part of the J/ψ production is described in CSM as well. The color-octet LDME give the probability of a transition between intermediate color-octet states, $^1S_0^{(8)}$, $^3P_0^{(8)}$, $^1S_1^{(8)}$, and the final color-singlet $^3S_1$ state. This elements are not known and have to be determined from a fit to the data. More details on the LDME can be found here [20]. For hadron collisions at high energy and at large p_T color-octet diagrams dominate for the J/ψ production, that is why the model is often called Color Octet Model (COM).

The NRQCD is in good agreement with measured J/ψ cross section. But one shall remember that the color-octet matrix elements are fit to reproduce the observed cross section as a function of p_T. NLO NRQCD calculations [53] successfully describe the J/ψ cross-section measured in the CDF experiment at $\sqrt{s} = 1.96$ TeV [54], as it is shown in Fig. 1.11. The model is also in agreement with measurements at lower energy of $\sqrt{s} = 200$ GeV, from STAR [34, 18] (calculations taken from [55]) and PHENIX [33] (calculations taken from [56]) experiments, see Fig. 1.12 and 1.13.
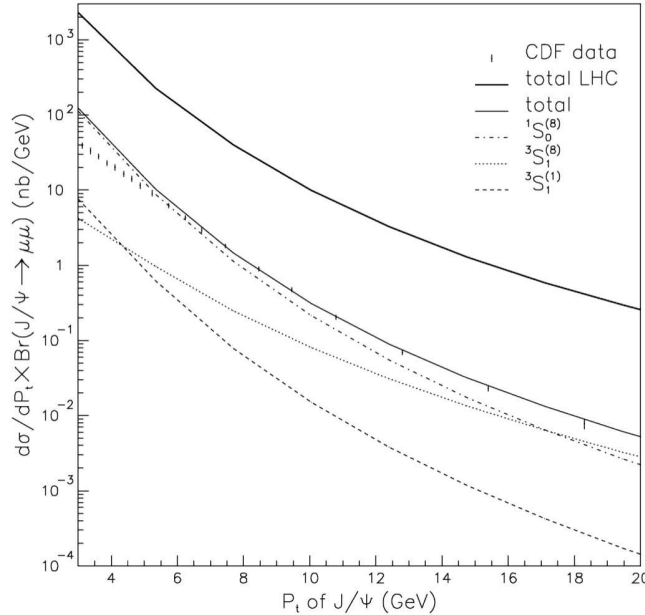
Figure 1.11: Transverse momentum distribution of prompt J/ψ production at Tevatron at $\sqrt{s} = 1.96$ TeV [54] with the NRQCD prediction [53].

---

[7](1) denotes color-singlet state, and (8) color-octet-state.
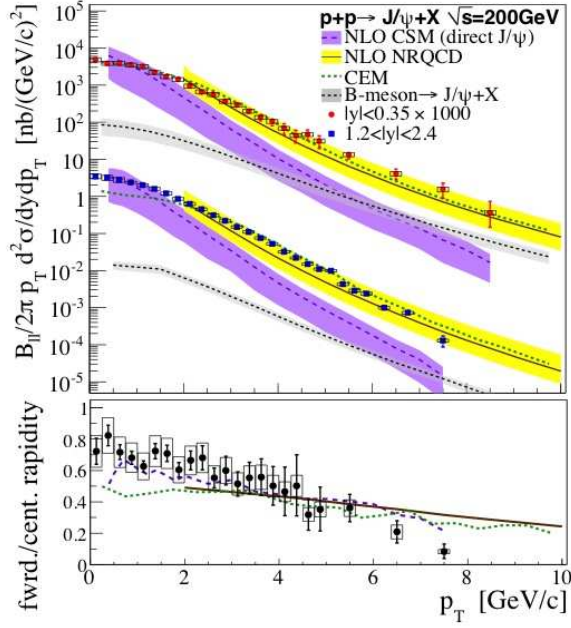
Figure 1.12: PHENIX J/ψ p_T spectrum measurements for mid and forward rapidity at $\sqrt{s}$ = 200 GeV [33] compared with different model predictions.
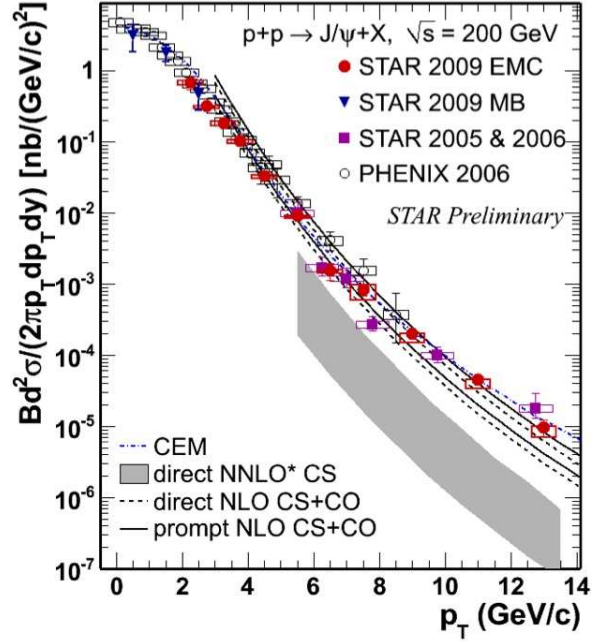
Figure 1.13: STAR J/ψ p_T spectrum measurements for mid-rapidity at $\sqrt{s}$ = 200 GeV [34, 18] compared with different model predictions.

The J/ψ polarization measurement is a crucial test for the NRQCD factorization and the color-octet mechanism. At high p_T, the model predicts strong transverse polarization in the helicity frame ($J_z = \pm 1$, with respect to the J/ψ momentum direction), increasing with p_T [48, 49, 50, 51, 52]. It is in contrary to CSM calculations at next-to-leading and higher orders, which predict longitudinal J/ψ polarization. Gluon fragmentation is the dominant process in the production of a quarkonium with p_T much larger than the quarkonium mass. When $p_T \gg m_{J/\psi}$, the fragmenting gluon is almost on its mass shell, and is therefore transversely polarized. The $c\bar{c}$ pair inherits this polarization, and NRQCD predicts that the polarization is preserve during the non-perturbative transition via a soft-gluon emission to the final physical state. This prediction is in disagreement with CDF polarization measurement [35]. CDF observes that the J/ψ becomes slightly longitudinal with increasing p_T, as it can be seen in Fig. 1.14.

At lower p_T the situation is different. The prediction for the CDF energies ($\sqrt{s}$ = 1.96 TeV) shows almost no polarization at $p_T \approx 5$ GeV/c, and according to calculation for lower energy ($\sqrt{s}$ = 200 GeV) [47] the polarization may even become slightly longitudinal at low p_T (1.5 GeV/c < p_T < 5 GeV/c). The strong transverse polarization is not expected because the fragmentation dominance does not occur at this p_T region [47]. Figure 1.15 shows the polar-

ization measurement from PHENIX [32] at $\sqrt{s} = 200$ GeV/c and at mid-rapidity, compared to COM prediction for prompt J/ψ [47]. The NRQCD prediction agrees with the two PHENIX data points. However, the measurement is limited to small p_T, where the data are not able to distinguish between the COM and CSM predictions regarding the J/ψ polarization.
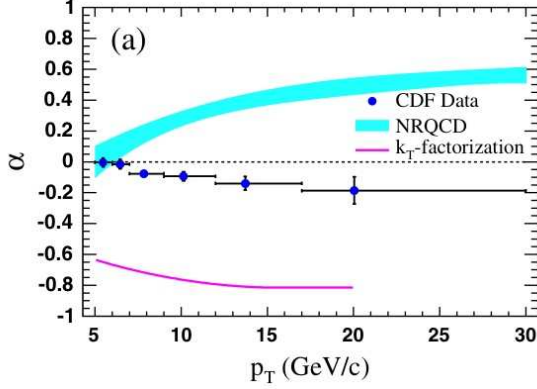
Figure 1.14: CDF prompt J/ψ polarization at mid-rapidity at $\sqrt{s} = 1.96$ TeV in helicity frame [35] compared to NRQCD [48][46] and k_T-factorization [36] models.
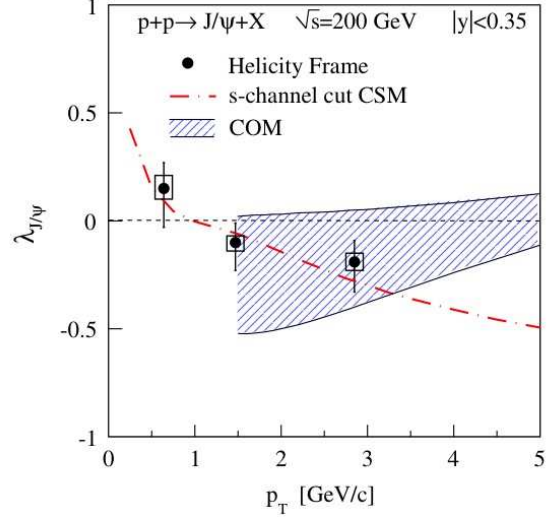
Figure 1.15: PHENIX inclusive J/ψ polarization at mid-rapidity at $\sqrt{s} = 200$ GeV in helicity frame [32] compared to CSM [25] and COM [47] predictions.

1.4.3 Color Evaporation Model

The Color Evaporation Model (CEM) was first proposed in 1977 [37, 38][39]. The model does not assume that the heavy quark pair produced by the perturbative interaction is in a color-singlet state. It is considered that the color and the spin of the asymptotic $c\bar{c}$ state is randomized by soft interactions occurring after its production. As a consequence, the quantum numbers of the $c\bar{c}$ pair are not correlated with the quantum numbers of the final meson. The fraction of the $c\bar{c}$ pairs that form a particular chamonium state is assumend to be independent of the production process. The total cross section for the charmonium production is calculated as the total cross section for quark pair production multiply by the probability that $c\bar{c}$ is in a color-singlet state (1/9):

$$\sigma_{onium} = \frac{1}{9} \int_{2m_c}^{2m_D} dm \frac{d\sigma_{c\bar{c}}}{dm} \tag{1.24}$$

The cross section of $c\bar{c}$ production is integrated from the threshold $2m_c$ up to the threshold to produce two charm mesons $(2m_D)$. The cross section for the J/ψ is then:

$$\sigma_{J/\psi} = \rho_{J/\psi}\sigma_{onium}, \tag{1.25}$$

where $\rho_{J/\psi}$ is the inverse of the number of quarkonium between $2m_c$ and $2m_D$. The $\rho_{J/\psi}$ can be determined only from the fit to the data. [20]

The CEM prediction for the J/ψ cross section is in good agreement with the measured cross section. Figures 1.12 and 1.13 show the newest p_T spectrum from STAR [34][18] and PHENIX [33] compared to the CSM prediction.

However, the simple CEM model prediction does not describe well the production ratios for charmonium states between processes and as functions of kinematic variables [20, 21].

It was suggested that in the framework of the Color Evaporation Model multiple soft gluon exchanges destroy the initial polarization of the heavy quark pair [39]. Since $J = 0$ states get its color randomized during the $c\bar{c}$ evolution, the final angular momentum vector $\overrightarrow{J}$ has no preferred alignment. One can say that the J/ψ is "unpolarized" - probability to found J/ψ in each of the angular momentum eigenstates J_z is the same, $1/(2J + 1)$ [19]. But, in general there is no prediction regarding the J/ψ polarization from the CEM.

1.5 Thesis scope

In this thesis, the first J/ψ polarization measurement in the STAR experiment at RHIC, in $p + p$ collisions at $\sqrt{s} = 200$ GeV at $|y| < 1$ and in p_T range $2 < p_T < 6$ GeV/c, is reported. The analysis is done using data from 2009 year, with a high-p_T electron trigger. The J/ψ is reconstructed via its di-electron decay channel. This analysis focuses on the polar angle, θ. The angular distribution coefficient (polarization parameter) λ_θ of the J/ψ decay into electrons is extracted in the helicity frame [58] as a function of J/ψ p_T. The extraction of λ_θ in the helicity frame allow us to compare the measured J/ψ polarization with different model predictions: NLO^+ Color Singlet Model (NLO^+ CSM) [27] and $NRQCD$ calculations with the color octet contributions (COM) [47].

Chapter 2

The STAR experiment

The Solenoid Tracker at RHIC (STAR) is one of two large experiments, currently taking data, at the Relativistic Heavy Ion Collider (RHIC) at Brookhaven National Laboratory. RHIC is the first machine in the world capable of colliding heavy ions and the first hadron collider with two independent rings which can collide polarized protons. Beams in the rings travel in opposite directions and can collide at six interactions points. The STAR experiment is placed at six o'clock position of the RHIC rings. RHIC is designed to operate with high beam luminosities. It can collide heavy ions, e.g. gold ions, at a wide center of mass energy range, from $\sim$5 GeV up to 200 GeV and protons up to $\sim$500 GeV. RHIC is also able to provide unsymmetrical collisions, e.g. deuterons on gold ions or coper ions on gold ions.

The Relativistic Heavy Ion Collider complex is shown in Fig.2.1, it consists of a chain of particle accelerators. Atoms are ionized in the Tandem Van de Graaff, then ions travel to the small, circular Booster which accelerates ions to higher energy. Then ions are directed to the Alternating Gradient Synchrotron (AGS) which further accelerates them and injects into the RHIC rings where they are accelerated to a desire energy and can be stored for many hours in order to conduct experiments. The same accelerator complex is used for polarized protons, which are supplied by the Linac. Protons travel the same way as heavy ions, starting from the Booster.

2.1   STAR detector

The STAR detector is a multi-purpose detector. It was build to study strongly interactive matter created in ultra-relativistic heavy-ion collisions and its space-time evolution, and search for

Figure 2.1: The RHIC accelerator complex.

signatures of a possible quark-gluon plasma (QGP) formation. The aim is to understand the microscopic structure of hadronic interactions at high energy densities. The three main categories of STAR physics program are: a study of high density QCD, measurement of the spin structure function of the proton, and a study of photon to pomeron interactions from electromagnetic fields of the passing ions at RHIC [66].

The STAR detector consists of many subsystems, it has a cylindrical geometry and a large acceptance with a full azimuthal coverage ($\Delta\phi = 2\pi$). Figure 2.2 shows a layout of the STAR detector. The main, and most important for this analysis, subsystems are marked in the figure. The main tracking detector for charged particles is the Time Projection Chamber (TPC) [67] which is also used to identify particles using dE/dx (ionization energy loss). The TPC pseudorapidity range is $|\eta| < 1.8$ with a full azimuthal coverage. Charged particles momenta are obtained due to their bend in magnetic field, the STAR magnet[68] covers the TPC and most of the subsystems. It is a room temperature solenoid magnet with a uniform magnetic field of a maximum value 0.5T. Outside the TPC is the Time Of Flight (TOF) [69][70] detector with a pseudorapidity coverage of $|\eta| < 0.9$ and $\Delta\phi = 2\pi$. The TOF extends, by measuring a particle velocity, STAR particle identification capabilities to momentum ranges where the TPC alone is not very efficient. Direct identification of $\pi/K/p$ is possible up to momenta $\sim$1.7-1.9 GeV/c, and $(\pi + K)/p$ identification up to $p \sim$2.9-3.1 GeV/c. The Vertex Position Detectors (VPD) [71], which are placed outside the magnet and close to the beam pipe, are start detectors for a
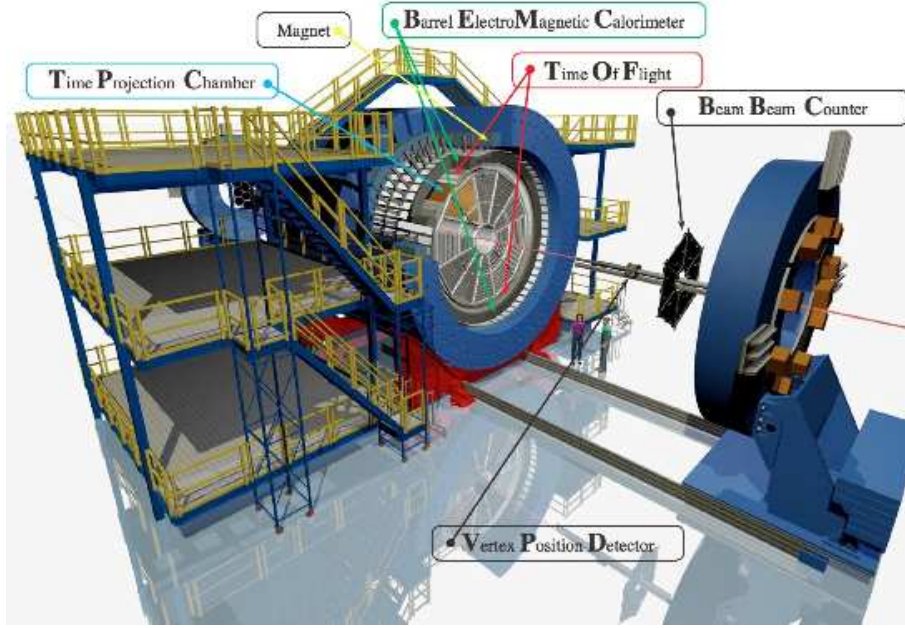
Figure 2.2: The STAR detector.

particle Time of Flight measurements and provide a minimum bias trigger. Between the TOF and the magnet there is the Barrel Electromagnetic Calorimeter (BEMC) [72] which covers $|\eta| < 1$ and $\Delta\phi = 2\pi$. The BEMC is used to study rare, high-p_T processes, such as jets, leading hadrons, direct photons, heavy quarks, and provide large acceptance for photons, electrons, π^0 and η mesons. The BEMC is a fast detector and it is utilized to discriminate against pileup tracks in the TPC (tracking detectors are too slow), arising from other beam crossing falling within the TPC drift time. BEMC can be also used to trigger on high-p_T electrons.

2.1.1 Time Projection Chamber (TPC)

The Time Projection Chamber (TPC) [67] is a main tracking device for charged particles in the STAR detector. It has a cylindrical shape and provides a complete coverage around the beam line. Its inner and outer radius is 50 cm and 200 cm, respectively. The TPC in a volume filled with a gas in a uniform electric field of $\approx 135\ V$/cm. It is 4.2 m long and 4 m in diameter. A pseudorapidity range for tracking is $|\eta| < 1.8$ with a full azimuthal angle. A schematic view of the TPC is shown in Fig.2.3. The TPC records particle tracks, and from the curvature of a track in the magnetic field the particle momenta from 100 MeV/c up to $\sim$30 GeV/c can be measured. A particle identification is done using particle ionization energy loss (dE/dx) in the TPC gas, an example of the dE/dx distribution as a function of the particle momentum is shown in Fig.2.4. Pions and protons can be separated up to 1.2 GeV/c.
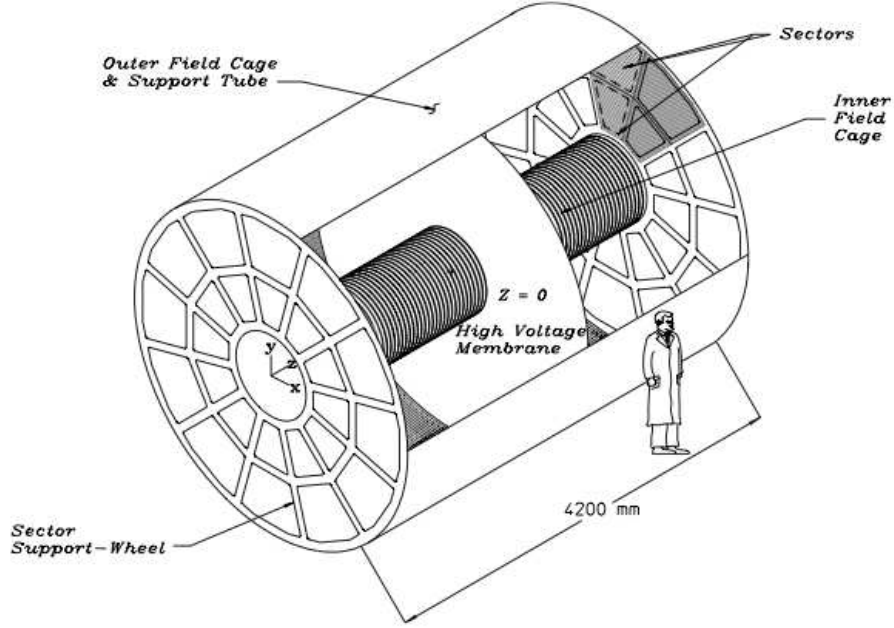
Figure 2.3: The STAR TPC.

Charged particles passing through the TPC gas ionise gas atoms and leave traces made of released electrons. These primary ionizing particles are reconstructed from the released secondary electrons which drift to the ends of the detector in the electric field. The TPC is filled with the P10 gas (90% of argon and 10% of methane) and its pressure is $2\ mbar$ above atmospheric pressure. The uniform electric filed is defined by a thin conductive Central Membrane (CM) at the center of the TPC, concentric field-cage cylinders and the readout end caps. An operating voltage of a cathode at the CM is 28 kV, while the end caps, where anodes are placed, are at ground. The read out system at the end caps is based on Multi-Wire Proportional Chambers (MWPC) with readout pads.

MWPC chambers on the end caps consists of a pad plane and three wire planes: an anode wire plane (amplification/readout layer), a ground wire plane and a gating grid. The purpose of the ground wire plane is to terminate the filed in the avalanche region and provide additional rf shielding for the pads. The gating grid is a shutter to control entry of electrons from the TPC drift volume into the MWPC, and blocks ions produced in the MWPC from entering the drift volume. The readout planes are modular units arranged in 12 sectors around the circle. Each sector is divided into an inner and outer part, see a schema of the anode pad plane with one full sector in Fig.2.5. The outer sub-sectors have continuous pad coverage in order to optimize the dE/dx resolution and improve a bit the tracking resolution. The inner sub-sectors, which are in the region of the highest track density, are optimized for a good two-hit resolution. These sub-

42
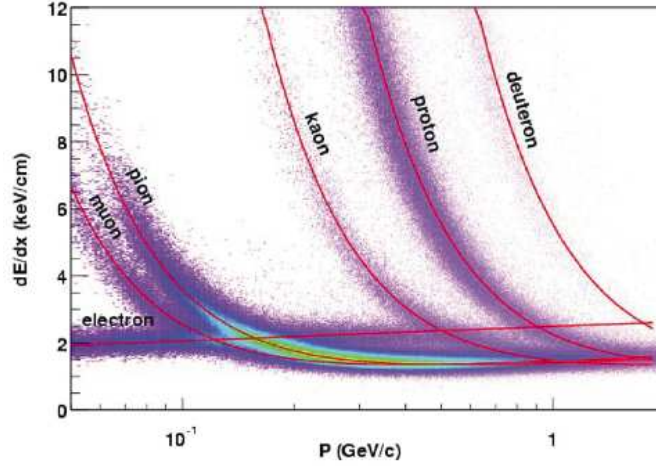
Figure 2.4: The dE/dx distribution as a function of the track momentum at magnetic filed of 0.25T [67].

sectors are built from smaller pads, with separate pad rows. Because of that the inner sectors do not improve significantly the dE/dx resolution. Their purpose is to improve the momentum resolution by extending the position measurements to small radii, along a track, and to detect particles with low momenta.

Track reconstruction.

A track can be reconstructed by maximum 45 pad rows, usually it is less due to the track curvature, emission angle, fiducial cuts, etc. The tracking efficiency is on average about 80-90%. The trajectory of a primary particle is reconstructed by joining ionization clusters along the track. The clusters are found separately in x, y and z direction. Local x direction is along the direction of a pad row, y axis extend from the beam line outwards and is perpendicular to the pad rows, and the z axis is along the beam line. A cluster, for example in x position, is created from ionization points on adjacent pads, within a pad row, with similar drift times. The x and y coordinates of a cluster are determined by measuring the charge on adjacent pads in a single pad row. The local x is found from the Gaussian fit to the signal distribution on the pads, with $y = 0$. Then the local coordinates are translate to the global coordinates using a pad global position. The z coordinate of a point inside the TPC is determined by measuring the time of drift of a cluster of secondary electrons (realised during the gas ionisation), from the point of origin to the anodes on the end cap dividing by the average drift velocity. Since the drift velocity has to be known with a precision of 0.1% in order to reconstruct position with a sufficient accuracy, it

43
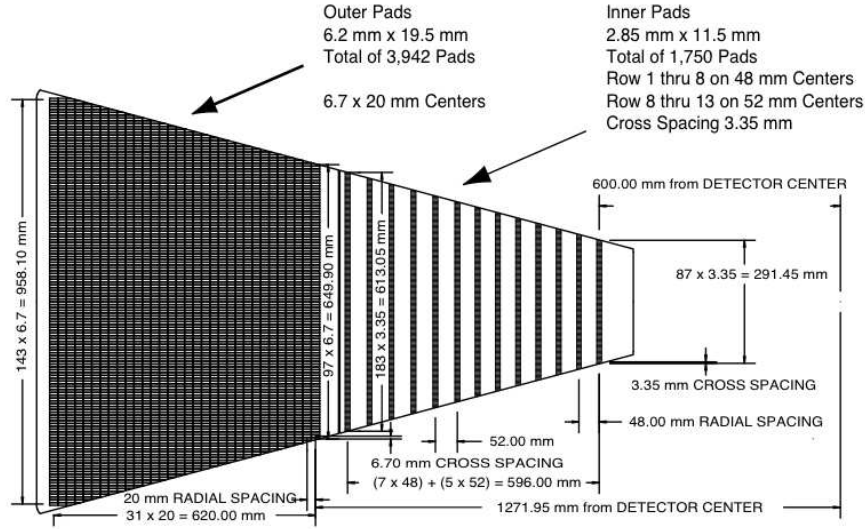
Figure 2.5: The TPC anode pad plane with one full sector [67].

is measured every few hours during the data taking using special laser tracks [74].

The found space points are associated with each other in order to reconstruct the track of a particle. The association is done using a special tracking software. In order to extract the particle momentum, the points on a track are fitted with a track model. The track is modelled as a helix, and then effects that cause a trajectory to slightly deviate from the helix, such as the energy loss in the gas, are taken into account in the model. In order to avoid broken track fragments, it is required that a track has hits on at least 10 pad rows. To improve the momentum resolution of a track, the primary vertex can be used. The primary vertex is found by extrapolating all reconstructed in the TPC tracks back to the origin and taking the global average of the found positions of tracks origins. Tracks that have a distance of the closest approach to the primary vertex (in three dimension) less than 3 cm are refitted with the primary vertex included in the fit and are called primary tracks.

The tracking efficiency depends on the acceptance of the detector, the electronic detection capabilities, two-hit separation capabilities of the system, and the fiducial cut. The efficiency, as well as the momentum resolution, are estimated using simulated tracks embedded into real events. Details on the tracking efficiency, momentum and vertex resolution, and dE/dx can be found here [67].

2.1.2 Time Of Flight (TOF)

Time of Flight system [69] [70] [71] extends the TPC charged hadron identification capabilities to higher particle momenta. The TPC alone can separate charged hadrons π/K and $(\pi+K)$/p up to $p_T \approx 0.7$ and 1.1 GeV/c, respectively. The TOF provide charged hadrons π/K and $(\pi+K)$/p separation up to $p_T \approx 1.6$ GeV/c and 3.0 GeV/c, respectively [75]. The inverse velocity, $1/\beta$, distribution as a function of particle momentum is show in Fig.2.6. β is a track path length divided by the Time of Flight and the speed of light, $\beta = pathLength/TimeOfFlight/c$. The TOF time resolution is $\lesssim 100$ ps. Charged hadron identification can be extended to $2 < p_T < 4$ GeV/c using a combination of the TPC and TOF detectors [75].

A start time for the Time of Flight measurement is given by the VPD detectors [71], and the TOF detector is a stop detector for the time measurement. The VPD detectors are mounted outside the STAR magnet, on both sides of the STAR detector and very close to the beam pipe, as it can be seen in Fig.2.2. The detectors consist of 19 Hamamatsu fine mesh dynode photomultiplier tubes. The VPD also provides position of an event vertex and can be used as a minimum bias trigger.
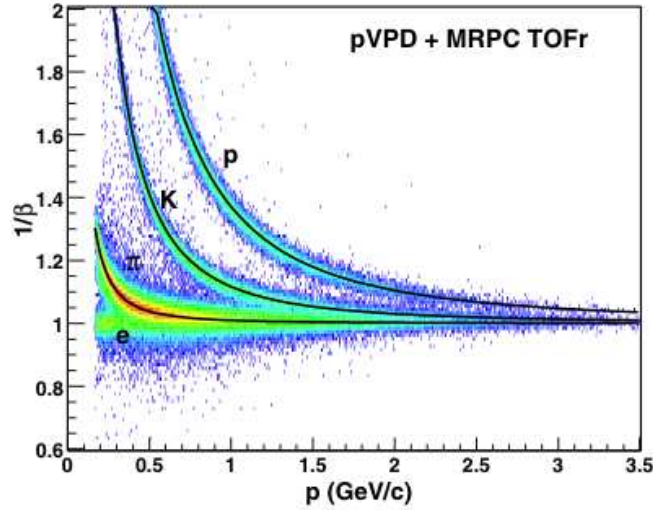
Figure 2.6: The inverse velocity for charged hadrons as a function of a particle momentum [69].

For lower momenta it is not possible to efficiently identify electrons using the TPC only. The electron identification can be improved, using both dE/dx information from the TPC and β from the TOF. For momenta below 1.5 GeV/c there are regions where proton and Kaon dE/dx bands overlap with the electron dE/dx band, and thus it is not possible to obtain a pure electron sample in this momentum range, using the TPC alone. The upper plot in Fig.2.7 shows

the dE/dx distribution as a function of particle momentum for d+Au collisions [75]. Slower hadrons can be efficiently rejected using a cut on the β: $|1/\beta - 1| < 0.03$, Fig.2.7b shows the dE/dx distribution with the $1/\beta$ cut applied. The electron dE/dx band is now well separated from the pion band.
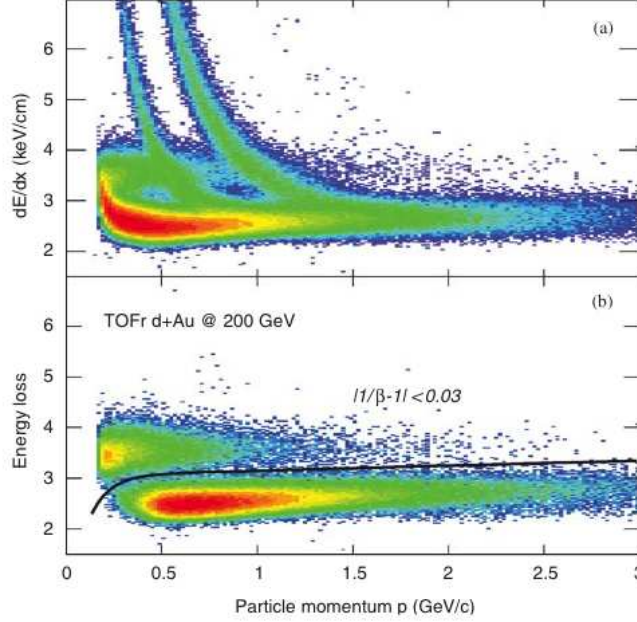
Figure 2.7: The TPC dE/dx as a function of a particle momentum [75].

The TOF detector has a full azimuthal coverage with pseudorapidity range of $|\eta| < 0.9$. It is placed outside the TPC detector and is arranged in 120 trays. The TOF detector is based on the multi-gap resistive plate chamber (MRPC) technology. The MRPC is a stack of parallel, resistive plates (float glass), with a series of uniform gas gaps in between. The TOF MPRC cross section is shown in Fig.2.8a, Fig.2.8b shows the printed circuit board with readout pads array. On outer glass plates, graphite electrodes are placed. To the electrodes high voltage ($\sim$ 14 kV) is applied and a strong electric field is generated in each gap. The inner glass plates float electrically. Copper readout pads are located outside the electrodes. The signal induced on the readout pads is a sum of avalanches that result from ionization inside the gaps, caused by a charged particle going through the glass stack. During operation, the MRPCs are surrounded by a gas, that consists of Freon R-134a in 95% and 5% of isobutane. [69]
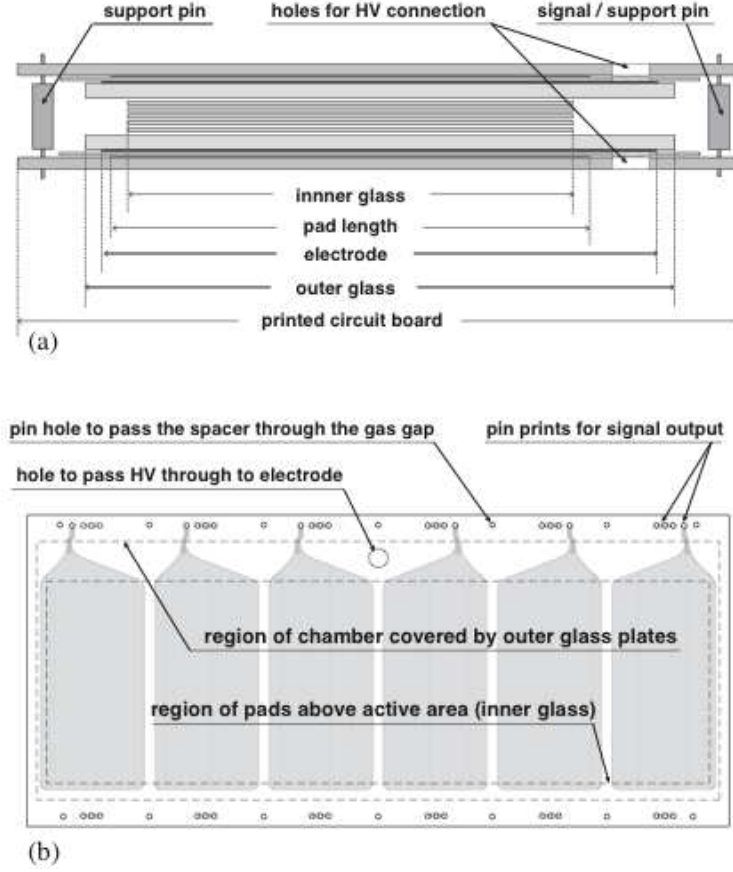
Figure 2.8: (a) Cross section of the TOF MPRC module. (b) Top view of the printed circuit board with readout pads array. [70].

2.1.3 Barrel Electromagnetic Calorimeter (BEMC)

The BEMC [72] is located between the TOF detector and the STAR magnet, it covers pseudorapidity range of $|\eta| < 1$ and full azimuthal angle. The detector's depth is approximately 20 radiation lengths $(20X_0)$ at $\eta = 0$. It is a sampling calorimeter build of a lead and plastic scintillator. The BEMC consists of 120 modules, 60 in ϕ and 2 in η, each of module is built of 40 towers, 2 in ϕ and 20 in η. The detector has 4800 towers in total, 0.05 by 0.05 in $\eta - \phi$. A side view of a module is shown in Fig.2.9. The energy resolution is $dE/E \approx 16\%/\sqrt{E}$. A BEMC module consists of 20 lead layers and 21 layers of scintillator, two first, thicker layers of scintillator are used as a PreShower detector (PSD) [72]. At approximately 5 radiation lengths from the front of the stack the Shower Maximum Detector (SMD) [72] is located.

A BEMC tower's size, at the inner radius, is $\sim 10 \times 10 \ cm^2$ at $\eta = 0$, and increases with increasing η. While the size is enough to provide precise energy measurements for isolated
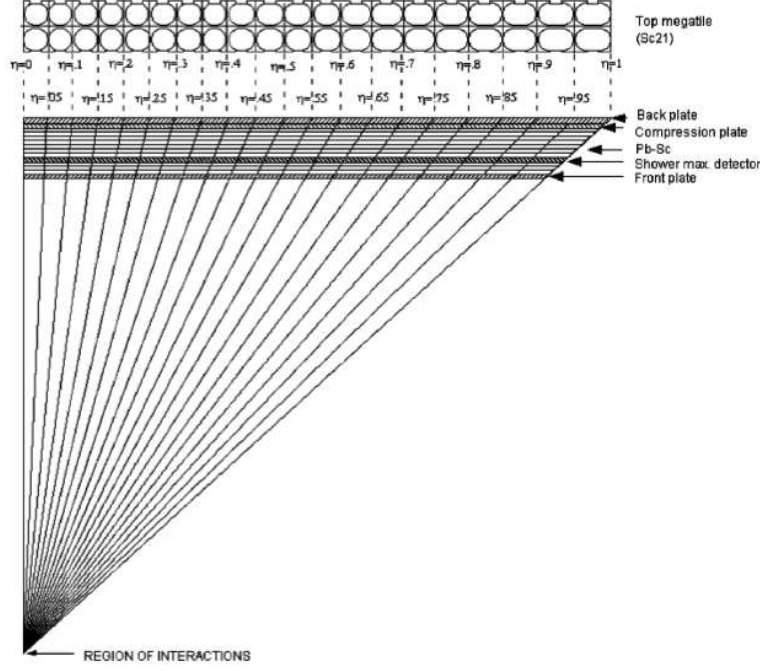
Figure 2.9: A side view of a BEMC module [72].

electromagnetic showers, it is larger that the Molier radius [1] and thus does not allow for a precise spatial reconstruction of electromagnetic showers. A high spatial resolution measurements of a shower distribution in orthogonal transverse dimensions can be done using the Shower Maximum Detector (SMD). The SMD provides information on a shower position and a shape as well as on a longitudinal development (i.e. along a tower) of the electromagnetic shower. It is essential to separate π^0 and isolated (direct) photons and identify electrons from the intense hadron background. The SMD is a wire proportional counter-strip readout detector, it consists of two layers. It is is located at $\approx$ 5.6 radiations lengths in the calorimeter, at $\eta = 0$. Near this depth there is a maximum density of electromagnetic showers, with energy $\gtrsim$ 1-2 GeV. There is 1200 areas, approximately 0.1 by 0.1 in $\eta - \phi$, each of the area has 15 stripes in ϕ and 15 in η. So there is total of 36 000 stripes in the SMD. The SMD double layer is shown in Fig.2.10.

The PreShower detector (PSD) is integrated into each of the 4800 BEMC towers. The first two scintillating layers of the BEMC are used as the PSD. The detector provides the longitudinal shower development after (1-1.5) radiation length. The PSD is important for π^0 and γ discrimination (especially at high p_T it is difficult to make this discrimination at the STAR

---

[1]The Moliere radius is a characteristic constant of a material describing its electromagnetic interaction properties. It gives the scale of the transverse dimension of the electromagnetic showers. By definition, it is the radius of a cylinder containing on average 90% of the shower's energy deposition [73].
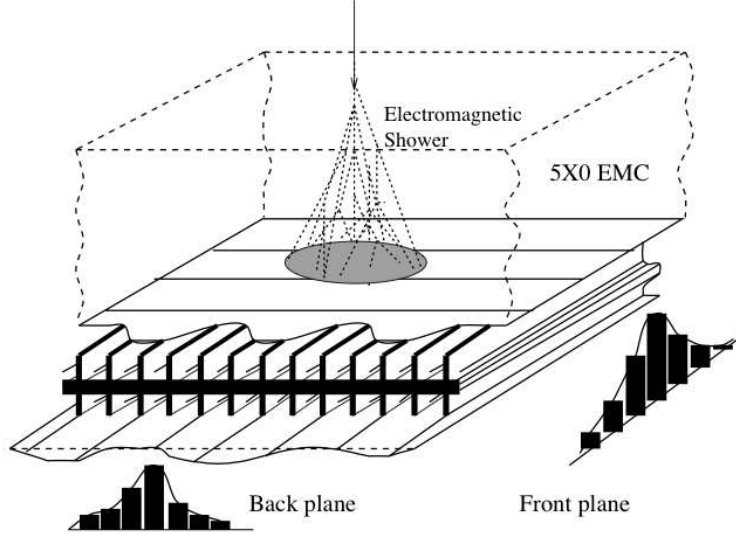
Figure 2.10: The BEMC SMD double layers [72].

detector radius with the SMD), it can be also used for the electron/hadron discrimination.

The BEMC detector is used to trigger on and to study rare, high-p_T processes, such as jets, leading hadrons, direct photons, heavy quarks. The detector is fast and sensitive to the particles' total energy and thus it is an important part of the STAR level-0 trigger.

Electron identification

The tower energy and shower information from the SMD detector can be used to identify electrons. The SMD is especially useful in hight intensity environment, like in Au+Au collisions.

The BEMC is constructed so that an electron should deposit all its energy it the BEMC towers. While hadrons, even those which shower in the BEMC, usually deposit only a fraction of their energy in the towers. The energy deposited by a particle in the BEMC can thus be used to discriminated between electrons and hadrons, by taking E/p ratio, where E is energy and p in the track momentum. For low mass electrons $E \approx p$ and the E/p ratio is expected to be ≈ 1.

The SMD can help to further discriminate between electrons and hadrons. At the depth where the SMD is placed, the electromagnetic shower should be fully developed while hadronic showers are still incomplete. Electrons should have more hits in the SMD $\eta - \phi$ than hadrons, since their broader shower activate more SMD stripes.

Chapter 3

Data analysis

3.1 Analysis method

This section contains a brief description of used analysis method for J/ψ reconstruction and the J/ψ polarization extraction.

In this analysis the inclusive J/ψ production is studied. Inclusive J/ψ's are prompt J/ψ's (directly produced and from a feed-down from the higher exited states of the charmonium, $\psi^{'}$ and χ_C) and non-prompt J/ψ's from a feed-down from the B meson decays. J/ψ lifetime is very short, $7 \times 10^{-21}s$ (the decay width is $92.9 \pm 2.8 keV$ [1]) , and the B meson lifetime is longer, $(0.453 \pm 0.041) \times 10^{-12}s$ [1]. In general, it is possible to separate the J/ψ from the B meson decay by reconstructing the secondary vertex. But the STAR detector does not have the necessary resolution.

J/ψ is analysed via its dielectron decay channel $J/\psi \rightarrow e^+e^-$ $(BR = 5.94\% \pm 0.06\%$ [1]) at mid-rapidity ($|y| < 1$). The branching ratio to leptons, $J/\psi \rightarrow e^+e^-$ and $J/\psi \rightarrow \mu^+\mu^-$, is high due to the fact that the hadronic decay modes are suppressed by the OZI Rule. Also, the advantage of leptons is that they do not interact strongly.

Since J/ψ decays almost in the collisions vertex it cannot be reconstructed using a topological method, so a statistical method is used. All electron candidates in an event are paired with all positron candidates and the J/ψ is identify as e^+e^- pairs which invariant mass is in a range $2.9 < m_{e^+e^-} < 3.3$ GeV/c^2. A combinatorial background under the J/ψ peak (random, uncorrelated e^+e^- pairs) is estimated using a like-sign technique. All e^+ and all e^- in an event are paired and the background is a sum of all e^+e^+ and e^-e^- pairs: $N_{e^+e^+} + N_{e^-e^-}$. In order to get the J/ψ signal, the background distribution is subtracted from the distribution for e^+e^-.

In this analysis we are interested in high-p_T J/ψ which have at least one e^+ or e^- with high p_T. Used High Tower (HT) trigger allows us to select events with high-p_T electron and it is required that at least one of electrons from the J/ψ decay satisfies the HT trigger conditions. With the HT trigger requirements the obtain J/ψ are with $2 < p_T < 6$ GeV/c and the combinatorial background under the J/ψ signal is reduced significantly.

Electrons are identified using information from the TPC detector. In addition, the TOF detector is used for lower momenta and the BEMC detector for higher momenta. Event and track selection, and offline cuts are described in sections 3.2.1, 3.2.2. Efficiencies are extracted from the data and a Monte Carlo simulation, and are discussed in section 3.4.

In this document, during analysis discussion, we refer to both electrons and positrons as electrons.

J/ψ polarization analysis method

J/ψ polarization is analysed via the angular distribution of the electron decay from J/ψ in the helicity frame [58]. In the helicity frame the polarization axis is along the J/ψ direction in the lab frame. The angular distribution is derived from the density matrix elements of the production amplitude using parity conservation rules. In this analysis, we are interested in the polar angle θ. It is the angle between the positron momentum vector in the J/ψ rest frame and the J/ψ momentum vector in the laboratory frame, as it is illustrated in Figure 3.1.

The angular distribution integrated over the azimuthal angle is parametrized:

$$\frac{dN}{dcos\theta} \propto 1 + \lambda_\theta cos^2\theta \qquad (3.1)$$

where angular decay coefficient λ_θ is called a polarization parameter and contains both the longitudinal and transverse components of the J/ψ cross section. When $\lambda_\theta = 0$ there is no polarization, $\lambda_\theta = $ -1 means full longitudinal polarization and $\lambda_\theta = 1$ corresponds to full transverse polarization.
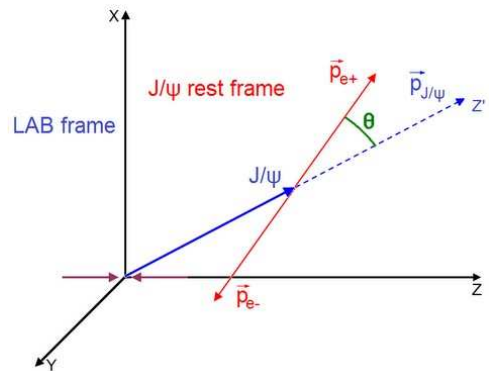
Figure 3.1: Definition of the θ angle in helicity frame.

In this analysis the p_T dependent J/ψ polarization parameter λ_θ is obtained by extracting the θ angle from the data and fitting $norm(1 + \lambda_\theta cos^2\theta)$ function to $dN/dcos\theta$ distributions in three p_T bins.

3.2 Event and track selection

3.2.1 Event selection

The p+p 200 GeV dataset used in this analysis is from year 2009, collected with the High Tower (HT) trigger. The trigger required transverse energy deposited in a single BEMC tower to be within $2.6 < E_T \leq 4.3$ GeV [1]. The HT trigger also includes a minimum bias trigger that required a coincidence two Vertex Position Detectors (VPD) [71]. Information about the trigger is gathered in a table 3.1. The table shows the trigger id and name, integrated luminosity, number of events taken with that trigger and the trigger conditions. The analysed data was sampled from an integrated luminosity of $\sim$1.8 pb^{-1}.

Trigger Id	Name	Lum	Nevents	Description
240570	BHT0* VPDMB* !BHT2 [2]	1.807 $[pb^{-1}]$	36.137 M	$11(2.6GeV) < HT \leq 18(4.3GeV)$

Table 3.1: High Tower trigger used in the analysis.

In the analysis, tracks that originate from a primary vertex of an event are used. In order to ensure a good quality of selected events, cuts on a TPC primary vertex position are applied. The cuts are listed below:

- $\neg(|V_x| < 10^{-4} \wedge |V_y| < 10^{-4} \wedge |V_z| < 10^{-4})$ cm - primary vertex positions in x, y and z have to be greater than 10^{-4} cm

- $|V_z| \leq 65$ cm

V_x, V_y and V_z are x, y and z positions of a primary vertex, respectively.

The integrated luminosity of analysed sample with the HT trigger is $\sim$1.8 pb^{-1} and after applying cuts on the vertex position the integrated luminosity is $\sim$1.6 pb^{-1} ($\sim$ 32.8 M events).

The same cut of $|V_z| \leq 65$ cm, on the z position (along the beam axis) of a vertex is applied in the data and the simulation analysis. The V_z cut helps also to select tracks with a good quality. Tracks that originate from a vertex which is far from the TPC center, close to the

---

[1]this is a transverse energy range that corresponds to DSM (Delta Sigma Modulator) ADC range of $11 < dsmAdc \leq 18$

[2]BHT0 trigger ($HT > 11$) with a minimum bias trigger ($VPDMB$) and BHT2 trigger ($HT > 18$) excluded.

detector edge, are reconstructed based on fewer hit points in the TPC and thus have a worse quality. A distribution of the z position of a primary vertex is shown in Fig. 3.2. One can see that applied cut on V_z does not reject many events, and so the efficiency of the cut is quite high. A vertex with x and y and z positions equal to zero is a badly reconstructed vertex, thus it is also required that x, y and z positions of a vertex are greater than 10^{-4} cm.
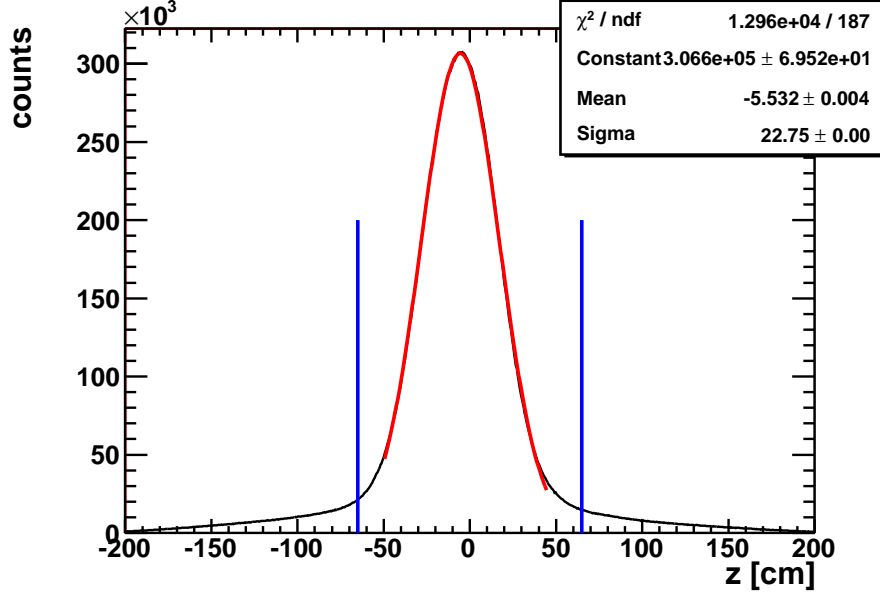
Figure 3.2: Z position (along the beam axis) of the primary vertex for HT triggered events fitted with the Gaussian function. The mean value is shifted to negative values due to a beam misalignment. Vertical lines represent the range of the V_z cut ($|V_z| \leq 65$).

To reduce the pile-up, it is required that each track is matched to a fast detector (BEMC or TOF), more details about track cuts are in the following section, 3.2.2.

3.2.2 Track selection

3.2.2.1 Track quality and acceptance cuts

In the analysis only primary tracks [3] are used. Following track quality and acceptance cuts are applied:

- $0 \leq flag < 1000$

- $nFitPts \geq 15$

---

[3]Tracks which originate from a primary vertex, that have the distance of the closest approach to the primary vertex is less than 3 cm

- $nFitPts/nFitPtsMax \geq 0.52$

- $DCA \leq 2$ cm

- $|\eta| \leq 1$

- $p_T \geq 0.4$ GeV/c

$Flag$ variable is a track quality control flag from the track fitting procedure. Tracks with a negative value of the $flag$ are poorly reconstructed and are removed. Also, tracks with the $flag \geq 1000$, which are pile-up tracks, are not included in this analysis.

To ensure a good quality of a track and a good resolution of a track momentum the cut on a minimum number of points in a track fit ($nFitPts$) of 15 is used. In addition, the number of $nFitPts$ has to be greater than 50% of possible number of fit points in order to remove split tracks. The cut is: $nFitPts/nFitPtsMax \geq 0.52$, where $nFitPtsMax$ is the maximum number of available points in the fitting procedure.

J/ψ has a very short lifetime so it decays in the event vertex. Therefore we use only primary tracks with the cut on the distance of the closest approach to the primary vertex of $DCA \leq 2$ cm.

The transverse momentum cut for a single track is quite low, $p_T \geq 0.4$ GeV/c. This is mostly in order to increase a number of extracted J/ψ's and due to an acceptance in $cos\theta$. Increasing the value of the cut on p_T causes loss of the J/ψ signal at $|cos\theta| \sim 1$. Decreasing the value of the p_T cut below 0.4 GeV/c does not change the acceptance in $cos\theta$, while increases the combinatorial background under the J/ψ signal. $p_T \geq 0.4$ GeV/c cut is optimal in terms of the acceptance in $cos\theta$ and a significance of the J/ψ signal.

Figures 3.3, 3.4, 3.5, 3.6, 3.7, 3.8 show $nFitPts$, $nFitPts/nFitPtsMax$, DCA, η, p_T and momentum distributions after all track quality and acceptance cuts, respectively.

3.2.2.2 Hight Tower trigger conditions

It is required, in this analysis, that at least one of electrons from the J/ψ decay fired the HT trigger (the trigger condition: $11 < dsmAdc \leq 18$). And an additional cut of $p_T \geq 2.5$ GeV/c is applied on the transverse momentum of the particle that fired the trigger.

A decision if a particle fired the trigger is made by the trigger simulator based on the DSM ADC [4] value in a BEMC tower (the trigger condition: $11 < dsmAdc \leq 18$). The lower dsmAdc

---

[4]Delta Sigma Modulator ADC
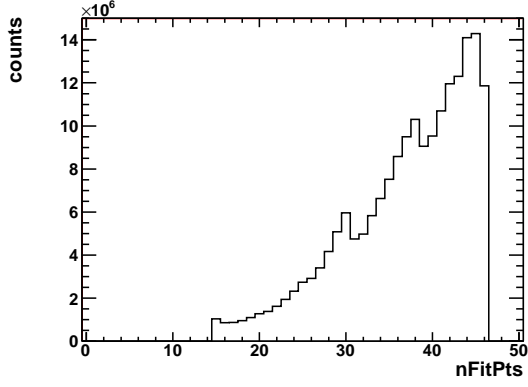
Figure 3.3: $nFitPts$ distribution after all track quality and acceptance cuts.
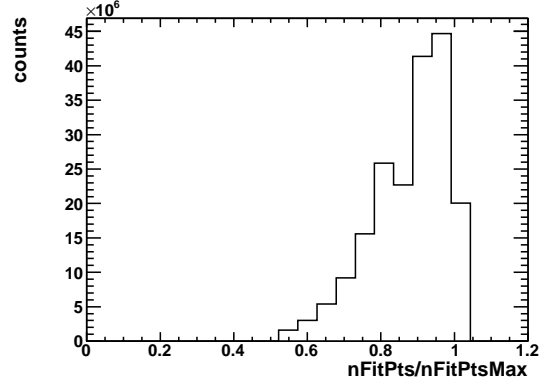
Figure 3.4: $nFitPts/nFitPtsMax$ distribution after all track quality and acceptance cuts.
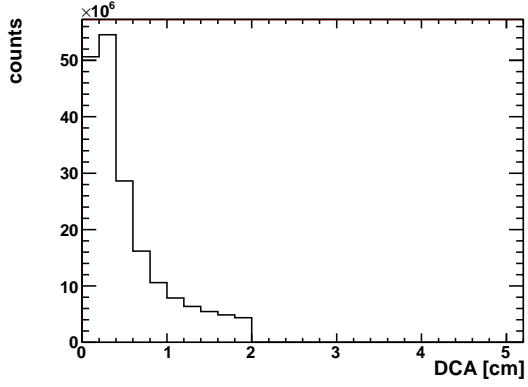
Figure 3.5: DCA distribution after all track quality and acceptance cuts.
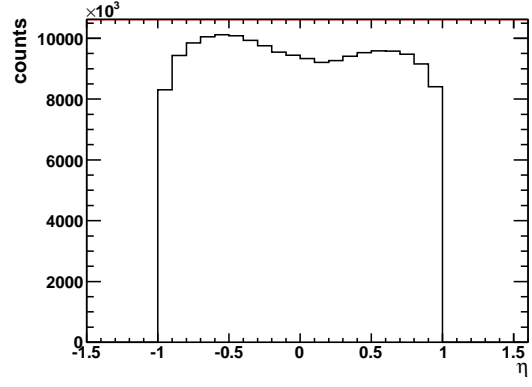
Figure 3.6: η distribution after all track quality and acceptance cuts.
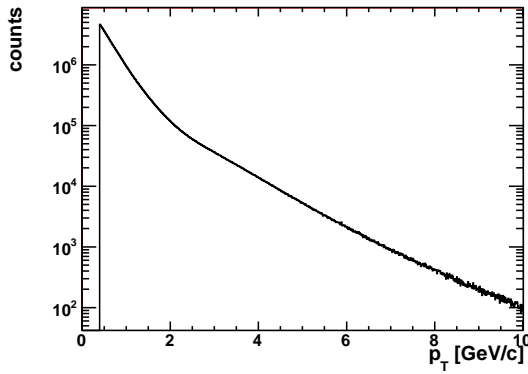
Figure 3.7: p_T distribution after all track quality and acceptance cuts.
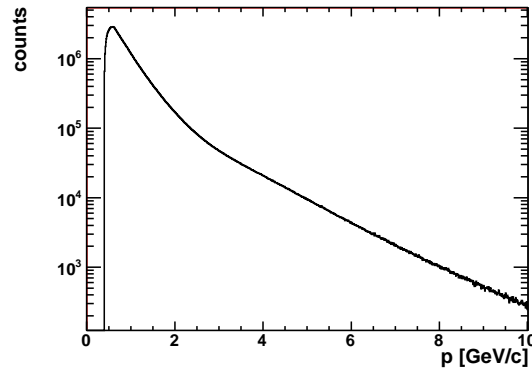
Figure 3.8: Momentum distribution after all track quality and acceptance cuts.

cut corresponds to a minimum transverse energy deposited in a single BEMC tower of ~ 2.6 GeV. In order to ensure that the particle that was found by the trigger simulator as a particle that fired the trigger was indeed a particle that could fired a trigger (there can be other hit in the same BEMC tower), an additional cut on that particle p_T is applied in the data analysis: $p_T \geq 2.5$ GeV/c. The requirement of one electron with high p_T reduces the combinatorial background and allows to obtain J/ψ signal with high p_T.

3.2.2.3 Electron identification cuts

J/ψ is reconstructed via its di-electron decay channel. In order to select electrons and reject hadrons information from the TPC, TOF and BEMC detectors is used. Electron identification (eID) cuts are applied using that information.

For whole momentum range $n\sigma_e$ variable which is based on dE/dx [5] from TPC is used to select electrons. $n\sigma_e$ describes a probability that a given track is an electron and is defined as:

$$n\sigma_e = \frac{log[(dE/dx)/(dE/dx \mid_{Bichsel})]}{\sigma_e} \tag{3.2}$$

dE/dx is a measured ionization energy loss in the TPC, $dE/dx \mid_{Bichsel}$ is an expected value of dE/dx from the Bichsel function [77] and σ_e is the resolution of the dE/dx. Figure 3.9 shows a dE/dx distribution as a function of rigidity ($p * q$) for tracks that passed the track quality and acceptance cuts, which are listed in Tab. 3.2. The figure also shows theoretical predictions of the Bichsel functions for different particle species. One can see that there is a lot of hadrons, especially pions in the sample. $-1 \leq n\sigma_e \leq 2$ cut selects electrons very efficiently and rejects a lot of pions in whole momentum range and other hadrons for $p \gtrsim 1.4$ GeV/c. The $n\sigma_e$ cut is asymmetric because the pion expected dE/dx range is below the electron expected dE/dx range, and due to the relativistic rise at higher p_T the pion band gets closer to the electron band. Figure 3.10 shows the dE/dx distribution after the TOF ($p < 1.4$ GeV/c) and the BEMC ($p \geq 1.4$ GeV/c) eID cuts, and the dE/dx distribution for particles identified as electrons (after all eID cuts) is shown in Fig. 3.15.

For $p \lesssim 1.4$ GeV/c there are regions where proton and Kaon bands overlap with the electron band. In that momentum range protons and Kaons cannot be rejected efficiently with the TPC alone without a significant loss of electrons at the same time. The TOF detector (72% of full

---

[5]Particle ionization energy loss in the TPC gas per unit of length.
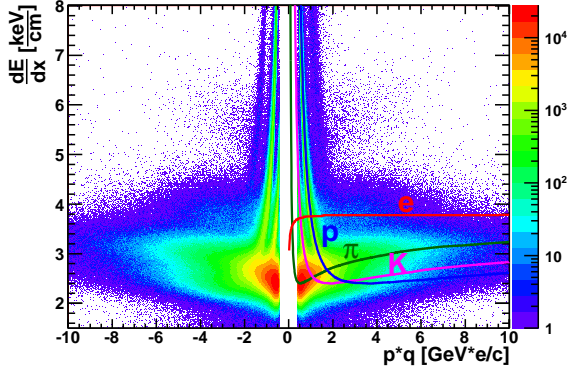
Figure 3.9: dE/dx distribution as a function of rigidity ($p*q$) for particles that passed track quality and acceptance cuts.
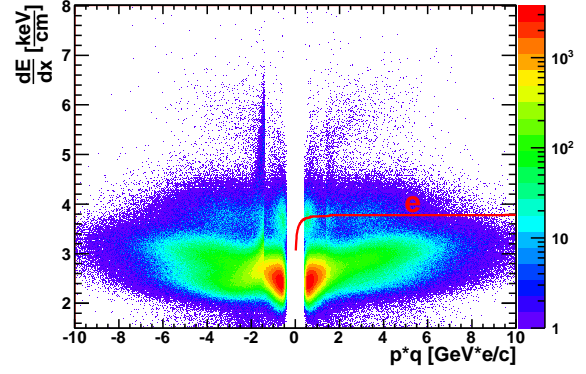
Figure 3.10: dE/dx distribution as a function of rigidity ($p*q$) for particles that passed the TOF ($p < 1.4$ GeV/c) and the BEMC ($p \geq 1.4$ GeV/c) eID cuts.

TOF was installed in 2009) allows to apply cut on the β[6] variable. Since electrons are faster ($1/\beta \sim 1$) than hadrons, $|1/\beta - 1| \leq 0.03$ cut rejects hadrons (mostly protons and kaons) at lower momenta very well. The cut corresponds to 2σ of the TOF resolution and is used at $p < 1.4$ GeV/c. In order to assure that a given track from the TPC is properly matched to the TOF, cut on the y_{Local}[7] variable is applied: $|y_{Local}| \leq 2$ cm. Figure 3.11 shows the $1/\beta$ distribution after the track quality and acceptance cuts (the $|y_{Local}| \leq 2$ cm cut was also applied when matching a track to the TOF). Figure 3.12 shows the $1/\beta$ distributions after the TPC and BEMC eID cuts. The horizontal lines represent a range of the $1/\beta$ cut. The $1/\beta$ distribution for particles identified as electrons (after all eID cuts) in shown in Fig.3.16 .

For higher momenta, $p \geq 1.4$ GeV/c, the information about energy deposited in BEMC towers is used to reject hadrons. For electrons it is expected that $E/p \sim 1$, where E is total energy deposited in the BEMC, and p is a track momentum. And thus $E/p \geq 0.5\ c$ cut is used to select electrons and reject hadrons. The cut is loose since taken energy is from a single BEMC tower ($\Delta\eta \times \Delta\phi = 0.05 \times 0.05$) that a given track projects to, and only fraction of the electron energy might be deposited in that tower (energy deposited by the electron can spread to surrounding towers). The cut of $E \geq 0.1$ GeV (E is energy deposited by a track in a BEMC tower) removes the noise in a BEMC tower. When projecting a TPC track to the BEMC the nearest BEMC tower is taken. Therefore, there is no need to apply an additional cut, on a

---

[6]$\beta = v/c = pathLength/TimeOfFlight/c$

[7]y_{Local} is the y coordinate of a hit local position in the TOF
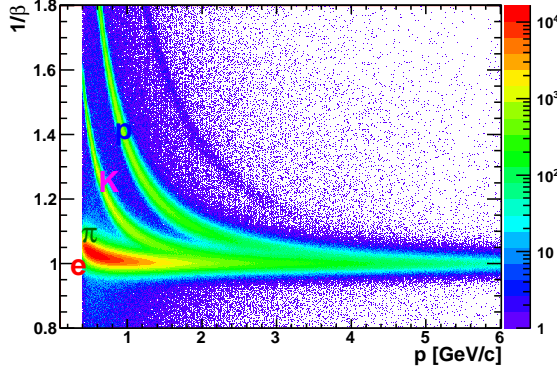
Figure 3.11: $1/\beta$ distribution as a function of momentum for particles that passed the track quality and acceptance cuts.
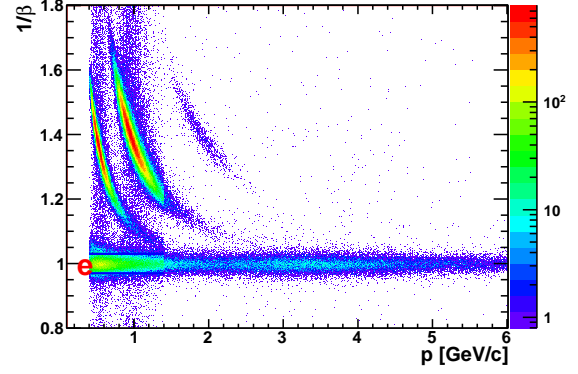
Figure 3.12: $1/\beta$ distribution as a function of momentum for particles that passed the TPC and BEMC ($p \geq 1.4$ GeV/c) eID cuts. The horizontal lines represent the range of the $1/\beta$ cut.

distance between a track and the matched BEMC tower. The distance, in the $\eta - \phi$ plane, between the track projected from the TPC and the center of a tower that the track projects to is always $R(\eta - \phi) \leq 0.035$.

The SMD is not used in this analysis. We checked that a cut on a number of SMD hits almost do not improve a significance and S/B ratio of observed J/ψ signal, but cause decrease of a number of observed J/ψ's.

Figure 3.13 shows the E/p distribution after the track quality and acceptance cuts (the $E \geq 0.1$ GeV cut is also applied). The E/p distribution after the TPC eID cuts is shown in Fig. 3.14. The vertical line represents the value of the E/p cut.

Below are listed electron identification cuts, and cuts assuring that a track matches to a given detector:

- $-1 < n\sigma_e < 2$

- $|1/\beta - 1| \leq 0.03$ for $p < 1.4$ GeV/c

- $|y_{Local}| \leq 2$ cm for $p < 1.4$ GeV/c

- $E/p \geq 0.5$ c (E - energy in a single BEMC tower) for $p \geq 1.4$ GeV/c

- $E \geq 0.1$ GeV for $p \geq 1.4$ GeV/c

58
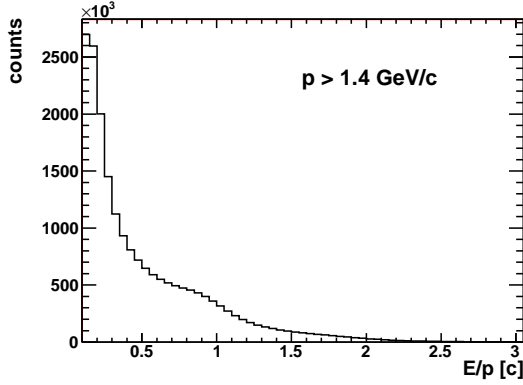
Figure 3.13: E/p distribution for particles that passed track quality and acceptance cuts. The distribution is for $p \geq 1.4$ GeV/c, where the E/p cut is used.
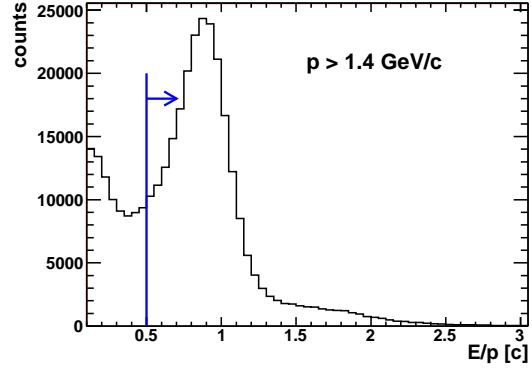
Figure 3.14: E/p distribution for particles that passed the TPC eID cuts. The vertical line represents a lower value of the E/p cut. The distribution is for $p \geq 1.4$ GeV/c, where the E/p cut is used.
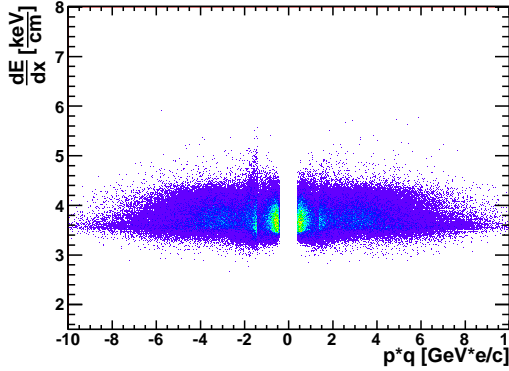
Figure 3.15: dE/dx distribution as a function of rigidity ($p * q$) for particles identified as electrons (after all eID cuts, the TOF cuts for $p < 1.4$ GeV/c and the BEMC cuts for $p \geq 1.4$ GeV/c).
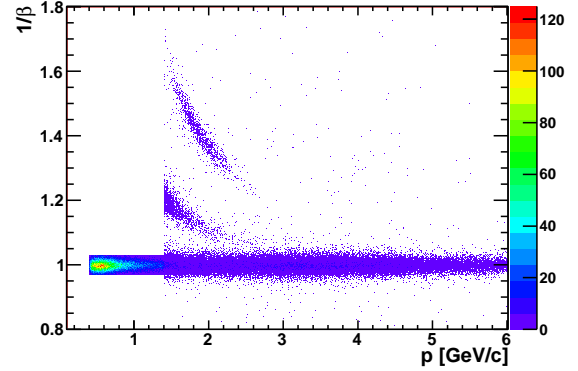
Figure 3.16: $1/\beta$ distribution as a function of momentum for particles identified as electrons (after all eID cuts, the TOF cuts for $p < 1.4$ GeV/c and the BEMC cuts for $p \geq 1.4$ GeV/c).

3.2.3 Summary

In summary, the applied cuts on events and track are gathered in Tab. 3.2:

Id	Cut	Comment
1	triggerId = 240570	event cuts
2	$\neg(|V_x| < 10^{-4} \wedge |V_y| < 10^{-4} \wedge |V_z| < 10^{-4})$ cm	
3	$|V_z| \leq 65$ cm	
4	$0 \leq flag < 1000$	track quality and acceptance cuts
5	$nFitPts \geq 15$	
6	$nFitPts/nFitPtsMax \geq 0.52$	
7	$DCA \leq 2$ cm	
8	$|\eta| \leq 1$	
9	$p_T \geq 0.4$ GeV/c	
10	at least one electron in an event that fired the HT trigger	the trigger condition: $11 < dsmAdc \leq 18$
11	$p_T \geq 2.5$ GeV/c	for an electron that fired the trigger
12	$-1 < n\sigma_e < 2$	eID cut
13	$|1/\beta - 1| \leq 0.03$	eID cut, for $p < 1.4$ GeV/c
14	$E/p \geq 0.5\,c$	eID cut, for $p \geq 1.4$ GeV/c, E - energy in a single BEMC tower
15	$|y_{Local}| \leq 2$ cm	TOF matching, for $p < 1.4$ GeV/c
16	$E \geq 0.1$ GeV	BEMC noise removal, for $p \geq 1.4$ GeV/c

Table 3.2: All cuts used in the analysis.

3.3 J/ψ signal and $cos\theta$ distributions

J/ψ signal is extracted using a statistical method. All electrons and positrons in an event are paired with each other and invariant mass (m_{ee}), p_T, rapidity (y) and $cos\theta$ of e^+e^- pairs are calculated. A combinatorial background (random, uncorrelated e^+e^- pairs) is calculated using the like-sign technique - the background is a sum of all e^+e^+ and e^-e^- ($N_{e^+e^+} + N_{e^-e^-}$) in an event. The J/ψ signal is obtained by subtracting the invariant mass distribution of the combinatorial background from the invariant mass distribution for all e^+e^- pairs. J/ψ's are identified as electron/positron pairs with the invariant mass range of $2.9 - 3.3\,\text{GeV}/c^2$. It is also required that a least one of electrons from a e^+e^- pair fired the HT trigger.

Figure 3.17 shows p_T and y distributions for all e^+e^- pairs and Fig.3.18 shows p_T and y distributions for the J/ψ signal after the background subtraction ($2.9 < m_{ee} < 3.3\,\text{GeV}/c^2$). The J/ψ y is between -1 and 1 and most of J/ψ's have p_T between 2 and 6 GeV/c.
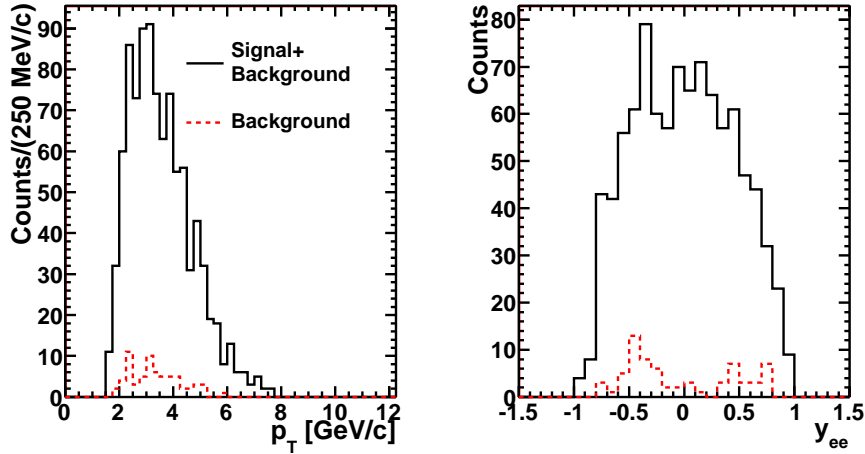
Figure 3.17: Left plot shows p_T and and right plot shows y distribution of unlike-sign pairs in black (solid line) and like-sign pairs that represent the combinatorial background in red (dashed line) for $2.9 < m_{ee} < 3.3\,\text{GeV}/c^2$.

3.3.1 J/ψ invariant mass distributions

Left plot in Fig. 3.19 shows an invariant mass distribution of electron/positron pairs with the combinatorial background, $2 < p_T < 6$ GeV/c and $|y| < 1$. The distribution after the combinatorial background subtraction is shown on a right plot in Fig. 3.19, the red line is J/ψ signal from a MC simulation which is discussed in section 3.4.1. Number of J/ψ ($N_{J/\psi}$), signal to
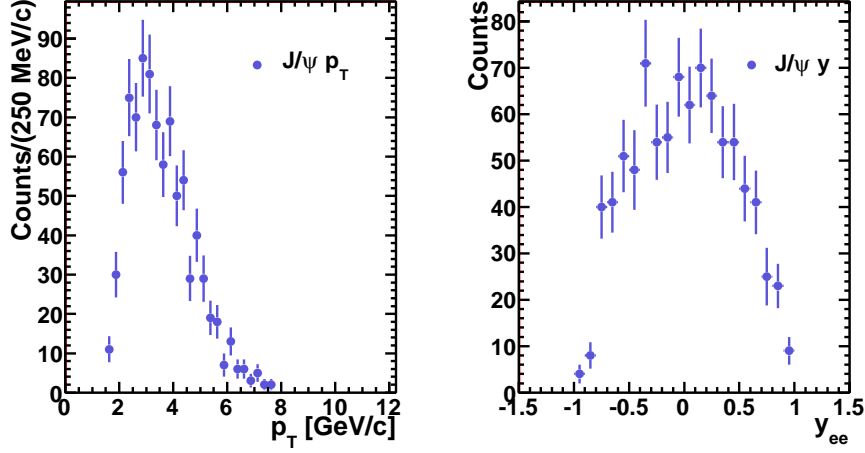
Figure 3.18: Left plots shows p_T and and right plot shows y distribution for J/ψ signal after the combinatorial background subtraction ($2.9 < m_{ee} < 3.3$ GeV/c^2).

background ratio (S/B) and the signal significance (sig) [8] in this p_T range are:

- $N_{J/\psi} = 791 \pm 30$

- $S/B = 14.7$, S - signal, B - background

- $sig = 26.4\sigma$

The significance of a signal is defined as a ratio of the signal to the statistical uncertainty of the signal:

$$sig = \frac{S}{\delta S} = \frac{S}{\sqrt{S + 2B}} \tag{3.3}$$

Since the polarization parameter λ_θ can be J/ψ p_T dependent, the obtained J/ψ signal is divided into three J/ψ p_T bins with comparable number of entries: $2 < p_T < 3$ GeV/c, $3 < p_T < 4$ GeV/c and $4 < p_T < 6$ GeV/c. The invariant mass distributions for that p_T bins are shown in Fig. 3.20, 3.21, 3.22. The distributions are for the full $cos\theta$ coverage, $-1 < cos\theta < 1$.

Number of J/ψ ($N_{J/\psi}$), signal to background ratio (S/B) and the signal significance (sig) in that p_T ranges are:

- $2 < p_T < 3$ GeV/c:

  - $N_{J/\psi} = 283 \pm 18$

  - $S/B = 14.2$

---

[8]see appendix B

(a) Unlike and like-sign pairs.

(b) J/ψ
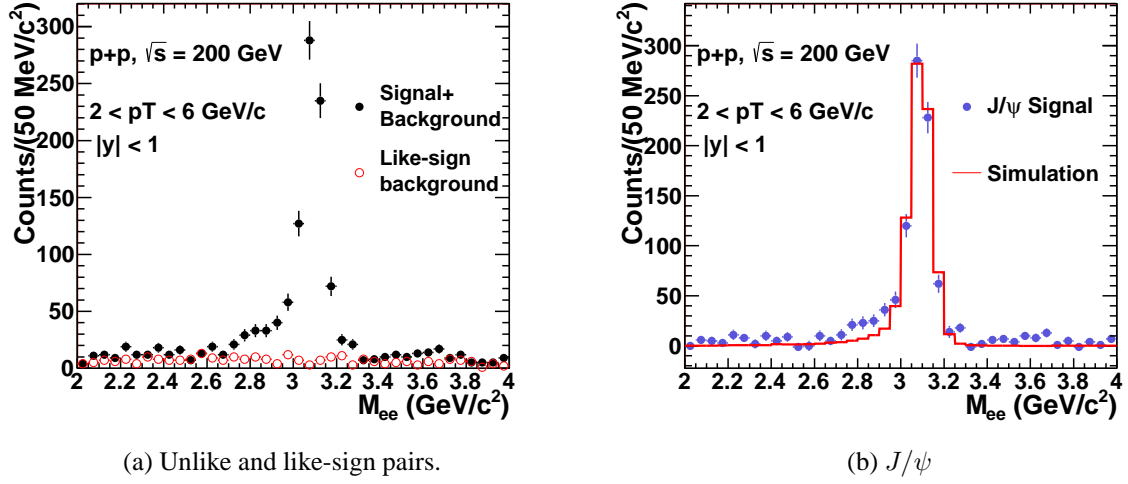
Figure 3.19: Invariant mass distributions of electron/positron pairs for $2 < p_T < 6$ GeV/c and $|y| < 1$. Plot (a) shows unlike-sign pairs in black (filled circles) and like-sign pairs that represent a combinatorial background in red (open circles). J/ψ signal to background ratio is ~15 and the signal significance is ~26 σ. Plot (b) shows J/ψ signal after the combinatorial background subtraction (blue filled circles), the red line is a MC simulation. Number of J/ψ in the mass range $2.9 < m_{e^+e^-} < 3.3$ GeV/c^2 is ~790.

- $sig = 15.7\sigma$

- $3 < p_T < 4$ GeV/c:

  - $N_{J/\psi} = 272 \pm 18$

  - $S/B = 13.6$

  - $sig = 15.4\sigma$

- $4 < p_T < 6$ GeV/c:

  - $N_{J/\psi} = 236 \pm 16$

  - $S/B = 16.9$

  - $sig = 14.5\sigma$

(a) Unlike and like-sign pairs.

(b) J/ψ
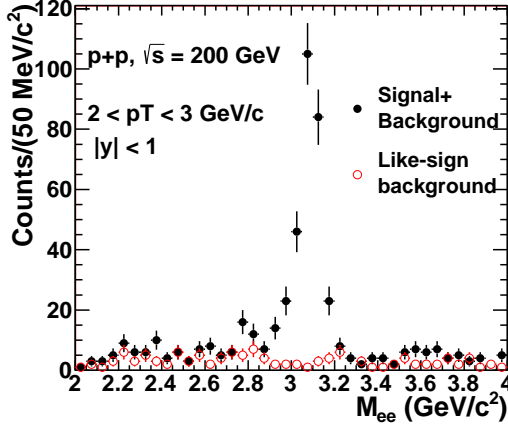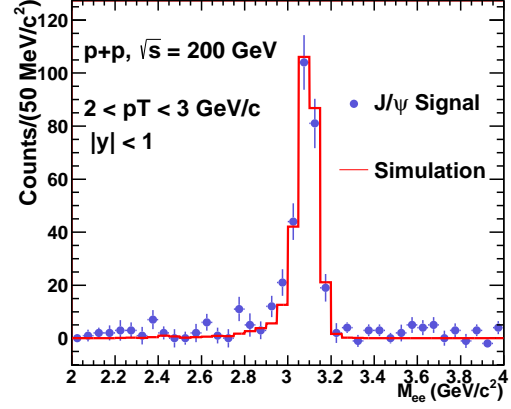
Figure 3.20: Invariant mass distributions of electron/positron pairs for $2 < p_T < 3$ GeV/c and $|y| < 1$. Plot (a) shows unlike-sign pairs in black (filled circles) and like-sign pairs that represent a combinatorial background in red (open circles). J/ψ signal to background ratio is ~ 14 and the signal significance is $\sim 16\ \sigma$. Plot (b) shows J/ψ signal after the combinatorial background subtraction (blue filled circles), the red line is a MC simulation. Number of J/ψ in the mass range $2.9 < m_{e^+e^-} < 3.3$ GeV/c^2 is ~ 280.

(a) Unlike and like-sign pairs.

(b) J/ψ
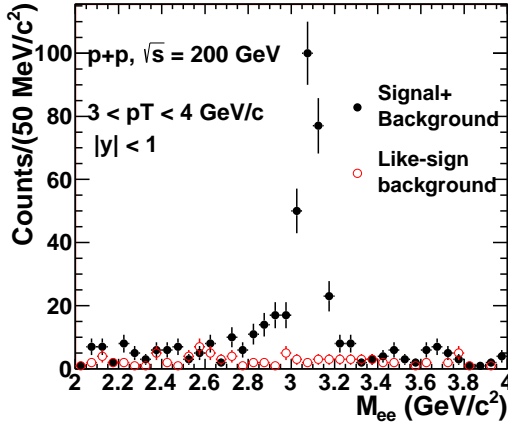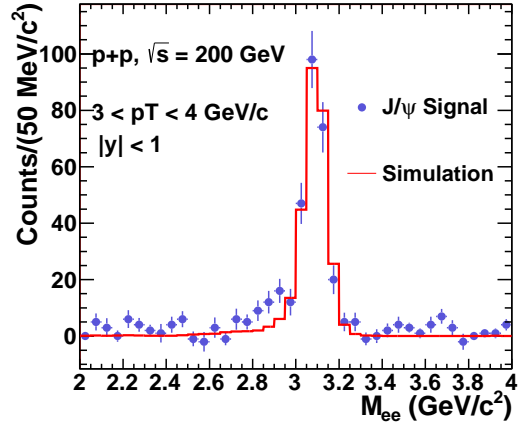
Figure 3.21: Invariant mass distributions of electron/positron pairs for $3 < p_T < 4$ GeV/c and $|y| < 1$. Plot (a) shows unlike-sign pairs in black (filled circles) and like-sign pairs that represent a combinatorial background in red (open circles). J/ψ signal to background ratio is ~ 14 and the signal significance is $\sim 15\ \sigma$. Plot (b) shows J/ψ signal after the combinatorial background subtraction (blue filled circles), the red line is a MC simulation. Number of J/ψ in the mass range $2.9 < m_{e^+e^-} < 3.3$ GeV/c^2 is ~ 270.

(a) Unlike and like-sign pairs.

(b) J/ψ
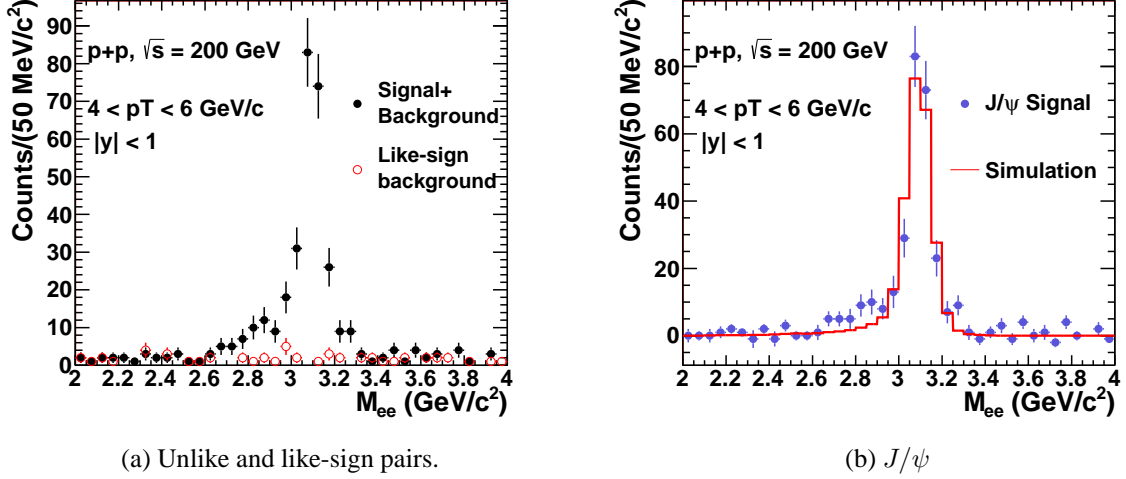
Figure 3.22: Invariant mass distributions of electron/positron pairs for $4 < p_T < 6$ GeV/c and $|y| < 1$. Plot (a) shows unlike-sign pairs in black (filled circles) and like-sign pairs that represent a combinatorial background in red (open circles). J/ψ signal to background ratio is ∼17 and the signal significance is ∼15 σ. Plot (b) shows J/ψ signal after the combinatorial background subtraction (blue filled circles), the red line is a MC simulation. Number of J/ψ in the mass range $2.9 < m_{e^+e^-} < 3.3$ GeV/c^2 is ∼240.

3.3.2 Uncorrected $cos\theta$ distributions

The polar angle θ is the angle between the positron momentum vector in the J/ψ rest frame and the J/ψ momentum vector in the laboratory frame. $cos\theta$ distributions, in each analysed J/ψ p_T bin are obtained by counting number of J/ψ ($N_{e^+e^-}$ - ($N_{e^+e^+}$ + $N_{e^-e^-}$) with $2.9 < m_{ee} < 3.3$ GeV/c^2) in each $cos\theta$ and J/ψ p_T bin. 10 bins in $cos\theta$ are used. An example of the invariant mass distributions in one of $cos\theta$ bins ($0.8 < cos\theta < 1$) and $2 < p_T < 3$ GeV/c is shown in Fig. 3.23.

Figure 3.24 shows uncorrected $cos\theta$ distributions for e^+e^- pairs before the background subtraction (black full circles) and $cos\theta$ distributions for the like-sign background (red open circles), in analysed p_T bins. Figure 3.25 shows $cos\theta$ distributions after the background subtraction.

65

(a) Unlike and like-sign pairs.

(b) J/ψ
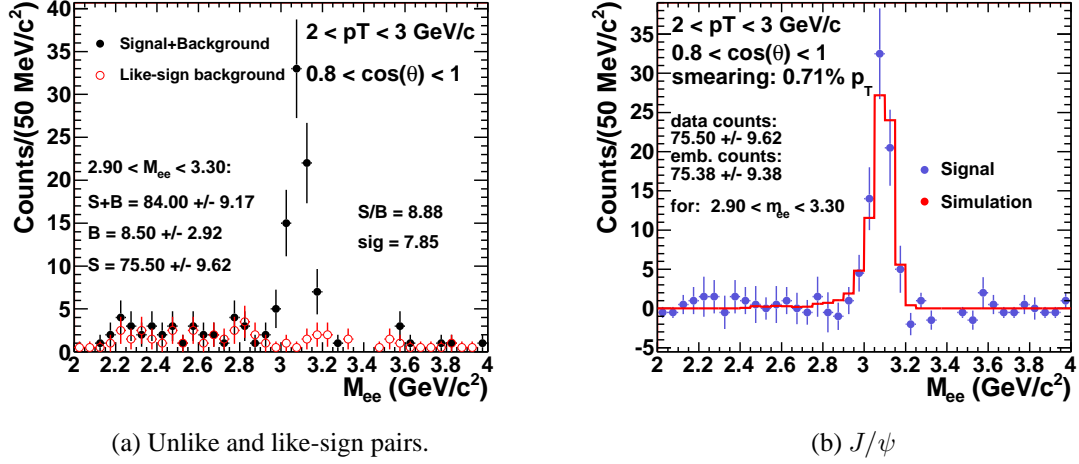
Figure 3.23: Invariant mass distributions of electron/positron pairs for $0.8 < cos\theta < 1$, $2 < p_T < 3$ GeV/c and $|y| < 1$. Plot (a) shows unlike-sign pairs in black (filled circles) and like-sign pairs that represent a combinatorial background in red (open circles). J/ψ signal to background ratio is $\sim$9 and the signal significance is $\sim$8 σ. Plot (b) shows J/ψ signal after the combinatorial background subtraction (blue filled circles), the red line is a MC simulation. Number of J/ψ in the mass range $2.9 < m_{e^+e^-} < 3.3$ GeV/c^2 is $\sim$75.

(a) $2 < p_T < 3$ GeV/c

(b) $3 < p_T < 4$ GeV/c

(c) $4 < p_T < 6$ GeV/c
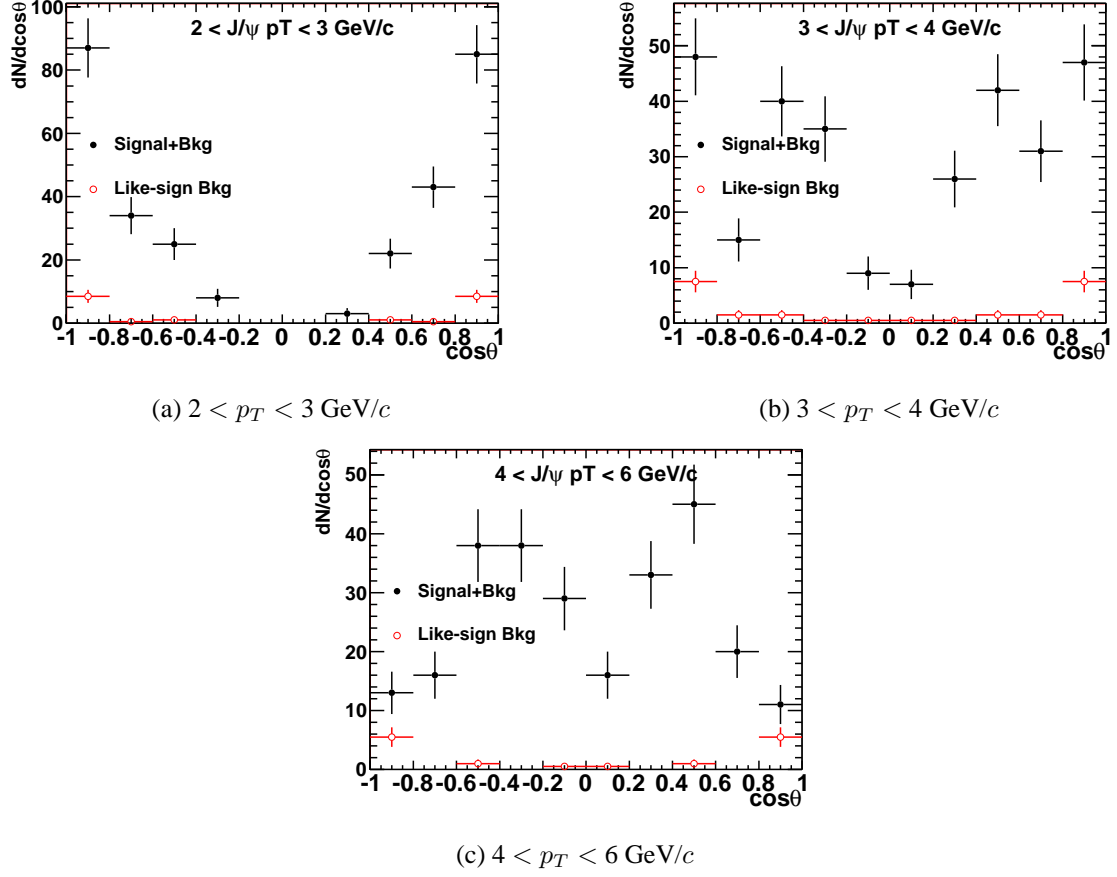
Figure 3.24: $cos\theta$ distributions for e^+e^- pairs before the background subtraction in black (full circles) and for the like-sign background in red (open circles), for each analysed p_T bin.

67

(a) $2 < p_T < 3$ GeV/c

(b) $3 < p_T < 4$ GeV/c

(c) $4 < p_T < 6$ GeV/c
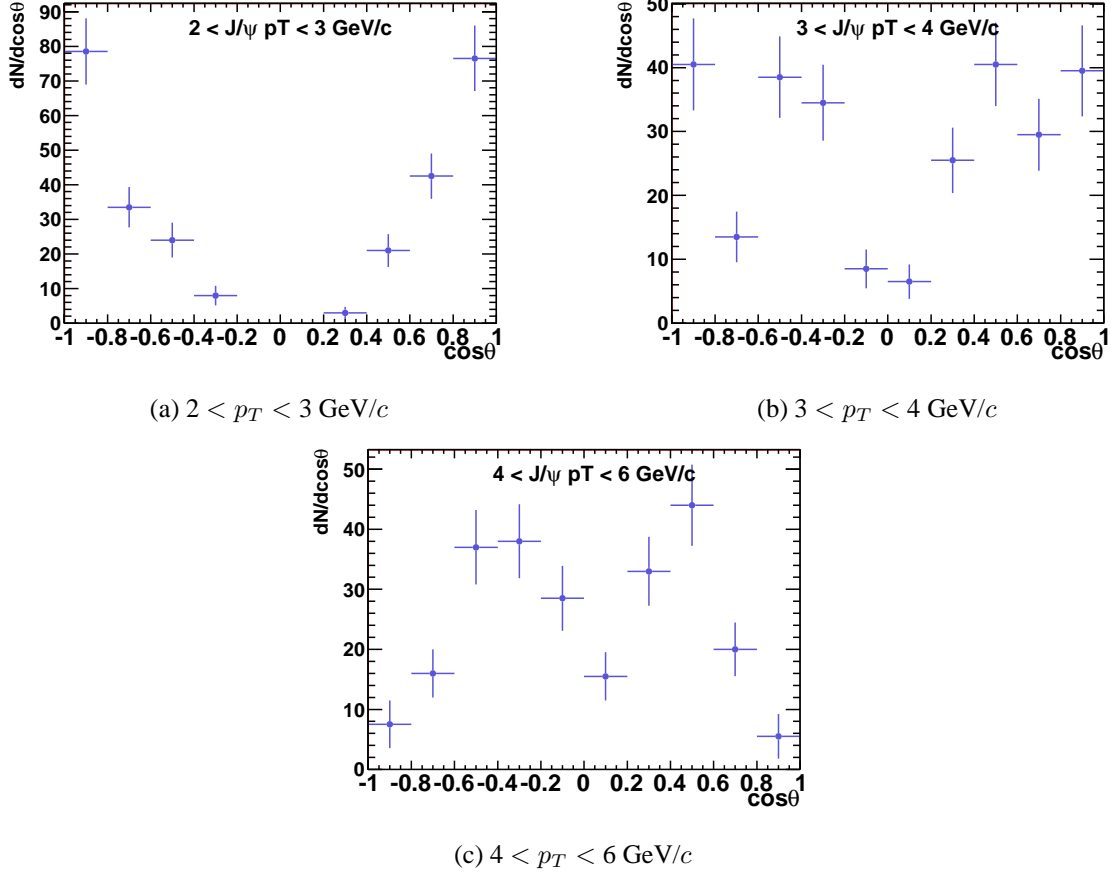
Figure 3.25: Uncorrected $cos\theta$ distributions after the combinatorial background subtraction, for each analysed p_T bin.

3.4 Efficiencies

Raw J/ψ distributions are corrected for the STAR detector acceptance, the tracks reconstruction efficiency, the electron identification efficiency and the efficiency of the High Tower trigger. All used in the data analysis cuts are taken into account. For that a Monte Carlo simulation is used, which is described in the following section 3.4.1.

3.4.1 J/ψ Monte Carlo simulation

We use Monte Carlo (MC) simulations to estimate the efficiency. This total efficiency contains detector acceptance, efficiencies of used track quality cuts and electron identification cuts and HT trigger efficiency. The MC J/ψ's are embedded into real events and the detector response is simulated. The procedure is called $embedding$.

In used embedding 3 Monte Carlo J/ψ (per event) were embedded into real events. In the

simulation, J/ψ decays only into one channel, e^+e^-. MC vertex distribution is taken from the real data. In order to save computing time, the input J/ψ p_T and rapidity distributions are simulated flat. p_T is simulated from 0 to 20 GeV/c and $|y| < 1.5$. Also, there is no J/ψ polarization in the embedding, the input $cos\theta$ distribution is flat.

The detector response is simulated using the GEANT software [76]. Then the TPC response for the simulated MC tracks is applied and the tracks are embedded into real events, in order to get the same environment as in the real data analysis. Next, the tracks are reconstructed in the TPC and associated with the MC tracks. At this point the TPC information for the electrons from the J/ψ decay can be used in the same way as it is done in the real data analysis.

After the TPC embedding, the BEMC embedding is done. The BEMC response is simulated with the same calibration tables that were used for the real data. And the response is superimposed with the real BEMC data. The simulated BEMC hits are embedded for towers which had a good status during the data taking. Finally, the simulated particles have to be associated with the BEMC hits.

Basic distributions for electrons, from J/ψ decay, from embedding were compared with distributions for electrons from the data, and reasonable agreement was found. Small differences between the simulation and data are taken into account in systematic uncertainties estimation.

3.4.1.1 Input J/ψ p_T and rapidity weighting

J/ψ's are embedded into real events with uniform p_T and rapidity distributions. Then, the p_T and y distributions are weighted according to experimental shapes.

The p_T weight is found by fitting function from Eq. 3.4 to PHENIX (2006 data [29]) and STAR (2009 high-p_T preliminary result [57]) J/ψ p_T spectrum. The spectrum with the fitted function is shown in Fig. 3.26.

$$f(p_T) = A(1 + (\frac{p_T}{B})^2)^{-6} \tag{3.4}$$

Obtained values of the fitting parameters, in the p_T range from 0 to 10 GeV/c, are:

- $A = 4.23 \pm 4.23$

- $B = 4.10 \pm 0.13$

So, the p_T weight is:

$$w_{p_T}^{J/\psi} = 4.32(1 + (\frac{p_T}{4.10})^2)^{-6} \times p_T \tag{3.5}$$
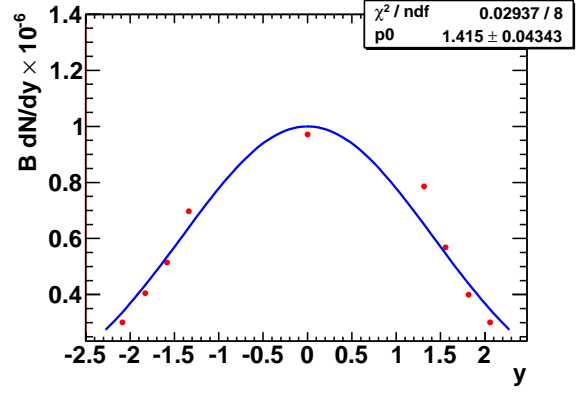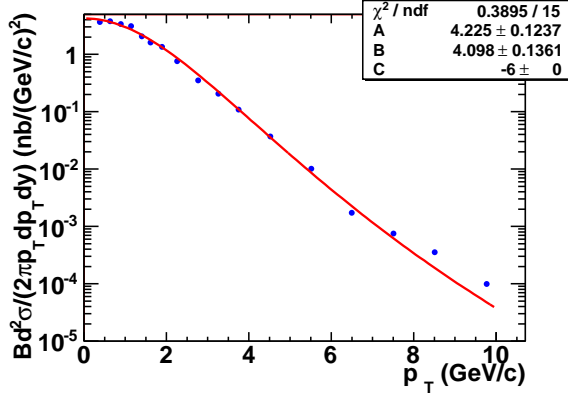
Figure 3.26: J/ψ p_T spectrum with function from Eq. 3.4 fitted in p_T range from 0 to 10 GeV/c.

Figure 3.27: J/ψ rapidity distribution with the Gaussian function (Eq. 3.6) fitted.

To estimate the weight for y distribution, data from the PHENIX experiment [29] are used. Figure 3.27 shows the y distribution with the Gaussian function fitted to the data:

$$\exp(-\frac{0.5y^2}{A^2}) \qquad (3.6)$$

Obtained value of the fitting parameter is: $A = 1.42 \pm 0.04$. So, the rapidity weight is:

$$w_y^{J/\psi} = \exp(-\frac{0.5y^2}{1.416^2}) \qquad (3.7)$$

A total input weight, $w_{input}^{J/\psi}$, is a product of the p_T weight the and y weight:

$$w_{input}^{J/\psi} = w_{p_T}^{J/\psi} \times w_y^{J/\psi} \qquad (3.8)$$

3.4.1.2   Cuts and weighting

The same procedure is applied in the embedding analysis as in the data analysis. The same cuts as those used in the data analysis, listed in the table 3.2, are used. Track quality, acceptance and the BEMC cuts as well as the HT trigger conditions are directly applied in the embedding analysis code. Matching to the BEMC is done in the same way as in the data analysis, i.e. a reconstructed TPC track is projected to the BEMC and a tower that the track projects to is taken. Since dE/dx $n\sigma_e$ and TOF conditions are not well simulated in the embedding, efficiencies of the $n\sigma_e$ cut and the TOF cuts, for single electrons, are calculated from the data. The TPC eID ($n\sigma_e$ cut) efficiency is obtained as a function of momentum. The TOF matching efficiency, with the efficiency of the $1/\beta$ cut, is used as a function of η. This efficiencies are applied in the embedding code as a weight - w_{eID}^e, as it is discussed in Sec. 3.4.3.

The final weight consist of both w_{eID}^e and $w_{input}^{J/\psi}$: $w_{eID}^{J/\psi} \times w_{input}^{J/\psi}$.

70

3.4.1.3 J/ψ signal

The invariant mass distribution of the J/ψ signal obtained from the embedding (so called the J/ψ lineshape) is shown in Fig. 3.28a, along with the J/ψ signal from the data, for $2 < p_T < 6$ GeV/c. The J/ψ lineshape is obtained after applying all analysis cuts and weights.
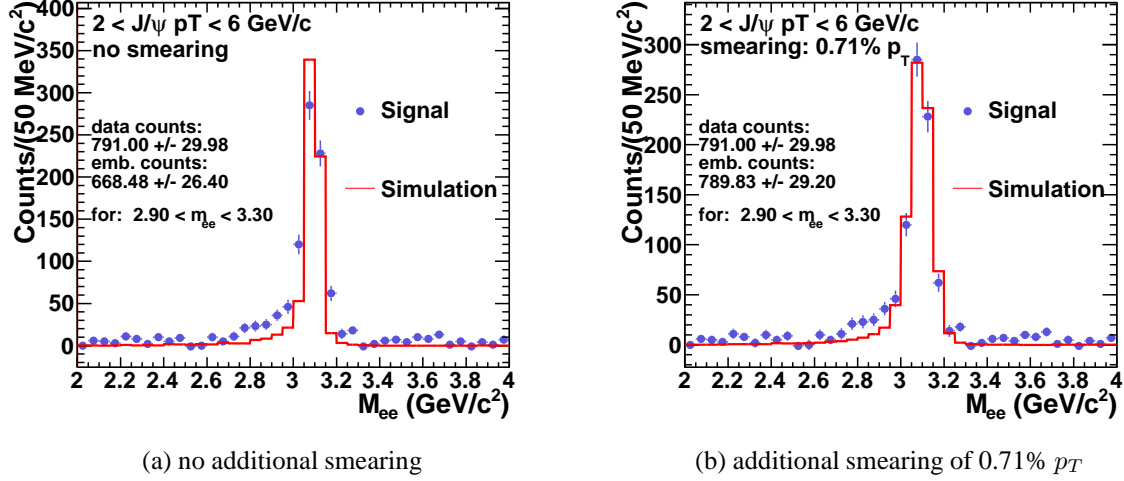
(a) no additional smearing

(b) additional smearing of 0.71% p_T

Figure 3.28: The J/ψ signal after the combinatorial background subtraction (blue filled circles) with the J/ψ signal from the embedding (red line). Plot (a) shows the embedding lineshape without applying additional smearing on the embedding momentum. Plot (b) shows the embedding lineshape with the additional p_T smearing of 0.71% p_T.

The J/ψ signal from the simulation is narrower than the J/ψ signal obtained from the data. Observed in the experiment width of the J/ψ signal depends on the detector resolution. The smaller width of the J/ψ signal in the embedding from the width of the signal in the data suggests that the TPC resolution is underestimated in the embedding. Figure 3.29 shows a p_T resolution from the embedding. The resolution is calculated as:

$$\frac{\delta p_T}{p_T^{MC}} = \frac{p_T^{MC} - p_T^{RC}}{p_T^{MC}} \tag{3.9}$$

where p_T^{MC} is Monte Carlo transverse momentum and p_T^{RC} is reconstructed p_T. Figure 3.29b shows the width of Gaussian functions fitted to the distribution of the p_T resolution in small p_T^{MC} intervals.

In order to better represent the detector conditions in the simulation, an additional Gaussian component is added to the p_T resolution from the embedding (additional p_T smearing). The Gaussian parameters are:

- mean: $\mu = 0$

(a) Width   (b) Mean
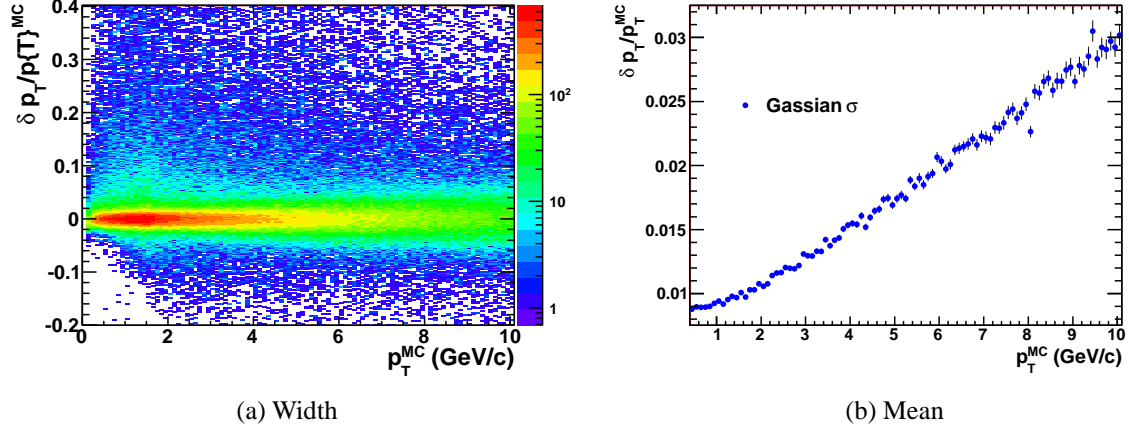
Figure 3.29: The p_T resolution from the embedding. Plot (b) shows the width of Gaussian functions fitted to the distribution of the p_T resolution in small p_T^{MC} intervals.

- width: $\sigma_A = A \times p_T$

where A is a smearing parameter.

To find the best value of the smearing parameter, a χ^2 minimization is done. J/ψ signal from the simulation with the additional smearing of p_T is compared to the J/ψ signal from the data and χ^2 value is determined, for each value of the smearing parameter A from 0 to 1% p_T with a step of 0.01% p_T. A 6th order polynomial is fitted to a distribution of χ^2 as a function of A. The best value of A is where χ^2 distribution reaches a minimum. An error on the smearing parameter is determined as a range of A where $\Delta\chi^2$ around the minimum χ^2 is equal to 1. The J/ψ signal from the data and the embedding are compared for $2 < J/\psi \ p_T < 6\,\text{GeV}/c$, the whole p_T range used in the analysis. The χ^2 distribution as a function of A is shown in Fig. 3.30. The smearing parameter for χ^2_{min}: $A = 0.71 \pm 0.05$ %. Vertical lines represent a χ^2 range of $\Delta\chi^2 = 1$, used to estimate the error on the smearing parameter.

The χ^2 minimization was also done for narrower J/$\psi \ p_T$ bins used in the analysis: $2 < p_T < 3\,\text{GeV}/c$, $3 < p_T < 4\,\text{GeV}/c$ and $4 < p_T < 6\,\text{GeV}/c$. Although, a small smearing parameter dependence of p_T was observed, which could be due to statistical fluctuations, obtained values of A agree with each other within the errors. In order to avoid fluctuation effects, one value of the smearing parameter for the whole J/$\psi \ p_T$ range is applied in the embedding analysis.

The best value of A is 0.71 ± 0.05 %, and the Gaussian parameters, used for additional p_T smearing are $\mu = 0$ and $\sigma_A = 0.71 \pm 0.05$ % p_T, where p_T is the Monte Carlo p_T. The J/ψ signal with additional smearing of the p_T of 0.71% p_T is shown in Fig. 3.28b.

Efficiencies are calculated as a function of Monte Carlo variables, so they are not influenced
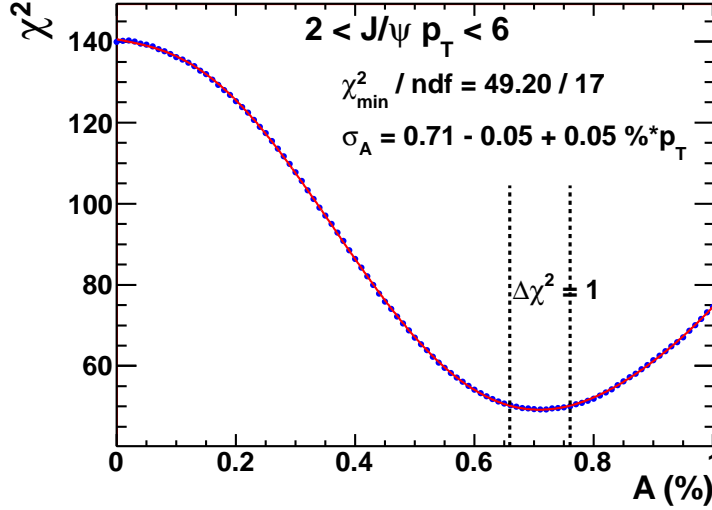
Figure 3.30: The χ^2 distribution as a function of A. Smearing for χ^2_{min}: $\sigma_A = 0.71 \pm 0.05$ % p_T. Vertical lines represent a χ^2 range of $\chi^2_{min} \pm 1$ used to determine the A error.

by the additional smearing of the p_T resolution. The additional smearing is done in order to obtain $cos\theta$ distributions from the simulated J/ψ signal, which has to properly describe the J/ψ signal from the data. This is a second method of determining $cos\theta$ distributions and is included in systematic uncertainties estimation (Sec. 5.1). The error on the smearing parameter is also taken into account.

3.4.2 Single electron efficiencies from the data

In next sub-sections efficiencies for single electrons obtained from the data are discussed. Data are used to calculate efficiencies of the $n\sigma_e$ cut and the TOF cuts. This efficiencies are later used for a total J/ψ efficiency calculation, as it is described in section 3.4.3.

Other cuts efficiencies are obtained directly for J/ψ, using the MC simulation. It is discussed in Sec. 3.4.3. For a systematic uncertainties estimation, these efficiencies are also calculated for electrons from the J/ψ decay from the embedding and compared with those obtained from the data, as it is shown in Sec. 5.

3.4.2.1 TPC electron identification efficiency

Electrons are identified in the TPC using dE/dx information, the cut of $-1 < n\sigma_e < 2$ is applied. The efficiency of the $n\sigma_e$ cut ($\epsilon_{n\sigma_e}$) is calculated as a ratio of a number of electrons that passed the $n\sigma_e$ ($N_{n\sigma_e}$) cut to the number of electrons in the TPC (N_{TPC}), that passed track

quality and acceptance cuts, as a function of momentum:

$$\epsilon_{n\sigma_e}(p) = \frac{N_{n\sigma_e}(p)}{N_{TPC}(p)} \tag{3.10}$$

The σ_e distribution for electrons has the Gaussian shape. For small momentum intervals the σ_e for hadrons can be approximated with the Gaussian as well. So the σ_e distributions for all particles can be approximated with a sum of Gaussian functions, in small momentum intervals. The Gaussian function for each particle species has different mean (μ) and width (σ). For example, the Gaussian function for electrons is:

$$f(n\sigma_e) = A e^{(n\sigma_e - \mu_e)^2 / 2\sigma_e} \tag{3.11}$$

The σ_e distribution for electrons and hadrons, before the σ_e cut, is fitted with a sum of Gaussian functions, as it is shown later in Fig. 3.33. Although for $p < 1.4$ GeV/c the TOF is used to reject hadrons and for higher momenta the BEMC is used, there is still a lot of hadrons in the sample which may influence a position of the Gaussian fit for electrons. The fitting is particularly difficult in momentum ranges where hadron bands cross or approach the electron band. An independent fit for μ_e and σ_e for electrons is perform using an electron sample with high purity. Then, this parameters are used in the sum of Gaussian functions fit, to improve the fitting.

The high-purity electrons sample is obtained by selecting photonic electrons [9], with the invariant mass of a pair less than 0.1 GeV/c^2. In addition, for $p < 1.5$ GeV/c the $|1/\beta - 1| \leq 0.03$ cut is applied and for momenta greater than 1.5 GeV/c the $E/p \geq 0.5$ cut is used in order to reject possible hadron contamination. Figure 3.31 shows the $n\sigma_e$ distribution for $0.4 < p < 1$ GeV/c. The red distribution (full squares) is for particles from unlike-sign pairs and the blue one (open squares) is for particles from like-sign pairs (the combinatorial background). The black distribution (unlike-like, full circles) is a high purity electron sample which is obtained by subtracting the like-sign distribution from the unlike-sign distribution. The $n\sigma_e$ distribution for electrons (black distribution) is fitted with the Gaussian function (the green function), see Eq. 3.11, without any constraints applied on the fit. Obtained values of the Gaussian mean and width, for momentum range $0.4 < p < 1$ GeV/c, are: μ_e = -0.103 $\pm$ 0.009 and σ_e = 0.852 $\pm$ 0.007. An efficiency of the $-1 < n\sigma_e < 2$ cut is 84.7 $\pm$ 0.8 %.

The same procedure is applied to other momentum bins and Fig. 3.32 shows distributions of mean and width of the Gaussian fits for electrons as a function of p. In order to avoid fluctuations

---

[9]from photon conversion in the detector material and Dalitz decay of π^0 and η mesons
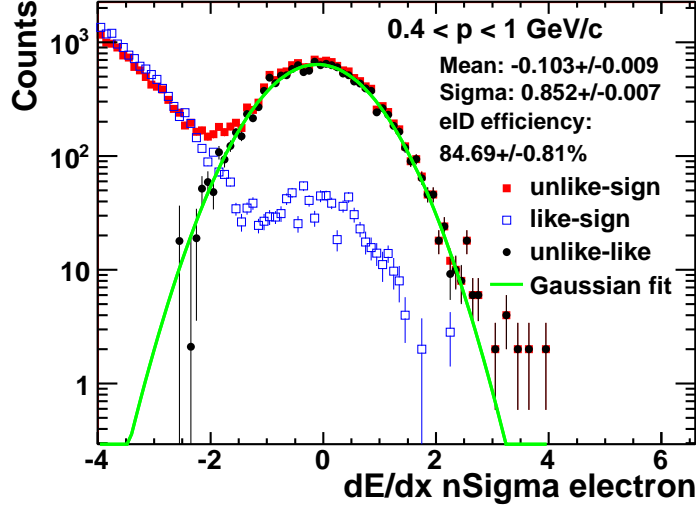
Figure 3.31: $n\sigma_e$ distribution for photonic electrons, for $0.4 < p < 1$ GeV/c. The black distribution is a high purity electron sample (the unlike-sign distribution after the like-sign distribution subtraction) with the Gaussian function fitted. Obtained values of the Gaussian mean and width are: μ_e = -0.103 $\pm$ 0.009 and σ_e = 0.852 $\pm$ 0.007, respectively. An efficiency of the $-1 < n\sigma_e < 2$ cut, in shown momentum bin, is 84.7 $\pm$ 0.8 %.

effects, constant functions are fitted to μ_e and σ_e points. 1σ uncertainty on the mean is obtained by moving the μ_e points up and down by their 1σ uncertainty and fitting a constant function. In the same way 1σ uncertainty on the width for electrons is obtained. In the ideal case the μ_e should be 0 and σ_e should be 1. But due to dE/dx calibration effects the real μ_e and σ_e could vary from the theoretical values. Obtained values of μ_e and σ_e are:

- μ_e = -0.029 $\pm$ 0.022

- σ_e = 0.839 $\pm$ 0.015

In principle, the efficiency of the $n\sigma_e$ cut can be calculated using the photonic electrons. But due to a small sample which is mostly up to 4.5 GeV/c only, the efficiency is calculated using inclusive electrons (without the invariant mass cut), with constraints on the Gaussian mean and width obtained from the photonic electrons sample analysis. The efficiency obtained from the photonic electrons sample is shown in Fig. 3.34 and agrees, within the errors, with the final efficiency obtained using the inclusive electrons sample. The efficiency is calculated using the Eq. 3.12.

The obtained constraints for the Gaussian fit for electrons can be adopted to the analysis of inclusive electrons. For that analysis 3σ ranges around the central values obtained for the mean
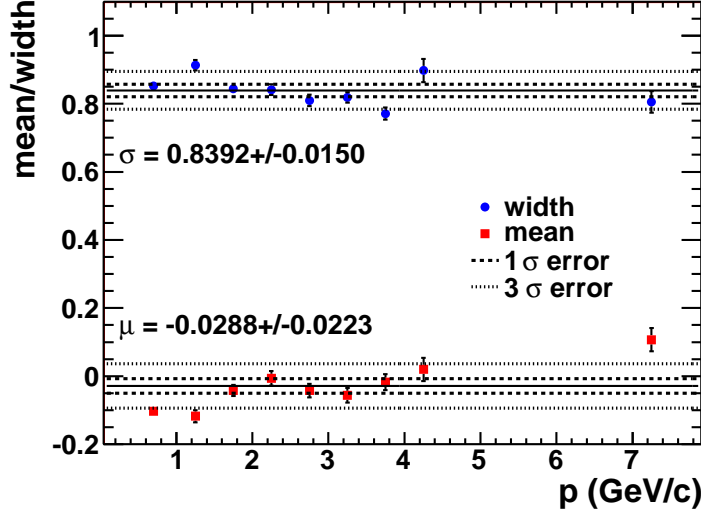
Figure 3.32: Distributions of the mean (red full squares) and width (blue filled circles) of the Gaussian fits to $n\sigma_e$ distributions for photonic electrons as a function of momentum. The mean and width obtained from a constant fit are: $\mu_e = -0.029 \pm 0.022$ and $\sigma_e = 0.839 \pm 0.015$, respectively. Dashed lines represent 1σ uncertainty ranges and dotted lines represent 3σ uncertainty ranges, for mean and width.

and width from the photonic electrons analysis (dotted lines in Fig. 3.32) are used as limits on the mean and width of the Gaussian fit for electrons. Fits for hadrons are also guided, using the Bischel function predictions. To get a purer electron sample, the TOF and BEMC eID cuts from the data analysis are applied, see table 3.2.

Fig. 3.33 shows $n\sigma_e$ distribution for inclusive electrons sample with the sum of Gaussian functions fitted. The left plot is for $0.4 < p < 0.6$ GeV/c and the right plot is for $3.6 < p < 3.8$ GeV/c. The red Gaussian is for electrons, the blue line is for pions and the green one is for protons, Kaons dE/dx merges with other hadrons. Solid black line is the sum of Gaussian functions and the shaded area are electron candidates after applying all electron identification cuts. The same multi-Gaussian fitting is done for other momentum ranges and the corresponding distributions are shown in appendix A.2. The $n\sigma_e$ cut efficiency is obtained from the Gaussian fit for the electrons ($f(n\sigma_e)$) as a fraction of electrons satisfying $-1 < n\sigma_e < 2$ cut:

$$\epsilon_{n\sigma_e}(p) = \frac{\int_{-1}^{2} f(n\sigma_e)}{\int_{-10}^{10} f(n\sigma_e)} \tag{3.12}$$

The $n\sigma_e$ cut efficiency as a function of momentum is shown in Fig. 3.34 as blue full circles. The plot also shows the efficiency obtained using the photonic electrons (red full squares), as

(a) $0.4 < p < 0.6$ GeV/c

(b) $3.6 < p < 3.8$ GeV/c
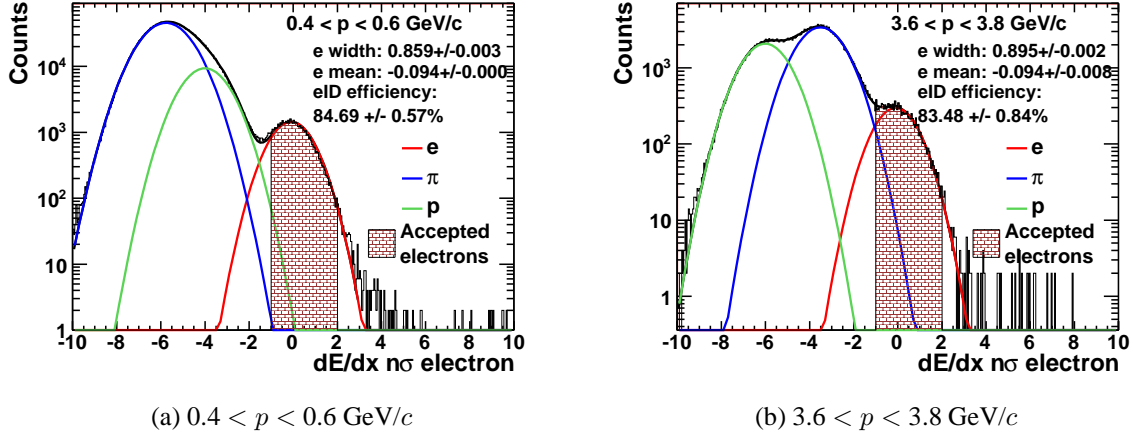
Figure 3.33: $n\sigma_e$ distribution in black with the sum of three Gaussian functions fitted. The red line is for electrons, the blue one is for pions and the green line is for protons, kaons dE/dx merges with other hadrons. The shaded area are electrons after all electron identification cuts. The $-1 < n\sigma_e < 2$ cut efficiency is calculated using Eq. 3.12. The left plot is for $0.4 < p < 0.6$ GeV/c and the right one is for $3.6 < p < 3.8$ GeV/c.

a cross-check. The two efficiencies agree with each other within the errors. The uncertainty on the efficiency is determined from the error on the integral which is used in the efficiency calculation (Eq. 3.12), taking into account correlations between the fitting parameters.

The blue band is the uncertainty of the efficiency, which is determined by changing the constraints on the Gaussian fit for electrons. The procedure is described in Sec. 5.6.

3.4.2.2 TOF matching and electron identification efficiency

For $p < 1.4$ GeV/c electrons are identified using information from the TOF detector, with the $|1/\beta - 1| \leq 0.03$ cut which does not depend on electron momentum.

In order to ensure that tracks from the TPC, that were detected in the TOF detector, are correctly matched to the TOF, an additional cut of $|y_{Local}| \leq 2$ cm is used. In 2009 there was 72% of the full TOF installed and due to a different number of TOF trays installed on the West and East sites of the TPC, the matching to the TOF is strongly η dependent. There is almost no p_T dependence, as it is shown in the next section. Therefore, the matching efficiency to the TOF is used as a function of η, $\epsilon_{TOFmatching}(\eta)$.

A total TOF efficiency is a product of the matching efficiency to the TOF and the efficiency of the $1/\beta$ cut:

$$\epsilon_{TOF}(\eta) = \epsilon_{TOFmatching}(\eta) \times \epsilon_\beta \tag{3.13}$$
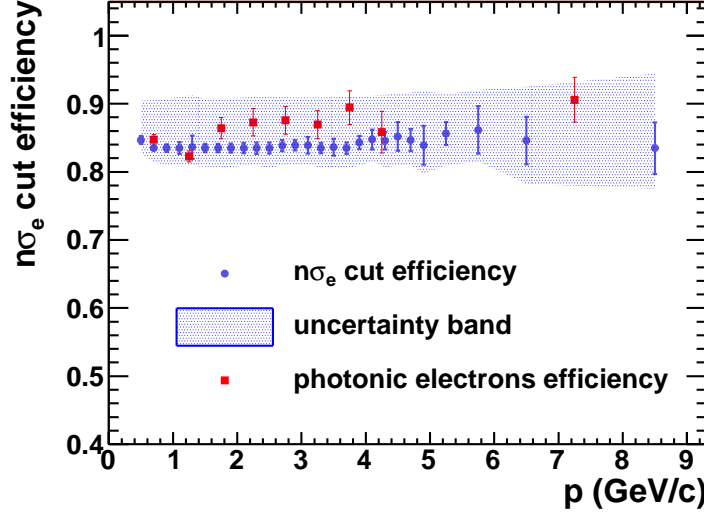
Figure 3.34: $-1 < n\sigma_e < 2$ cut efficiency as a function of momentum (blue full circle) with the uncertainty band (blued shaded area). The efficiency obtained using the photonic electrons is shown as red full squares.

TOF matching efficiency

The TOF matching efficiency for electrons is defined as a number of electrons that match the TOF and pass the $|y_{Local}| \leq 2$ cm cut ($N^e_{TOF\&y_{Local}}$) divided by a number of electrons in the TPC (N^e_{TPC}), that pass the track quality and acceptance cuts:

$$\epsilon_{TOFmatching} = \frac{N^e_{TOF\&y_{Local}}}{N^e_{TPC}} \tag{3.14}$$

The TOF matching efficiency cannot be studied from the analyzed HT triggered data since the denominator in Eq. 3.14 would contain tracks from a pile-up, which are seen in the TPC. In the main analysis, the pile-up is removed by matching tracks to the TOF, which is a fast detector. Here, because the TOF matching efficiency is studied itself, this method of removing the pile-up cannot be used. Because of that, data with low luminosity (*pp2pp* data), that are almost without the pile-up, are used.

At lower momenta, where the TOF is used, it is not possible to obtain a pure electron sample, with a reasonable good statistics, using the TPC cuts alone. At the lower momentum range, the dE/dx bands for hadrons overlap with the electron band, and $n\sigma$ cuts that can reject hadrons would remove a lot of electrons at the same time. So the matching to the TOF is calculated using a hadron sample and then scaled. Matching efficiencies for electrons and hadrons are calculated as a function of transverse momentum, as is show Fig. 3.35, the matching efficiency for electrons in red (full circles) and for hadrons in blue (open circles).
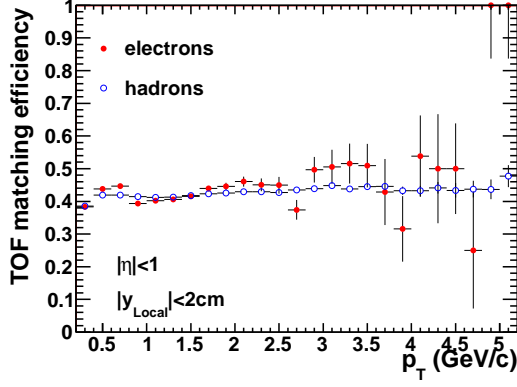
Figure 3.35: TOF matching efficiency, with the $|y_{Local}| \leq 2$ cm cut, as a function of p_T for electrons in red (full circles) and hadrons in blue (open circles), $-1 \leq \eta \leq 1$ and $-180° \leq \phi \leq 180°$.
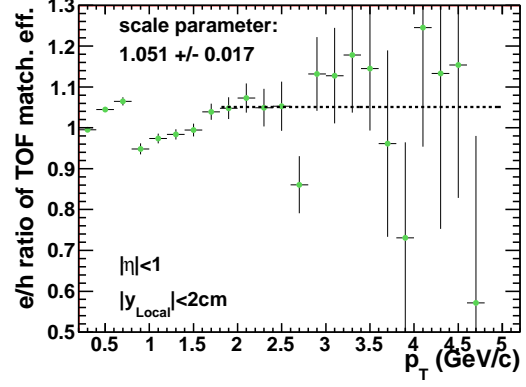
Figure 3.36: Ratio of the electron to hadron TOF matching efficiency with a constant function fitted for $p_T > 1.8$ GeV/c. The scale parameter is 1.051 ± 0.017.

At $p_T \lesssim 1.8$ GeV/c, a purity of the electron sample is low. So a scale parameter is determined at transverse momenta greater than 1.8 GeV/c, at this higher p_T range it is much easier to get a pure electron sample using dE/dx cuts only. The scale parameter is obtained by dividing the matching efficiency for electrons by the matching efficiency for hadrons, as a function of p_T, for $p_T > 1.8$ GeV/c. The ratio of the electron to hadron matching efficiency is show in Fig. 3.36. The scale parameter is obtained by fitting a constant function to the ratio, for $p_T > 1.8$ GeV/c, and a one value of the parameter is obtained: 1.051 ± 0.017.

Using the obtained scale parameter, the matching efficiency for electrons can be calculated from the hadron efficiency. Described below matching efficiencies for electrons are hadron efficiencies scaled by 1.051.

The matching efficiency for electrons (with the $|y_{Local}| \leq 2$ cm cut) as a function of p_T for different η ranges and for full azimuthal angle ($-180° \leq \phi \leq 180°$) is shown in Fig. 3.37. The vertical line represents the p_T cut in the data analysis. Shown errors are statistical (calculated using the Binomial distribution [78]) and from the scale parameter uncertainty. The efficiency almost does not depend on p_T for all η bins, but is strongly η dependent.

Figure 3.38 shows the matching efficiency as a function of η for $0.4 \leq p_T < 1.4$ GeV/c and $-180° \leq \phi \leq 180°$. Errors combine statistical and scale parameter uncertainties. In further analysis the TOF matching efficiency is applied as a function of η.

The number of installed TOF trays also depends on ϕ. The matching efficiency as a function

Figure 3.37: TOF matching efficiency for electrons, with the $|y_{Local}| \leq 2$ cm cut, as a function of p_T for different η ranges and -180°$\leq \phi \leq$ 180°. The vertical line represents the p_T cut in the data analysis. Almost no p_T dependence is observed.

Figure 3.38: TOF matching efficiency for electrons, with the $|y_{Local}| \leq 2$ cm cut, as a function of η for $0.4 \leq p_T < 1.4$ GeV/c and -180°$\leq \phi \leq$ 180°. Difference in $\eta < 0$ and $\eta > 0$ is due to different number of installed TOF trays.

(a) Electrons

(b) Positrons

Figure 3.39: TOF matching efficiency for electrons, with the $|y_{Local}| \leq 2$ cm cut, as a function of ϕ for -1 < η < -0.4 and $0.4 \leq p_T < 1.4$ GeV/c. Plot 3.39a is for electrons and plot 3.39b is for positrons.

of ϕ for $0.4 \leq p_T < 1.4$ GeV/c is shown in Fig. 3.39 and 3.40 for two TPC sites. Figure 3.39 shows the efficiency for -1 < η < -0.4 and Fig. 3.40 shows the efficiency for 0.4 < η < 1. Left plots are for electrons and right plots are for positrons. Gaps in the distributions are due to the missing TOF trays.

(a) Electrons
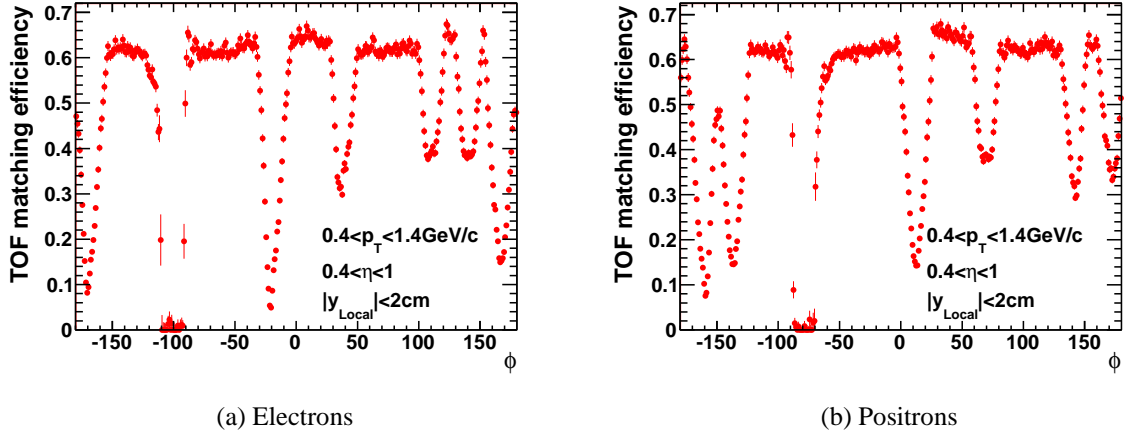
(b) Positrons

Figure 3.40: TOF matching efficiency for electrons, with the $|y_{Local}| \leq 2$ cm cut, as a function of ϕ for 0.4 < η < 1 and $0.4 \leq p_T < 1.4$ GeV/c. Plot 3.40a is for electrons and plot 3.40b is for positrons.

The distributions can be divided in three bins with significantly different efficiency in ϕ: -180°$\leq \phi$ < -123°, -123°$\leq \phi$ < -63°and -63°$\leq \phi \leq$ 180 °. Figure 3.41 show the matching efficiency as a function of η for that three ϕ bins. Applying the efficiency in three ϕ bins instead of the efficiency integrated over the ϕ has small influence on the final polarization result and is
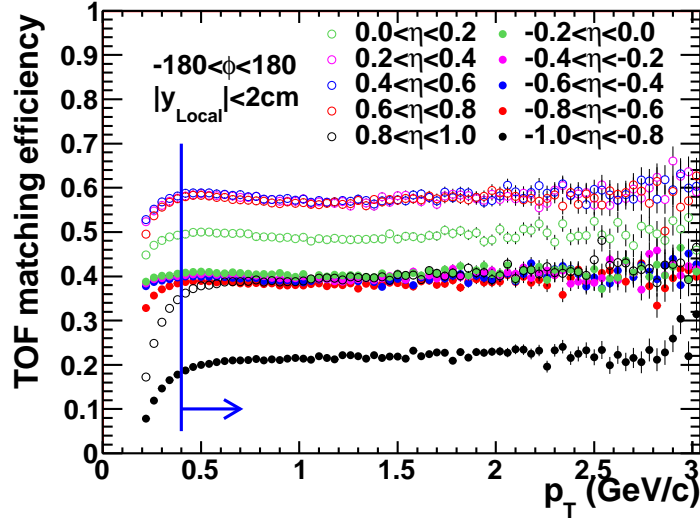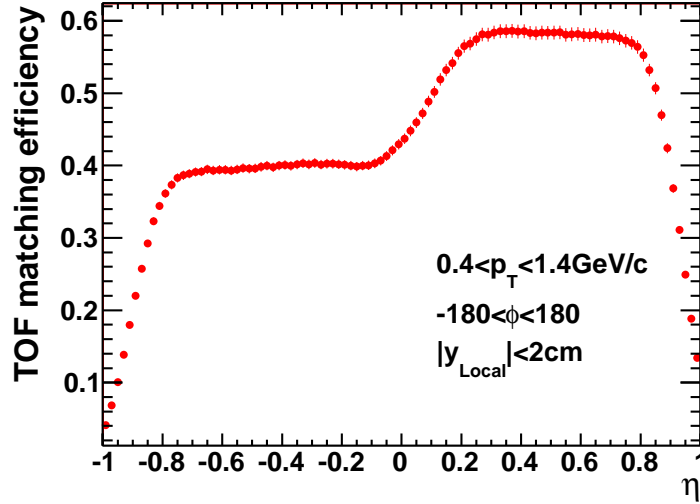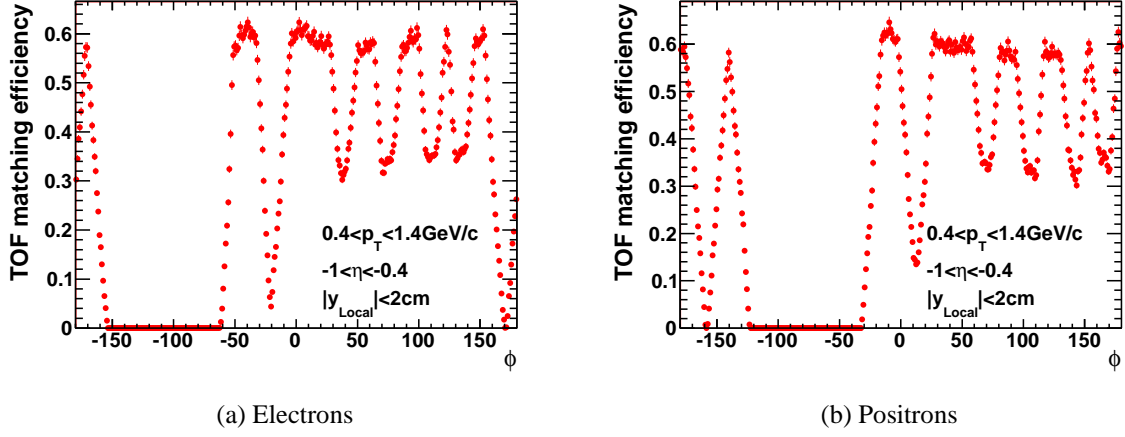
included in systematic uncertainties.
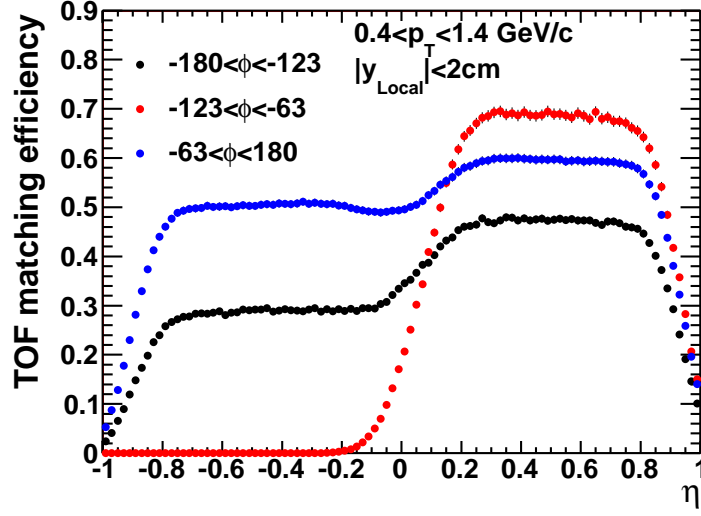
Figure 3.41: TOF matching efficiency for electrons, with the $|y_{Local}| \leq 2$ cm cut, as a function of η for $0.4 \leq p_T < 1.4$ GeV/c and three ϕ bins: -180°$\leq \phi <$ -123°(in black) , -123°$\leq \phi <$ -63°(in red) and -63°$\leq \phi \leq$ 180 °(in blue).

$1/\beta$ cut efficiency

The efficiency of the $|1/\beta - 1| \leq 0.03$ cut is calculated using an electron sample with a hight purity. Th pure electron sample is obtained by selecting tracks with -0.2 $< n\sigma_e <$ 2 and invariant mass of a pair of particles less than 15 MeV/c^2. The invariant mass cut selects photonic electrons, from photon conversion in the detector material and Dalitz decay of π^0 and η mesons, where almost no hadron background is presented.

The $1/\beta$ cut efficiency is defined as a ratio of a number of electrons in the TOF that pass the $1/\beta$ cut ($N^e_{TOF\&\beta Cut}$) to a number of electrons in the TOF (N^e_{TOF}):

$$\epsilon_\beta = \frac{N^e_{TOF\&\beta Cut}}{N^e_{TOF}} \tag{3.15}$$

Figure 3.42 show the $1/\beta$ cut efficiency as a function of momentum. The momentum dependent efficiency is calculated from the data, in small momentum intervals:

$$\epsilon_\beta(p) = \frac{\int_{0.97}^{1.03} f(1/\beta, p)}{\int_{0.90}^{1.10} f(1/\beta, p)}, \tag{3.16}$$

where $\int_{0.97}^{1.03} f(1/\beta, p)$ is a number of electrons in a range where $1/\beta$ cut is used and $\int_{0.90}^{1.10} f(1/\beta, p)$ is a number of all electrons, for a small momentum interval.
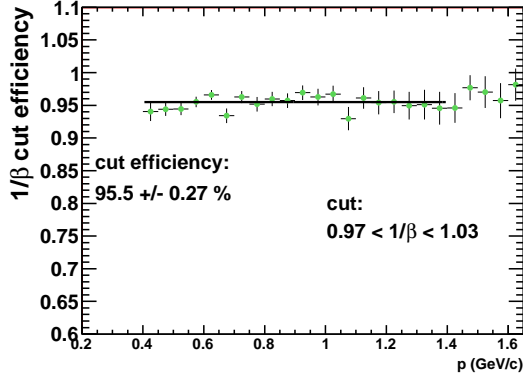
Figure 3.42: The $1/\beta$ cut efficiency as a function of momentum with a constant function fitted at $0.4 \leq p < 1.4$ GeV/c. The cut efficiency from the fit is $95.70 \pm 0.26\%$
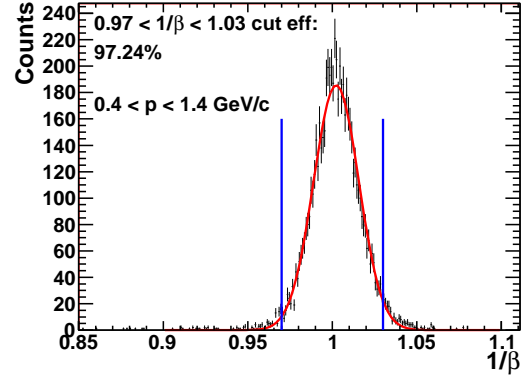
Figure 3.43: The $1/\beta$ distribution from the data in black for $0.4 \leq p < 1.4$ GeV/c with the Gaussian fit in red. The cut efficiency $1/\beta$ from the Gaussian fit is 97.3%. Vertical lines represent the cut range.

There is a small momentum dependence. Due to a limited statistics, small deviations from the linearity are most probably due to fluctuations. In order to avoid an influence of the fluctuations on the result, the $1/\beta$ cut efficiency is obtained by fitting a constant function in the momentum range $0.4 \leq p < 1.4$ GeV/c. The $|1/\beta - 1| \leq 0.03$ cut efficiency obtained in that way is:

$$\epsilon_\beta = 95.70 \pm 0.26\%. \tag{3.17}$$

This value is used as the $1/\beta$ cut efficiency in the total efficiency calculations.

The $1/\beta$ distribution in the whole momentum range where the $1/\beta$ cut is used ($0.4 \leq p < 1.4$ GeV/c) is shown in Fig. 3.43 with the Gaussian fit. Vertical lines represent the range of the cut. The $1/\beta$ cut efficiency calculated in the momentum range $0.4 \leq p < 1.4$ GeV/c from the Gaussian fit using formula 3.16 is: $\epsilon_\beta = 97.24\%$, the uncertainty is negligibly small. The difference between the efficiencies obtained using described two methods is included in systematic uncertainties.

3.4.3 J/ψ efficiencies

J/ψ efficiencies as a function of J/ψ p_T^{MC} and $cos\theta$ are calculated using the J/ψ embedding. $cos\theta$ is calculated as an angle between the positron MC momentum vector in the J/ψ rest frame and the J/ψ MC momentum vector in the laboratory frame.

Track quality, acceptance, BEMC cuts and HT trigger conditions are directly applied in the embedding analysis code. Matching to the BEMC is done in the same way as in the data analysis. A reconstructed in the TPC track is projected to the BEMC and a tower that the track projects to is considered.

TPC eID ($n\sigma_e$ cut) efficiency as a function of momentum, $\epsilon_{n\sigma_e}$, and the TOF efficiency as a function of η, ϵ_{TOF}, are applied in the embedding analysis as a weight - w_{eID}^e. These efficiencies are obtained from the data.

$$w_{eID}^e(p, \eta) = \epsilon_{n\sigma_e}(p) \times \epsilon_{TOF}(\eta) \tag{3.18}$$

The ϵ_{TOF} includes the TOF matching efficiency, $\epsilon_{TOFmatching}$, and the efficiency of the $1/\beta$ cut, ϵ_β:

$$\epsilon_{TOF}(\eta) = \epsilon_{TOFmatching}(\eta) \times \epsilon_\beta \tag{3.19}$$

The J/ψ eID weight ($w_{eID}^{J/\psi}$) is a product of the weights for electrons from the J/ψ decay:

$$w_{eID}^{J/\psi} = w_{eID}^{e^+} \times w_{eID}^{e^-} \tag{3.20}$$

The total J/ψ weight ($w^{J/\psi}$) applied on the final J/ψ distributions in the embedding analysis is a product of the J/ψ eID weight ($w_{eID}^{J/\psi}$) and the input J/ψ weight ($w_{input}^{J/\psi}$):

$$w^{J/\psi} = w_{eID}^{J/\psi} \times w_{input}^{J/\psi} \tag{3.21}$$

Weights for the input p_T and rapidity distributions, $w_{input}^{J/\psi}$, are discussed in Sec. 3.4.1.1.

In order to match conditions from the data analysis, following cuts are applied, in addition to the track quality and the electron identifications cuts, in the embedding analysis: $|V_z| < 65$ cm $|y^{J/\psi}| < 1$.

Tracking and acceptance efficiency

Figures 3.44 and 3.45 show the tracking efficiency (that includes a probability that MC track is reconstructed in the TPC) and acceptance as a function of $cos\theta$ and J/ψ p_T^{MC}, respectively. The efficiency is calculated as a ratio of a number of reconstructed J/ψ ($N_{RC}^{J/\psi}$) to a number of simulated J/ψ ($N_{MC}^{J/\psi}$):

$$\epsilon_{RC}^{J/\psi} = \frac{N_{RC}^{J/\psi}}{N_{MC}^{J/\psi}} \tag{3.22}$$

Both electron and positron from the J/ψ decay have to passed the track quality and acceptance cuts. Applied track quality and acceptance cuts are listed in table 3.2, cuts 4-10.
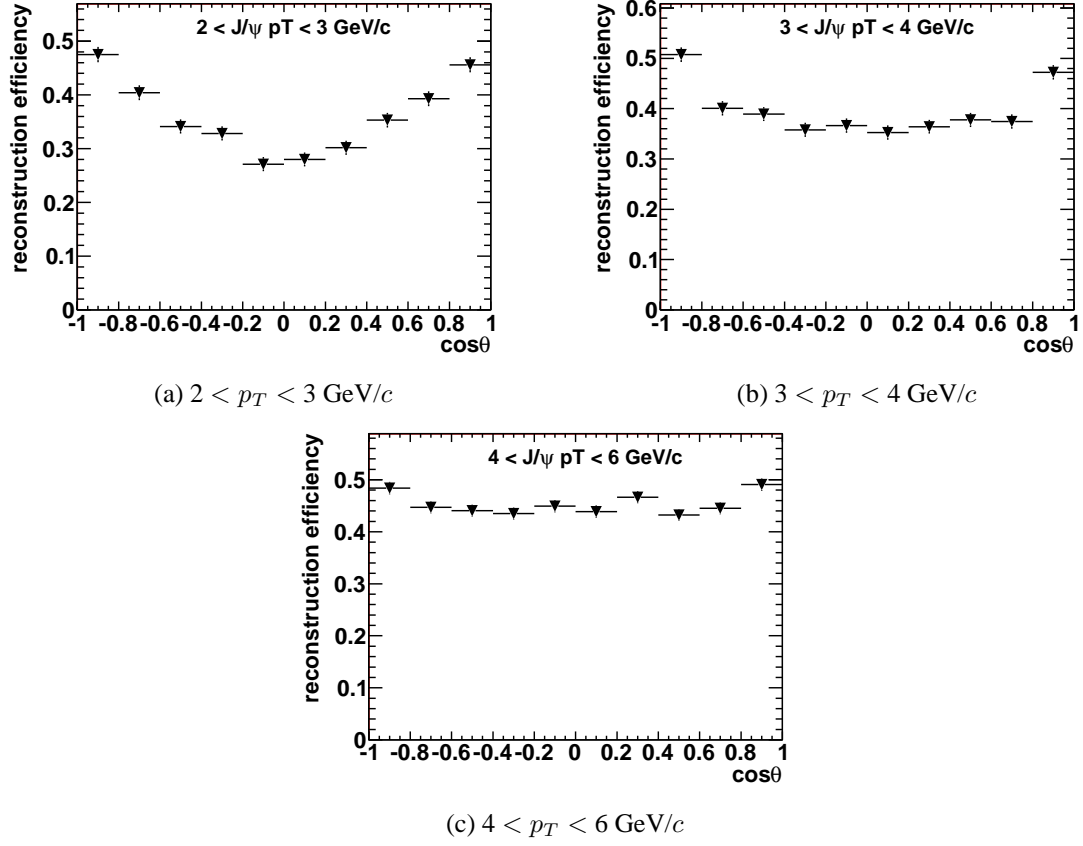
(a) $2 < p_T < 3$ GeV/c

(b) $3 < p_T < 4$ GeV/c

(c) $4 < p_T < 6$ GeV/c

Figure 3.44: J/ψ tracking and acceptance efficiency as a function of $cos\theta$ in p_T bins.

Figure 3.45: J/ψ tracking and acceptance efficiency as a function of p_T^{MC}.

85

(a) $2 < p_T < 3$ GeV/c

(b) $3 < p_T < 4$ GeV/c

(c) $4 < p_T < 6$ GeV/c
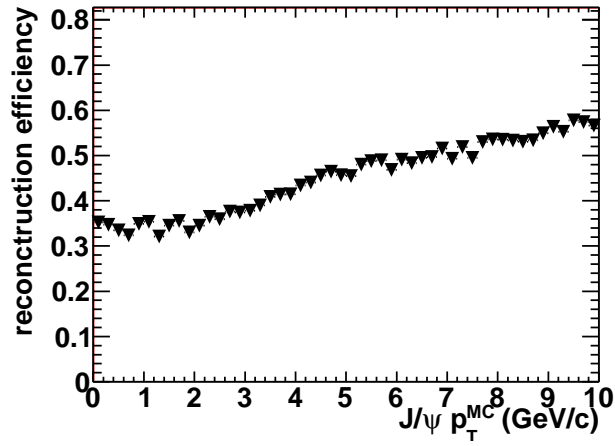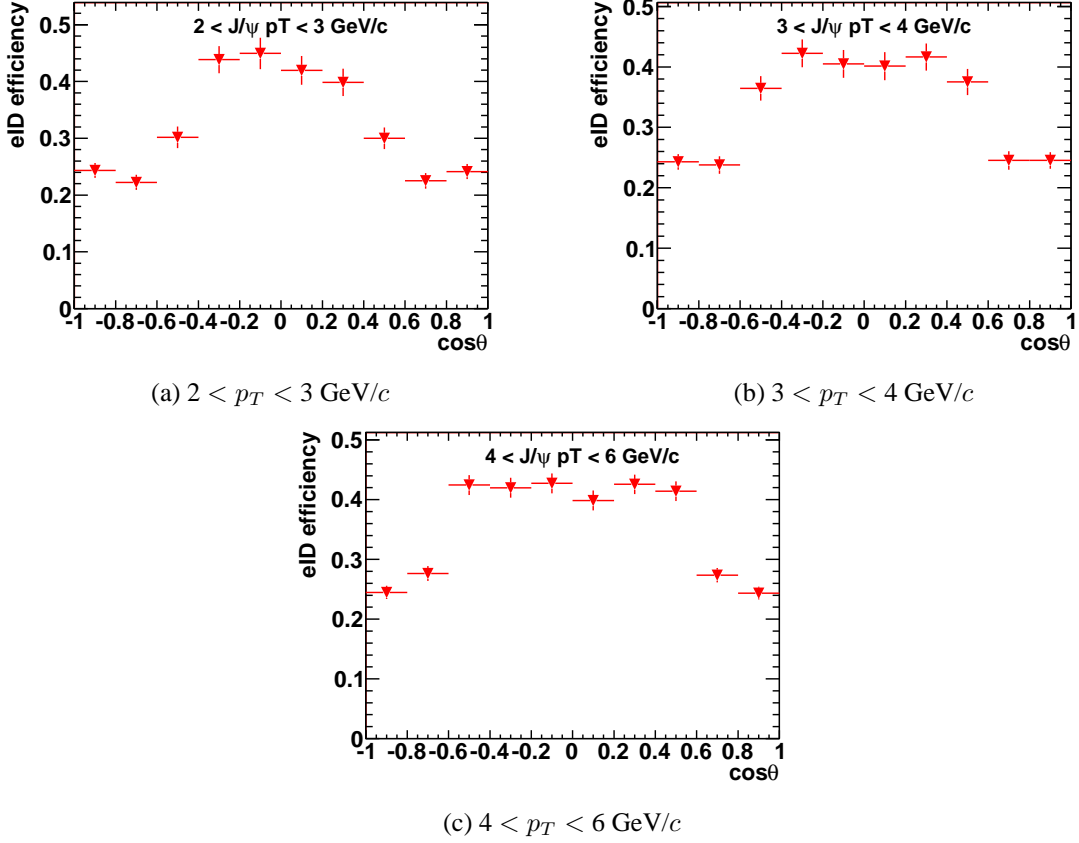
Figure 3.46: J/ψ di-electron identification efficiency as a function of $cos\theta$ in p_T bins.

Electron identification efficiency

Figures 3.46 and 3.47 show the electron identification efficiency as a function of $cos\theta$ and J/ψ p_T^{MC}, respectively. Applied eID cuts on electrons from the J/ψ decay are listed in table 3.2, cuts 12-16. The $n\sigma_e$ cut efficiency and the TOF efficiencies are applied as weights. The electron identification efficiency is determined by a number of J/ψ after the eID cuts ($N_{eID}^{J/\psi}$) to a number of reconstructed J/ψ ($N_{RC}^{J/\psi}$), that pass track quality of acceptance cuts:

$$\epsilon_{eID}^{J/\psi} = \frac{N_{eID}^{J/\psi}}{N_{RC}^{J/\psi}} \tag{3.23}$$

Both electron and positron from the J/ψ decay have to passed the track quality and acceptance cuts.

HT trigger efficiency

The HT trigger efficiency is calculated by applying the HT trigger condition to the embedding analysis: $dsmAdc$ in a BEMC tower has to be within $11 < dsmAdc \leq 18$. In addition, the electron that fired the trigger has to have $p_T \geq 2.5$ GeV/c. The HT trigger efficiency is
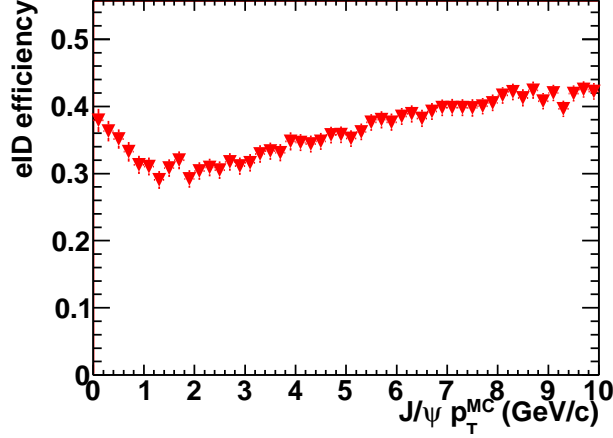
Figure 3.47: J/ψ di-electron identification efficiency as a function of p_T^{MC}.

calculated as a number of J/ψ that satisfy the mentioned HT trigger requirements ($N_{HT}^{J/\psi}$) to a number of J/ψ that pass the eID cuts ($N_{eID}^{J/\psi}$):

$$\epsilon_{HT}^{J/\psi} = \frac{N_{HT}^{J/\psi}}{N_{eID}^{J/\psi}} \tag{3.24}$$

It is required that at least one of electrons from the J/ψ decay fired the HT trigger. Figures 3.48 and 3.49 show the Hight Tower trigger efficiency as a function of $cos\theta$ and J/ψ p_T^{MC}, respectively.

3.4.4 Total J/ψ efficiency

The total J/ψ efficiency, to be applied to uncorrected $cos\theta$ distributions, is obtained from the J/ψ embedding by applying cuts, or corresponding weights, that are used in the data analysis. The total efficiency is determined as a number of J/ψ that pass all cuts ($N_{final}^{J/\psi}$) to a number of embedded Monte Carlo J/ψ ($N_{MC}^{J/\psi}$).

$$\epsilon_{total}^{J/\psi} = \frac{N_{final}^{J/\psi}}{N_{MC}^{J/\psi}} \tag{3.25}$$

Distributions of the total J/ψ efficiency as a function of $cos\theta$, in three analysed p_T bins, are shown in Fig. 3.50. The total J/ψ efficiency as a function of J/ψ p_T^{MC} is shown in Fig. 3.51.

The total correction includes the detector acceptance and tracking efficiency, dielectron identification efficiency and the trigger efficiency. The most critical factor is the trigger efficiency. Due to the decay kinematics, the HT trigger requirements cause significant loss in number of observed J/ψ at lower p_T, and the efficiency decreases with decreasing $|cos\theta|$. It is well visible in Fig. 3.50a, where we lose all entries at $cos\theta \sim 0$. With increasing J/ψ p_T the

(a) $2 < p_T < 3$ GeV/c

(b) $3 < p_T < 4$ GeV/c

(c) $4 < p_T < 6$ GeV/c
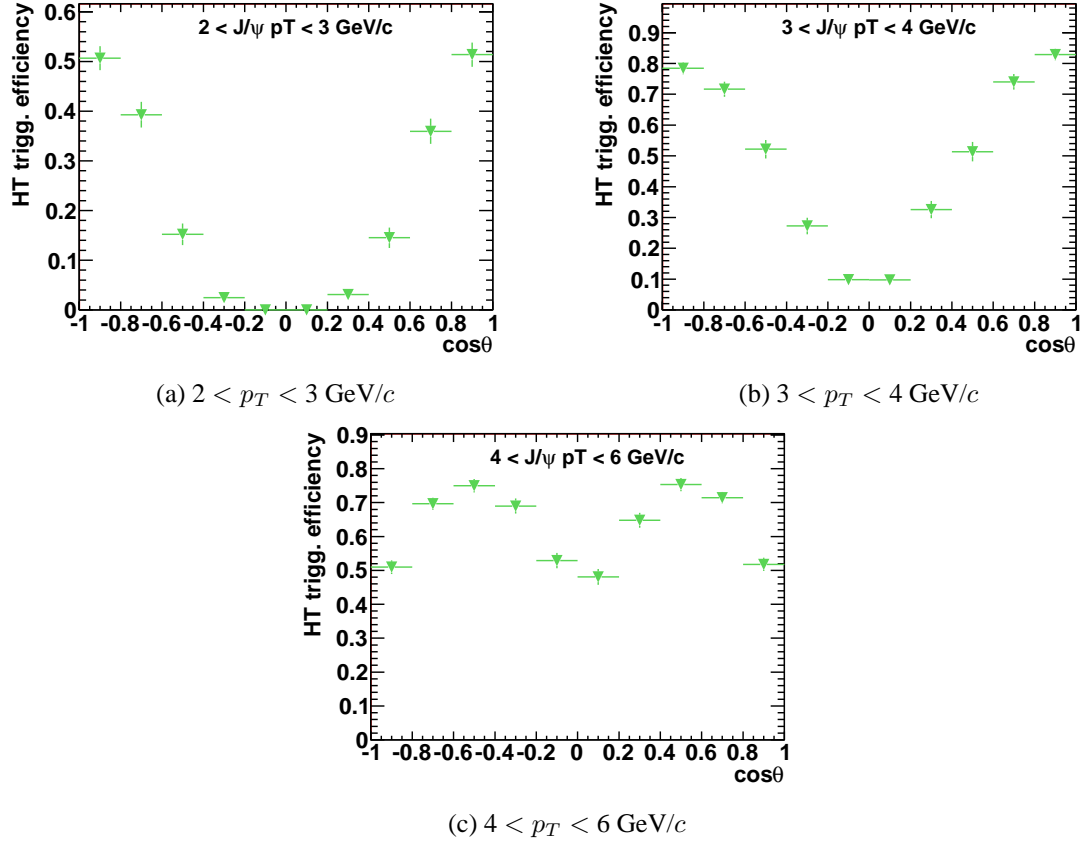
Figure 3.48: Hight Tower trigger efficiency as a function of $cos\theta$ in p_T bins.

Figure 3.49: Hight Tower trigger efficiency as a function of p_T^{MC}.

88
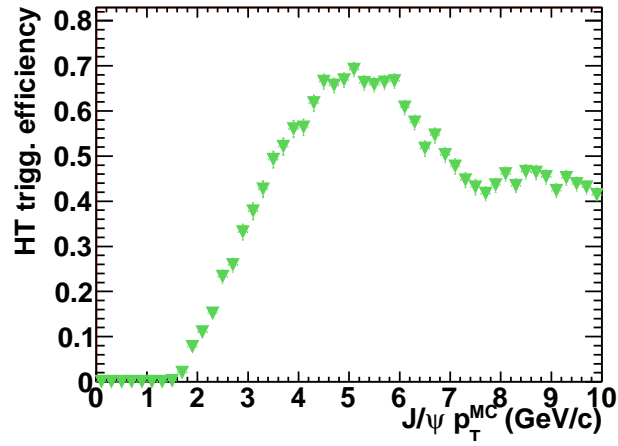
trigger efficiency increases, but because the trigger has also the upper threshold (transverse energy deposited in the BEMC tower: $E_T \leq 4.3$ GeV) a drop of the total efficiency at $|cos\theta| \sim 1$ is seen, see Fig. 3.50c.

(a) $2 < p_T < 3$ GeV/c

(b) $3 < p_T < 4$ GeV/c

(c) $4 < p_T < 6$ GeV/c
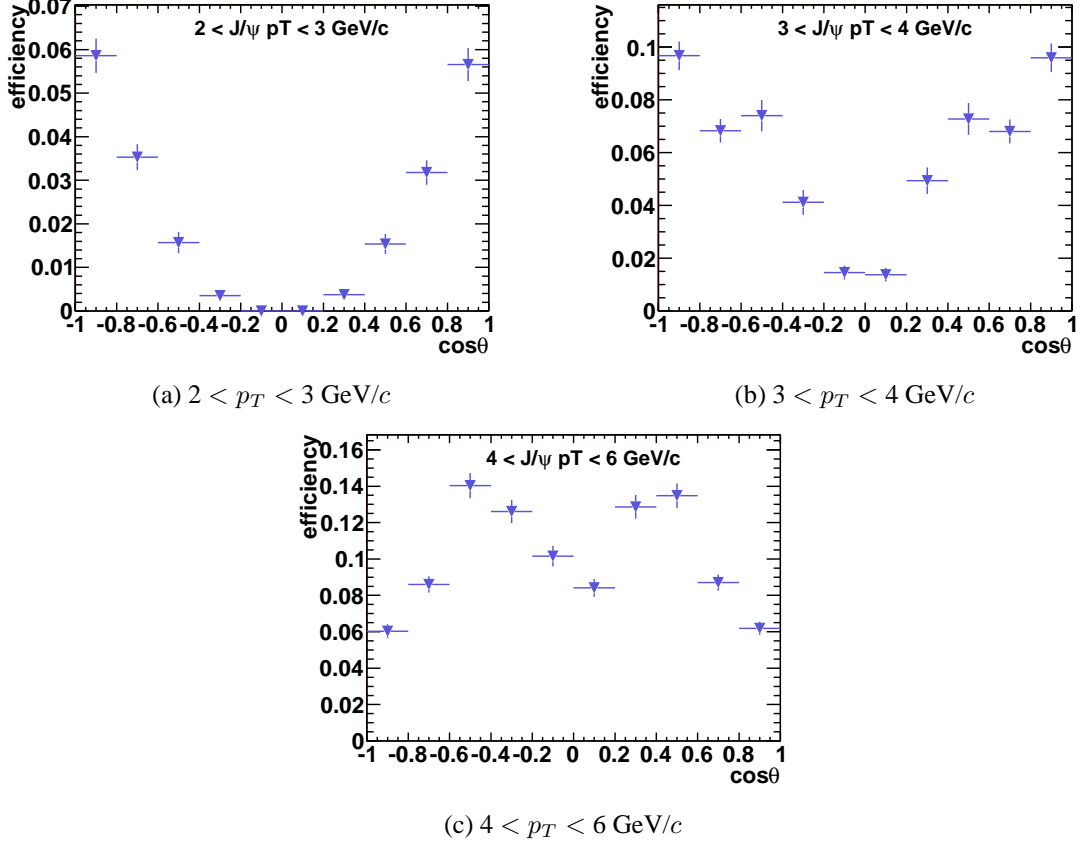
Figure 3.50: Total J/ψ efficiency as a function of $cos\theta$ in p_T bins.
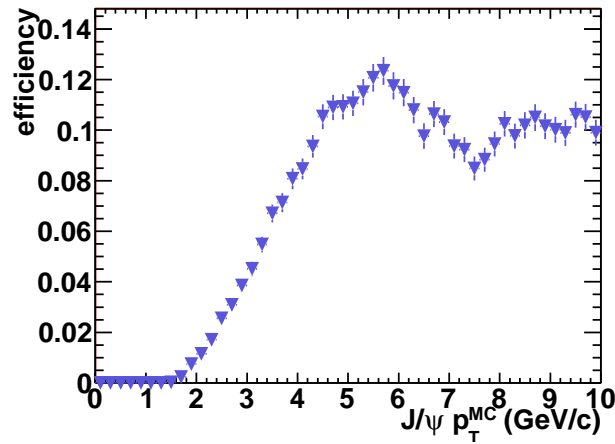
Figure 3.51: Total J/ψ efficiency as a function of p_T^{MC}.

Chapter 4

Polarization results

4.1 Corrected $cos\theta$

The total J/ψ efficiencies as a function of $cos\theta$ are used to correct the raw $cos\theta$ distributions from the data, in the three analysed p_T bins. Figure 4.1 shows the uncorrected $cos\theta$ distributions in each p_T bin (left plots) with corresponding distributions of the total efficiencies (right plots). In total efficiency plots statistical and systematic uncertainties are shown. Blue squares represent the systematic uncertainties. The systematic uncertainties include all sources of the efficiency uncertainties which are discussed in Sec. 5 and are summarised in Tab. 5.12 (contributions 2 - 12). The raw $cos\theta$ distributions are corrected with the total efficiencies, without taking into account the errors on the efficiency. The statistical errors of the efficiencies are included in the polarization systematic uncertainties (Sec. 5).

Corrected $cos\theta$ distributions are fitted with the function:

$$norm(1 + \lambda_\theta cos^2\theta) \tag{4.1}$$

where $norm$ is a normalization factor and λ_θ is the polarization parameter. No constraints on the fit parameters are applied.

Figure 4.2 shows corrected $cos\theta$ distributions with the function 4.1 fitted. Shown errors represent statistical uncertainties from the data. The solid line represents the most likely fit. The dashed band around this line is 1σ uncertainty on the fit. It takes into account uncertainties on both fit parameters ($norm$ and λ_θ) and correlations between them.
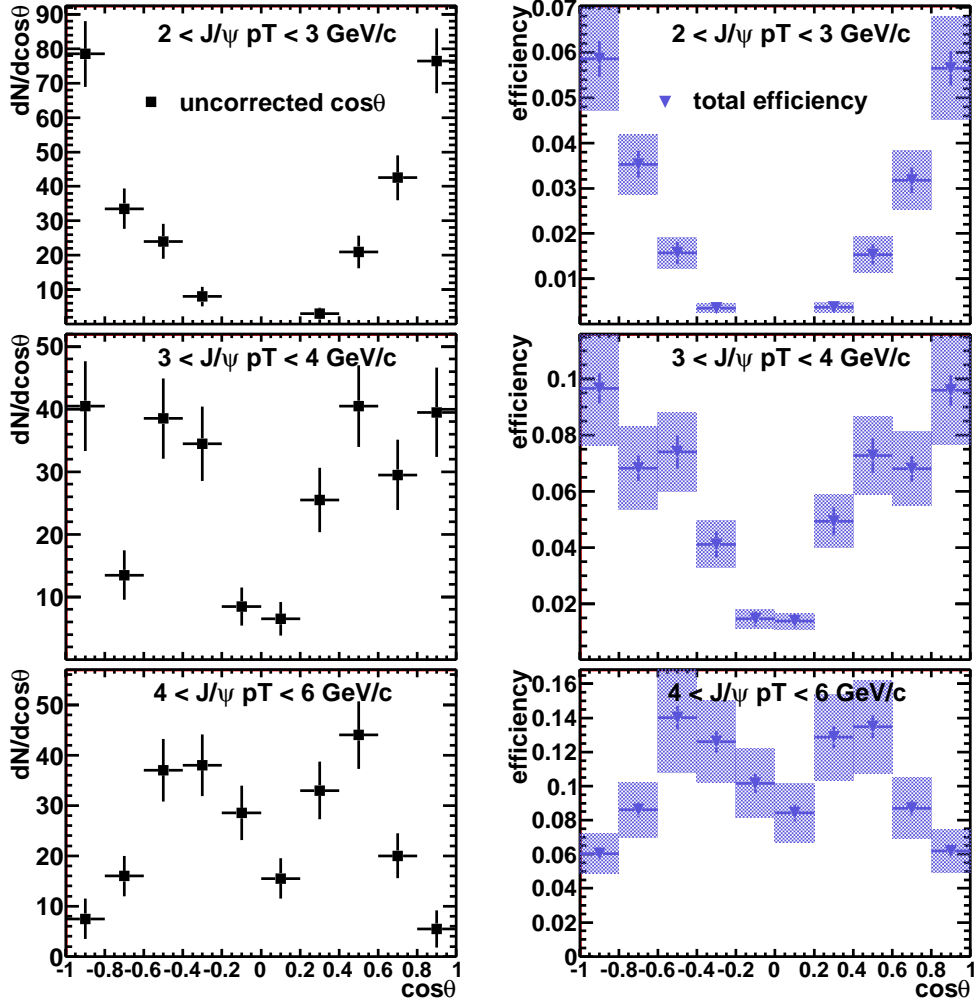
Figure 4.1: Left plots show an uncorrected $cos\theta$ distributions after the combinatorial background subtraction. Right plots show total corrections.

(a) $2 < p_T < 3$ GeV/c

(b) $3 < p_T < 4$ GeV/c

(c) $4 < p_T < 6$ GeV/c
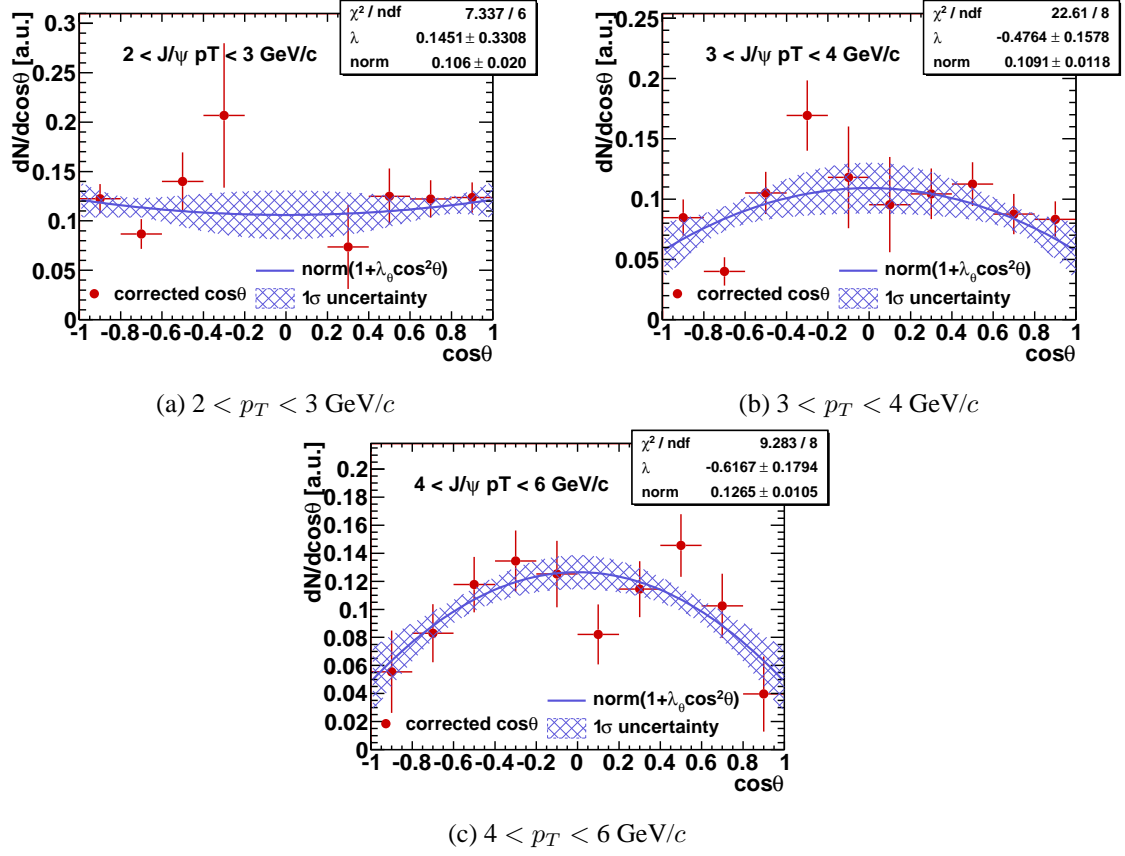
Figure 4.2: Corrected $cos\theta$ distributions fitted with a function: $norm(1 + \lambda_\theta cos^2\theta)$ in each analyzed p_T bin, shown errors are statistical. Solid blue lines represent the most likely fits and hatched blue bands represent 1σ uncertainty on the fits.

Obtained values of the polarization parameter for each J/ψ p_T bin are:

- $2 < p_T < 3$ GeV/c

    – $\lambda_\theta = 0.15 \pm 0.33$ (stat.)

- $3 < p_T < 4$ GeV/c

    – $\lambda_\theta = $ -0.48 $\pm$ 0.16 (stat.)

- $4 < p_T < 6$ GeV/c

    – $\lambda_\theta = $ -0.62 $\pm$ 0.18 (stat.)

We observe that the polarization parameter λ_θ decrease with increasing p_T. The trend is towards the longitudinal J/ψ polarization in the helicity frame as p_T increases.

4.2 The polarization parameter

Figure 4.3 shows the p_T dependent J/ψ polarization parameter λ_θ. Additionally, the PHENIX mid-rapidity ($|y| < 0.35$) results (black filled circles [32]) are shown. The results are for the inclusive J/ψ production, i.e. the sample includes directly produced J/ψ as well as the J/ψ from the feed-down from the higher excited states, χ_C and ψ' (33 ± 5 % [16]) and from the B meson feed-down (10-25% for $4 < p_T < 12$ GeV/c [18]). The result is also compared with two model predictions for the λ_θ at mid-rapidity: NLO^+ Color Singlet Model (CSM) [27] and NRQCD calculations with color octet contributions (COM) [47]. The prediction of the COM for direct J/ψ production, gray shaded area, goes towards the transverse J/ψ polarization as p_T increases. This trend is different from what is seen in the RHIC data. Green dashed lines represent a range of λ_θ for the direct J/ψ production from the $NLO^+ CSM$ prediction and an extrapolation of λ_θ for the prompt J/ψ production (with the feed-down from the excited states but the B feed-down is excluded) is shown as the hatched blue band [27]. This model predicts a weak λ_θ p_T dependence, and within the experimental and theoretical uncertainties the RHIC result is consistent with the $NLO^+ CSM$ model prediction.
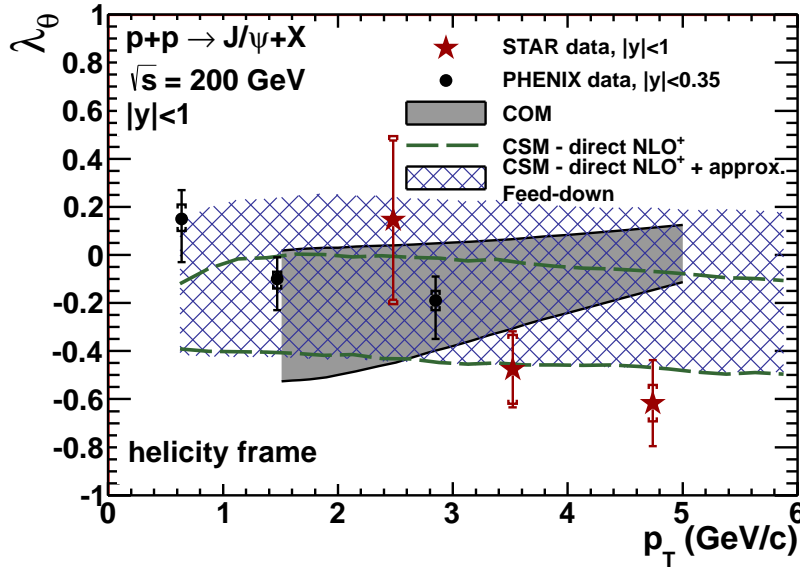
Figure 4.3: The polarization parameter λ_θ as a function of J/ψ p_T (red stars) for $|y| < 1$ in p+p collisions at $\sqrt{s} = 200$ GeV. The result is compared with two model predictions: NLO^+ Color Singlet Model (CSM) (green dashed lines represent a range of λ_θ for the direct J/ψ and hatched blue band is an extrapolation of λ_θ for the prompt J/ψ) [27] and NRQCD calculations with color octet contributions (COM) [47] (gray shaded area). For a comparison the PHENIX result is shown as black filled circles [32].

In order to obtain p_T positions of the points, the Kaplan function [79] from Eq. 4.2 is fitted to the corrected p_T spectrum.

$$f(p_T) = A(1 + (\frac{p_T}{B})^2)^{-6} \tag{4.2}$$

The raw p_T distribution is corrected with the total efficiency, taking into account errors on the total efficiency. Figure 4.4 shows the corrected p_T spectrum obtained from the data in blue and the dashed blue line represents the fitted function. Red triangles represent data points in three p_T bins that are used in the polarization analysis: $2 < p_T < 3$ GeV/c, $3 < p_T < 4$ GeV/c and $4 < p_T < 6$ GeV/c. In Fig. 4.4a the red points are placed in the center of a bin. In order to obtain positions of the points for the λ_θ distribution, the red points are shifted so that they lie on the fitted function, as it is show in Fig. 4.4b. Obtained values of p_T position are: 2.48 GeV/c, 3.52 GeV/c and 4.74 GeV/c for $2 < p_T < 3$ GeV/c, $3 < p_T < 4$ GeV/c and $4 < p_T < 6$ GeV/c, respectively.

(a) Points in the center of bins.

(b) Shifted points positions.
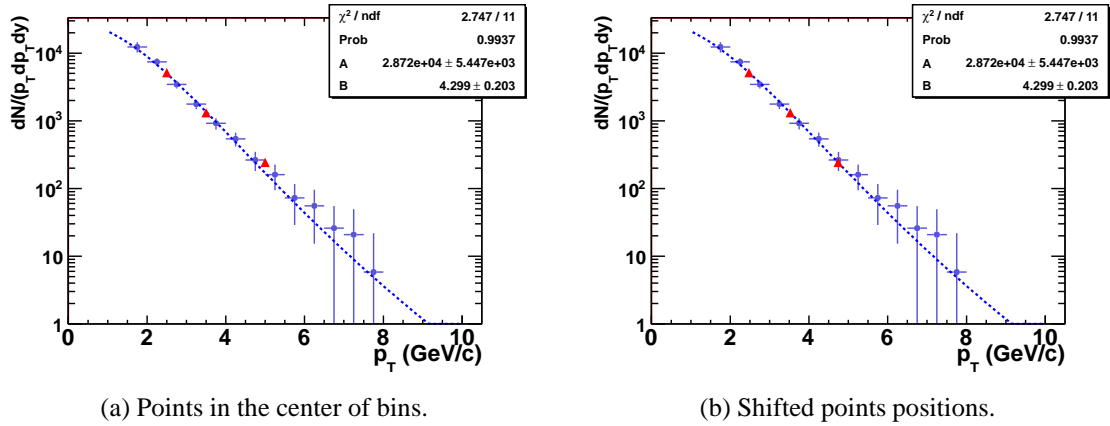
Figure 4.4: Corrected J/ψ p_T spectrum in blue with the function from Eq. 4.2 fitted (dashed blue line), red triangles are data points for the three p_T bins used in the polarization analysis. In Fig. (a) the red points are in the center of a bins and in Fig. (b) x positions of the points are shifted so that they lie on the fitted function.

In order to check a trend in the data, constant and linear functions are fitted to the λ_θ distribution shown in Fig. 4.3. The distribution with the fitted functions is shown in Fig. 4.5. Errors contain statistical and systematic contributions. Fits are done taking the PHENIX data points at lower p_T and at $p_T > 3$ GeV/c the STAR data points are used. The points used in the fit are marked in magenta. It is seen that the RHIC result goes towards the longitudinal J/ψ polarization with increasing p_T. The constant fit has a poor χ^2/ndf of 10.32/4. The linear fit is much better, it has a negative slope parameter of -0.17 $\pm$ 0.05 with $\chi^2/ndf = 0.82/3$.

94
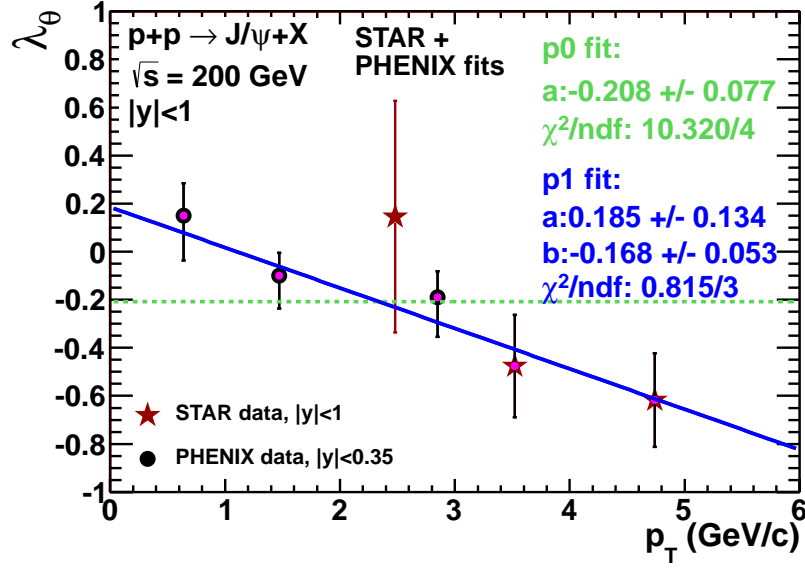
Figure 4.5: The polarization parameter λ_θ as a function of J/ψ p_T. Red stars are the STAR data points and black full circles are the PHENIX data points. The green dashed line represents a constant fit and the blue solid line is a linear fit to the magenta points.

Table 4.1 summarises the λ_θ values with their statistical and systematic errors, and p_T positions ($< p_T >$). Methods of systematic uncertainties estimation are discussed in the Chapter 5.

p_T range (GeV/c)	$< p_T >$ (GeV/c)	λ_θ	stat. error	sys. error
$2 < p_T < 3$	2.48	0.145	$\pm$ 0.331	$\pm$ 0.350
$3 < p_T < 4$	3.52	-0.476	$\pm$ 0.158	$\pm$ 0.143
$4 < p_T < 6$	4.74	-0.617	$\pm$ 0.179	$\pm$ 0.076

Table 4.1: The polarization parameter.

Chapter 5

Systematic uncertainties

5.1 $cos\,\theta$ from the MC simulation

$cos\theta$ distributions for the final result are obtained by summing up number of J/ψ's from the data, in each analysed p_T and $cos\theta$ bin. Another method of determining $cos\theta$ distributions is by counting number of J/ψ's using the J/ψ signal from the MC simulation (the lineshape). Since the p_T resolution in the simulation was found to be too small, it was additionally smeared with Gaussian which parameters are: $\mu = 0$ and $\sigma_A = 0.71$ p_T, see Sec. 3.4.1.3 for details. Figure 5.1 shows an example of the J/ψ signal with the additional momentum smearing for two $cos\theta$ and p_T bins.

In order to estimate a systematic uncertainty on the J/ψ polarization, $cos\theta$ distributions are obtained by counting number of J/ψ's using the embedding. The best value of the smearing parameter was found to be 0.71 ± 0.05 % p_T. And polarization parameters λ_θ are extracted using the J/ψ lineshape with additional p_T smearing in a range 0.66% - 0.76% p_T, which takes into account the uncertainty on the smearing parameter. The systematic uncertainty is an average of differences between the λ_θ value obtained from the data and λ_θ values obtained using the embedding, with p_T smearing (0.66, 0.67, ..., 0.76)% p_T. Figure 5.2 shows $cos\theta$ distributions obtained using the J/ψ signal from the embedding with the additional p_T smearing of 0.71% p_T.

The systematic uncertainty on the J/ψ polarization is shown in a table 5.1.
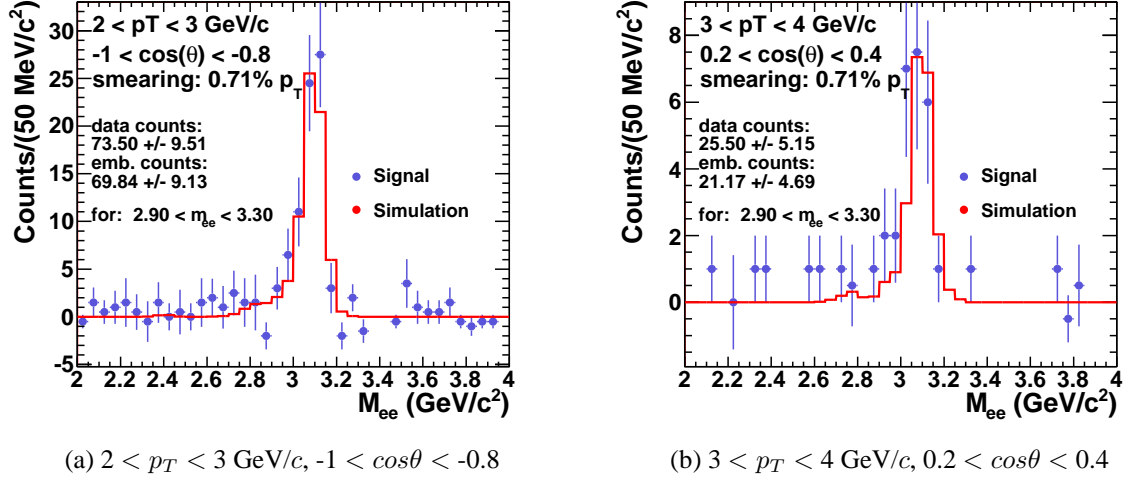
(a) $2 < p_T < 3$ GeV/c, $-1 < cos\theta < -0.8$

(b) $3 < p_T < 4$ GeV/c, $0.2 < cos\theta < 0.4$

Figure 5.1: J/ψ signal after the combinatorial background subtraction (blue filled circles), the red line is J/ψ signal from the embedding with the additional p_T smearing of 0.71% p_T.

(a) $2 < p_T < 3$ GeV/c

(b) $3 < p_T < 4$ GeV/c

(c) $4 < p_T < 6$ GeV/c

Figure 5.2: Corrected $cos\theta$ distributions obtained from the MC simulation, with the additional p_T smearing of 0.71% p_T, fitted with a function: $norm(1 + \lambda_\theta cos^2\theta)$ in each analyzed p_T bin, shown errors are statistical. Solid blue lines represent the most likely fits and hatched blue bands represent 1σ uncertainty on fits.

97

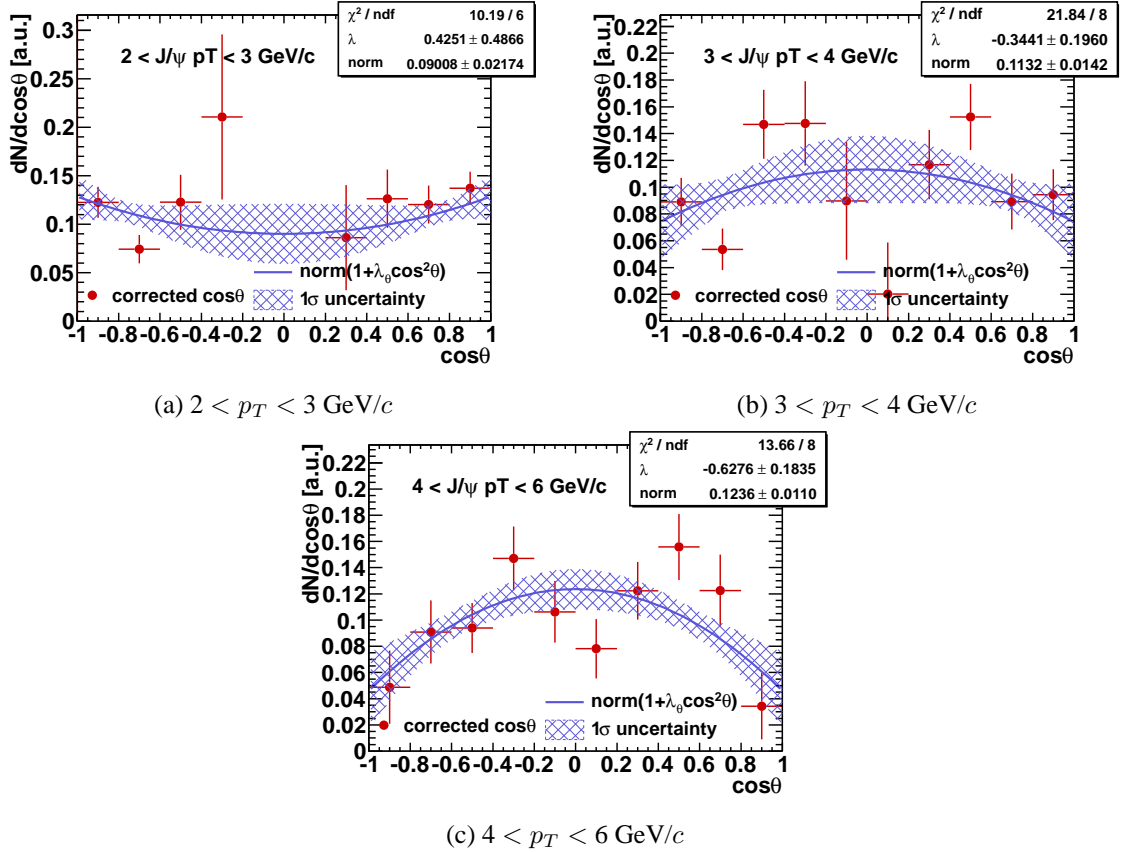| Id	Systematic uncertainty source	Systematic uncertainty on λ_θ		
		$2 < p_T < 3$ GeV/c	$3 < p_T < 4$ GeV/c	$4 < p_T < 6$ GeV/c
1	polarization from the simulated lineshape	0.270	0.135	0.003

Table 5.1: Systematic uncertainty from the polarization obtained from the simulated J/ψ line-shape.

5.2 Weighting of input J/ψ p_T and rapidity distributions in the simulation

Since J/ψ input p_T and rapidity distributions used in the embedding are flat, they have to be weighted according to experimental shapes. The p_T and y weighting is described in section 3.4.1.1.

A systematic uncertainty from the weighting of the p_T distribution is estimated using three methods. The Kaplan function which is used for the p_T weighting is $f(p_T) = A(1 + (\frac{p_T}{B})^2)^{-6}$, with parameters of $A = 4.23 \pm 4.23$ and $B = 4.10 \pm 0.13$, obtained from the fit in a p_T range of 0-10 GeV/c.

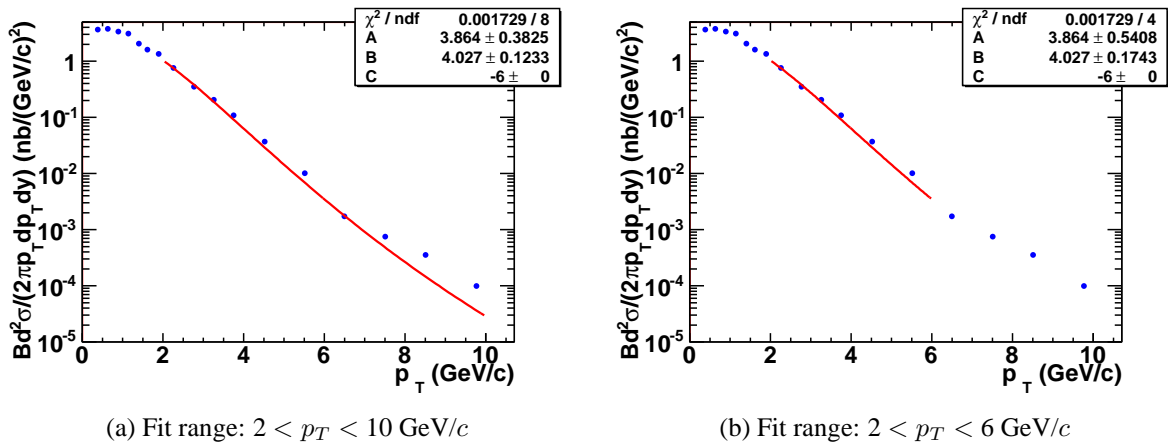(a) Fit range: $2 < p_T < 10$ GeV/c (b) Fit range: $2 < p_T < 6$ GeV/c

Figure 5.3: J/ψ p_T spectrum with $f(p_T) = A(1 + (\frac{p_T}{B})^2)^{-6}$ function fitted in p_T ranges: (a) from 2 to 10 GeV/c and (b) from 2 to 6 GeV/c.

First, values of the A and B parameters are varied by their 1σ uncertainties, and the polar-

ization parameter is recalculated. In next two methods, the A and B parameters are extracted by fitting the Kaplan function in two different p_T ranges: from 2 to 10 GeV/c and from 2 to 6 GeV/c (the J/ψ p_T range used for this analysis), as it is shown in Fig. 5.3. Also, the parameters' values are varied by their 1σ uncertainties, and λ_θ is extracted in each case.

The final systematic uncertainty from the p_T weighting is an average of systematic errors from described three methods.

In the analysis, the rapidity distribution is fitted with the Gaussian function in order to obtain the J/ψ y weight. But at mid-rapidity many functions describe the observed rapidity distribution well. To estimate a systematic uncertainty from the weighting of the rapidity distribution, the y distribution is assumed to be uniform at mid-rapidity ($|y| < 1$).

Systematic uncertainties on the J/ψ polarization from weighting the input p_T and rapidity distributions in the simulation are shown in a table 5.2.

Id	Systematic uncertainty source	Systematic uncertainty on λ_θ		
		$2 < p_T < 3$ GeV/c	$3 < p_T < 4$ GeV/c	$4 < p_T < 6$ GeV/c
2	weighting of the input J/ψ p_T shape	0.018	0.007	0.019
3	weighting of the input J/ψ y shape	0.043	0.002	0.014

Table 5.2: Systematic uncertainties from the weighting of input J/ψ p_T distributions in the simulation.

5.3 Input J/ψ polarization in the simulation

In the embedding, simulated J/ψ's are unpolarized - input $cos\theta$ is flat. The shape of the input $cos\theta$ influences the acceptance and so the total J/ψ efficiency. In order to estimate the systematic uncertainty, we consider two extreme cases. Fully transverse ($\lambda_\theta = 1$) and fully longitudinal ($\lambda_\theta = -1$) input J/ψ polarization. Figure 5.4a shows the input $cos\theta$ distribution for the transverse case and Fig. 5.4b is for the longitudinal polarization.

The systematic uncertainty on the J/ψ polarization is estimated as an average of the uncer-
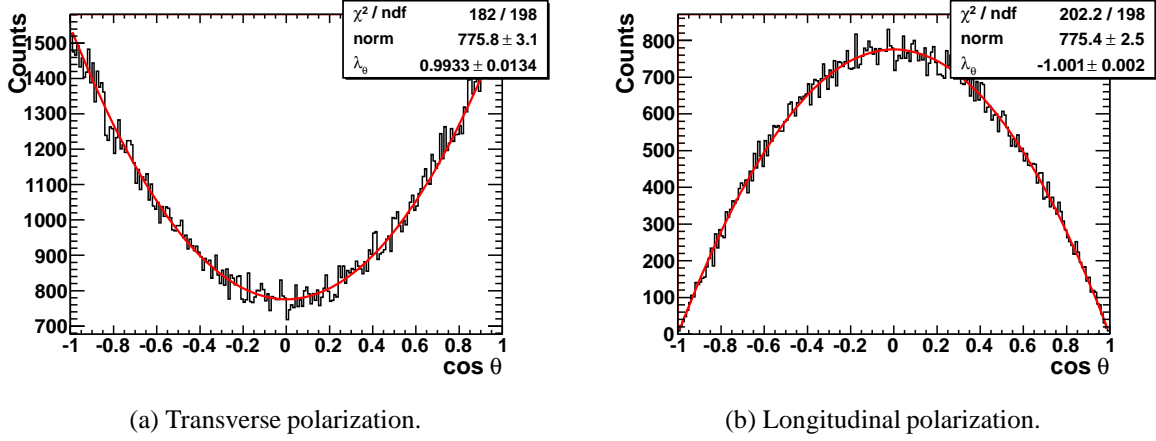
(a) Transverse polarization.	(b) Longitudinal polarization.

Figure 5.4: Input $cos\theta$ distribution from the simulation for fully transversely polarized J/ψ, Fig. 5.4a and fully longitudinally polarized J/ψ, Fig.5.4b.

tainties obtained for the described two extreme cases of the input J/ψ polarization, and is shown in a table 5.3.

Id	Systematic uncertainty source	Systematic uncertainty on λ_θ		
		$2 < p_T < 3$ GeV/c	$3 < p_T < 4$ GeV/c	$4 < p_T < 6$ GeV/c
4	input J/ψ polarization	0.184	0.018	0.013

Table 5.3: Systematic uncertainty from the input J/ψ polarization in the simulation.

5.4 Simulation uncertainties

In the main analysis, errors shown on the corrected $cos\theta$ distributions are statistical errors from the data. When correcting $cos\theta$ distributions, it is assumed that there is no statistical uncertainty from the simulation.

But the statistics in the embedding is limited, so the total efficiency has a statistical uncertainty, which may influence the λ_θ fit. The influence of statistical uncertainties of the efficiency on the λ_θ is included in the polarization systematic uncertainty. It is done by propagating statistical uncertainties of the total efficiency to uncertainties of the corrected $cos\theta$ distributions, while dividing raw $cos\theta$ distributions by the efficiency distributions. Then, the $norm(1 + \lambda_\theta cos^2\theta)$ function is fitted to the corrected distributions in order to extract the polarization parameter.
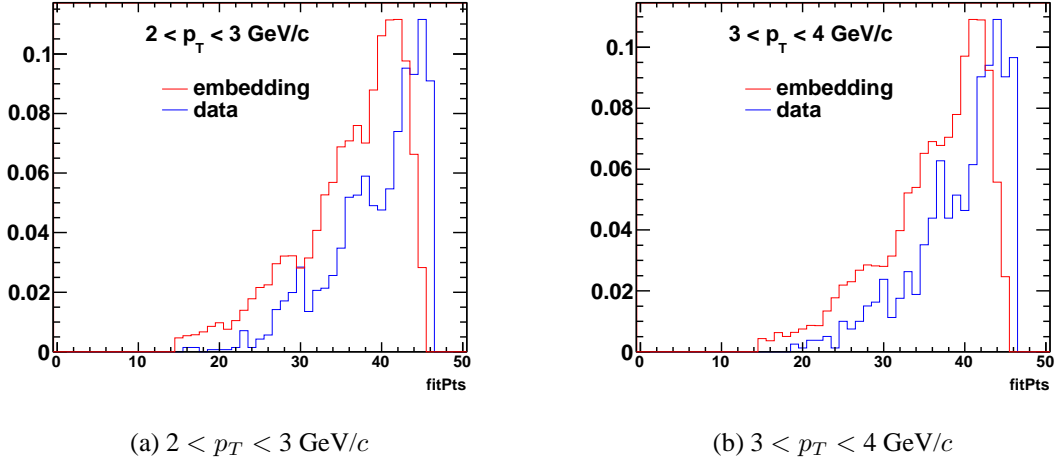
(a) $2 < p_T < 3$ GeV/c (b) $3 < p_T < 4$ GeV/c

Figure 5.5: Electrons $nFitPts$ distributions from the embedding in red and the data in blue. Figure (a) is for $2 < p_T < 3$ GeV/c and Fig. (b) is for $3 < p_T < 4$ GeV/c.

The J/ψ polarization systematic uncertainty is shown in a table 5.4.

Id	Systematic uncertainty source	Systematic uncertainty on λ_θ		
		$2 < p_T < 3$ GeV/c	$3 < p_T < 4$ GeV/c	$4 < p_T < 6$ GeV/c
5	errors from the simulation	0.077	0.028	0.004

Table 5.4: Systematic uncertainty from the simulation errors.

5.5 Tracking efficiency

To the tracking efficiency contribute efficiencies of $flag$, $nFitPts$, $nFitPts/nFitPtsMax$ and DCA cuts. The tracking efficiency is calculated from the simulation and it relies mostly on a good simulation of $nFitPts$ and DCA variables. Figure 5.5 shows the $nFitPts$ distribution and Fig. 5.6 shows the DCA distribution, for two p_T bins for the embedding in red and the data in blue. The distributions were obtained from a pure electron sample obtained by selecting photonic electrons with following cuts: -0.2 $< n\sigma_e < 2$ and invariant mass of a pair less than 15 MeV/c^2.

The simulated DCA agrees with the data, but there is some discrepancy between the data and the embedding in $nFitPts$ distributions. The embedding $nFitPts$ distribution seems to be
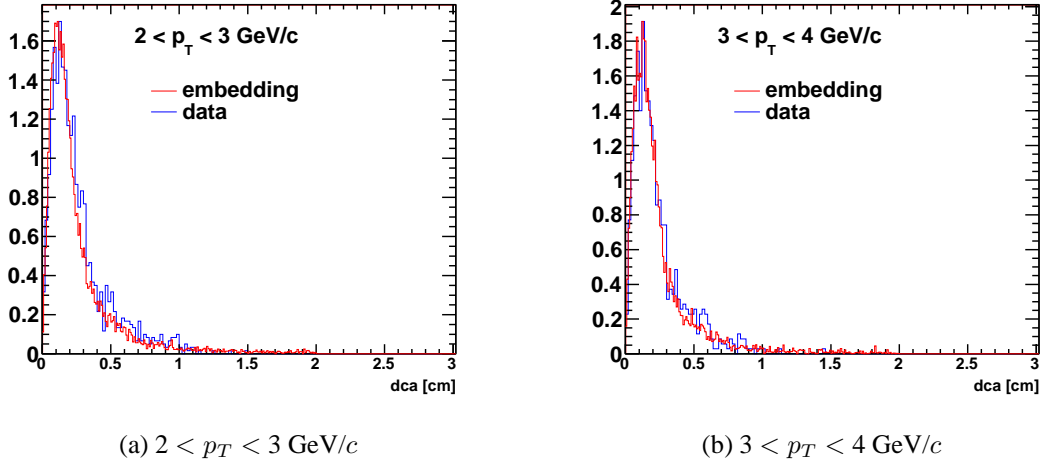
(a) $2 < p_T < 3$ GeV/c (b) $3 < p_T < 4$ GeV/c

Figure 5.6: Electrons DCA distributions from the embedding in red and the data in blue. Figure (a) is for $2 < p_T < 3$ GeV/c and Fig. (b) is for $3 < p_T < 4$ GeV/c.

shifted comparing to the data. In order to estimate a systematic uncertainty from that source, $nFitPts$ is vary in embedding by ± 1 and ± 2 hits and the total efficiency is recalculated. A maximum difference is taken as a systematic error. The systematic uncertainty on the J/ψ polarization from the tracking efficiency is shown in Tab. 5.5.

Id	Systematic uncertainty source	Systematic uncertainty on λ_θ		
		$2 < p_T < 3$ GeV/c	$3 < p_T < 4$ GeV/c	$4 < p_T < 6$ GeV/c
6	tracking efficiency	0.024	0.009	0.008

Table 5.5: Systematic uncertainty from the tracking efficiency.

5.6 TPC electron identification efficiency

The $n\sigma_e$ cut efficiency is obtained from the Gaussian fit to the $n\sigma_e$ distribution for electrons ($f(n\sigma_e)$) as a fraction of electrons satisfying $-1 < n\sigma_e < 2$ cut:

$$\epsilon_{n\sigma_e}(p) = \frac{\int_{-1}^{2} f(n\sigma_e)}{\int_{-10}^{10} f(n\sigma_e)} \tag{5.1}$$

as it is discussed in Sec. 3.4.2.1. The error on the efficiency is determined from the error on the integral, taking into account correlations between the fitting parameters.

102

Fitting parameters for electrons are found from the analysis of the photonic electron sample. Central values of mean and width of the Gaussian fit are: μ_e = -0.029 $\pm$ 0.022 and σ_e = 0.839 $\pm$ 0.015, respectively. In the analysis, ranges in which the parameters for the electron fit can vary, μ_e and σ_e, are fixed to 3σ around the central values.

The systematic uncertainty on the $n\sigma_e$ cut efficiency is estimated by changing the constraints on the Gaussian fit to $n\sigma_e$ distributions for electrons (Gaussian mean and width) and taking into account errors on the efficiency. Following changes are made to the constraints of the Gaussian fit:

- relaxing limits for the mean and the width - the range for μ_e (σ_e) is chosen so that all μ_e (σ_e) points from the Fig. 5.7 are located within this chosen range; the range for μ_e is (-0.136, 0.141) and for σ_e is (0.753, 0.928)

- fixing the value of the mean and width to:

  - a value obtained from a constant fit to the mean and width points from the Fig. 5.7 without taking into account errors on the points; μ_e = -0.029 and σ_e = 0.839

  - a value obtained from a constant fit to the mean and width points taking into account errors on the points; μ_e = -0.075 and σ_e = 0.861

  - 3σ upper limit for the mean and the width from the constant fit from the Fig. 5.7; μ_e = 0.036 and σ_e = 0.895

  - 3σ lower limit for the mean and the width from the constant fit from the Fig. 5.7; μ_e = -0.094 and σ_e = 0.784

  - 3σ upper limit for the mean and 3σ lower limit for the width from the constant fit from the Fig. 5.7; μ_e = 0.036 and σ_e = 0.784

  - 3σ lower limit for the mean and 3σ upper limit for the width from the constant fit from the Fig. 5.7; μ_e = -0.094 and σ_e = 0.895

The 3σ uncertainty range of the fit functions in Fig. 5.7 is shown as dotted lines.

The range of the uncertainty band is from a minimum and a maximum value of the efficiencies obtained when changing the fitting constraints and taking into account errors on the efficiency. The efficiency with the systematic uncertainty is shown in Fig. 5.8 (the blue shaded area).
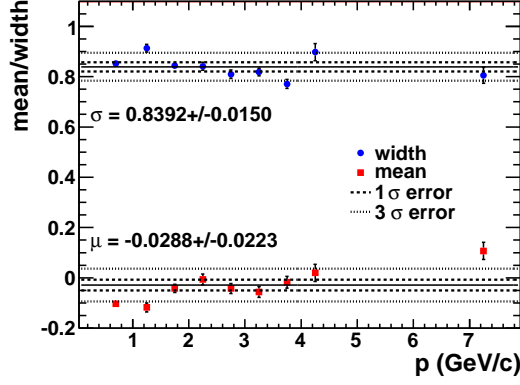
Figure 5.7: Distributions of the mean (red full squares) and width (blue filled circles) of the Gaussian fits to $n\sigma_e$ distributions for photonic electrons as a function of momentum. Dashed lines represent 1σ uncertainty range and dotted lines represent 3σ uncertainty range.
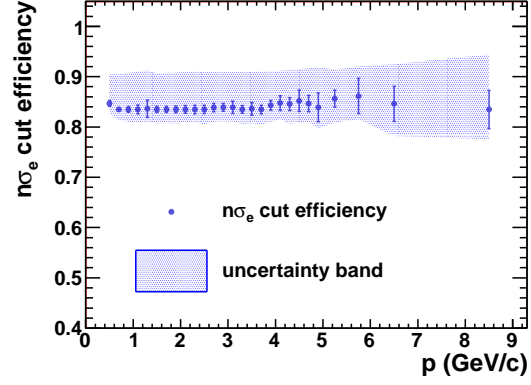
Figure 5.8: $-1 < n\sigma_e < 2$ cut efficiency as a function of momentum (blue full circle) with the uncertainty band (blued shaded area).

Note, that the band's shape does not depend much on the momentum and therefore does not introduce a big systematic uncertainty on the final result, even the uncertainty band may look as a quite big.

A systematic uncertainty on the J/ψ polarization is estimated by shifting $n\sigma_e$ cut efficiency to the minimum and maximum value of the uncertainty band from the Fig. 5.8, in the total efficiency calculations. Then, the polarization parameter is recalculated, and a maximum difference between λ_θ values obtained with changed $n\sigma_e$ cut efficiency and the central value of the λ_θ is taken as a systematic uncertainty. The systematic uncertainty on the J/ψ polarization is shown in a table 5.6.

Id	Systematic uncertainty source	Systematic uncertainty on λ_θ		
		$2 < p_T < 3$ GeV/c	$3 < p_T < 4$ GeV/c	$4 < p_T < 6$ GeV/c
7	$n\sigma_e$ cut efficiency	0.009	0.006	0.012

Table 5.6: Systematic uncertainty from the $n\sigma_e$ cut efficiency.

5.7   TOF matching efficiency

The TOF matching efficiency for single electrons is applied in the analysis as a function of η, integrated over the p_T ($0.4 \leq p_T < 1.4$ GeV/c) and over the full ϕ range, see Sec. 3.4.2.2. As it was shown before, the efficiency does not depend on p_T, but it does depend on ϕ. The matching efficiency as a function of η in three ϕ bins is shown in Fig. 3.41. A systematic uncertainty on the J/ψ polarization, from the first source, is estimated by applying the TOF matching efficiency in the total efficiency calculation as a function of η in the three ϕ bins.

The second source of systematic uncertainty which is taken into account, are errors on the matching efficiency. The error on the matching efficiency includes the statistical error and the uncertainty on the scale parameter, they are treated as uncorrelated.

Both sources of systematic uncertainties are treated as uncorrelated and the systematic uncertainty on the J/ψ polarization from the uncertainty of the TOF matching efficiency is shown in a table 5.7.

Id	Systematic uncertainty source	Systematic uncertainty on λ_θ		
		$2 < p_T < 3$ GeV/c	$3 < p_T < 4$ GeV/c	$4 < p_T < 6$ GeV/c
8	TOF matching efficiency	0.055	0.013	0.003

Table 5.7: Systematic uncertainty from the TOF matching efficiency.

5.8 $1/\beta$ cut efficiency

The method of calculation the efficiency of the $|1/\beta - 1| \leq 0.03$ cut is described in Sec. 3.4.2.2. The $1/\beta$ cut efficiency of 95.70 % is used in the total efficiency calculation.

In order to estimate a systematic uncertainty on the J/ψ polarization from the $1/\beta$ cut efficiency two sources are taken into account. The first source is the uncertainty on the efficiency from the fitting, the error on the fit parameter is 0.26 %. The systematic uncertainty on the J/ψ polarization from this source is negligible. The second source is the different method of calculating the $1/\beta$ cut efficiency. The efficiency can be obtained from the Gaussian fit to the $1/\beta$ distribution (shown in Fig. 5.9), in the whole momentum range where the $1/\beta$ cut is used:
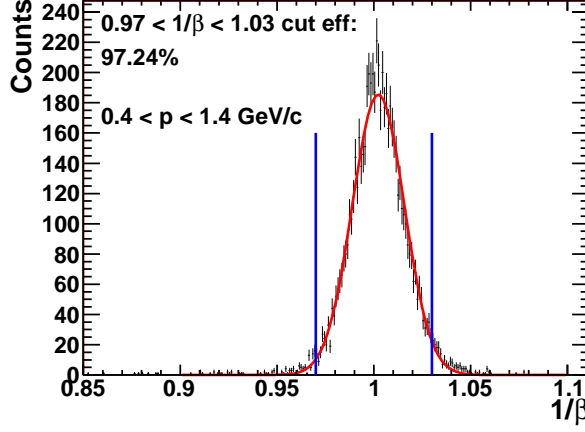
Figure 5.9: The $1/\beta$ distribution from the data in black for $0.4 \leq p < 1.4$ GeV/c with the Gaussian fit in red. The cut efficiency $1/\beta$ from the Gaussian fit is 97.3%. Vertical lines represent the cut range.

$0.4 \leq p < 1.4$ GeV/c. The efficiency obtained in this way is 97.24%, see Fig. 3.43. This value, instead of 95.70 %, is applied to the total efficiency calculation in order to estimate the systematic uncertainty on the final result of the J/ψ polarization.

The systematic uncertainty on the J/ψ polarization arising from the $1/\beta$ cut efficiency is shown in a table 5.8.

Id	Systematic uncertainty source	Systematic uncertainty on λ_θ		
		$2 < p_T < 3$ GeV/c	$3 < p_T < 4$ GeV/c	$4 < p_T < 6$ GeV/c
9	$1/\beta$ cut efficiency	0.015	0.012	0.014

Table 5.8: Systematic uncertainty from the $1/\beta$ cut efficiency.

5.9 TPC pointing resolution effect on the BEMC matching

In the embedding and the data analysis reconstructed in the TPC tracks are matched do the BEMC detector and a tower that the track projects to is considered. Due to the TPC pointing resolution a matched BEMC tower could be a tower which is adjacent to the one that a track really hit. In order to estimated an effect on the final result of potentially different TPC pointing resolution in the embedding and in the data, Monte Carlo tracks (instead of the reconstructed
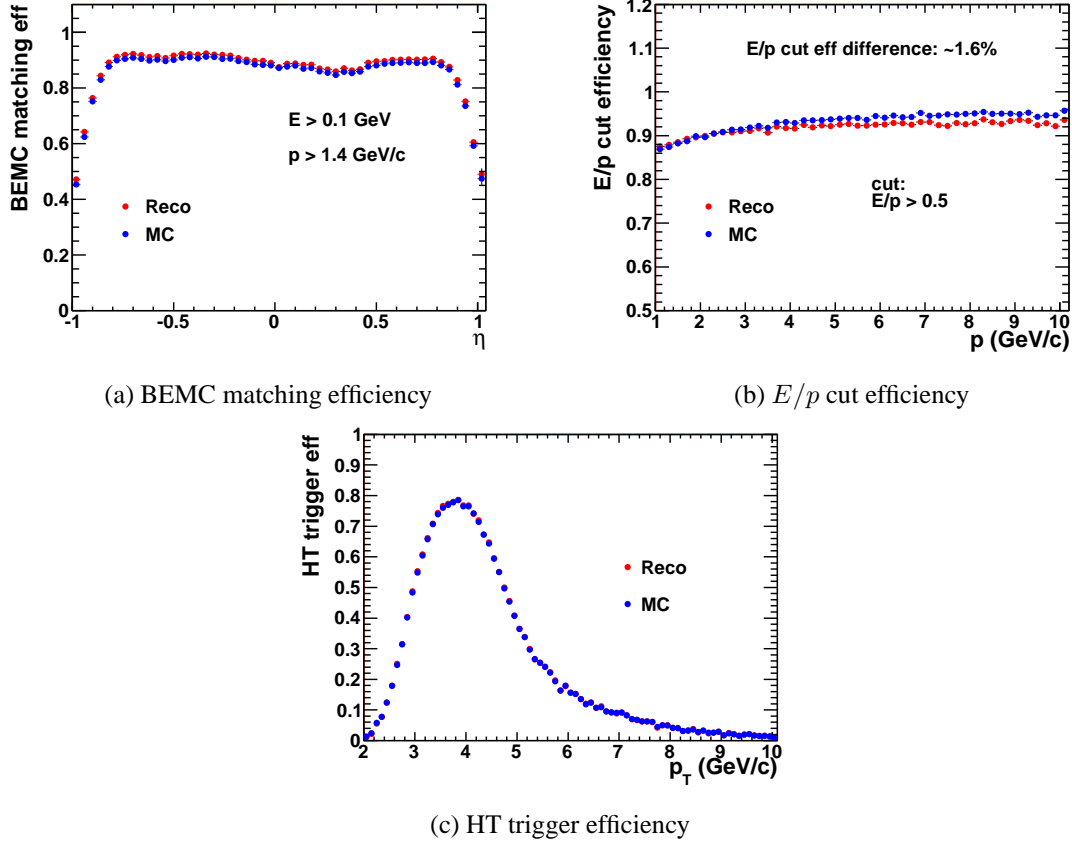
(a) BEMC matching efficiency

(b) E/p cut efficiency

(c) HT trigger efficiency

Figure 5.10: BEMC distributions from the simulation for reconstructed tracks matched do the BEMC in red and for Monte Carlo tracks matched to the BEMC in blue. Figure (a) shows the matching efficiency (with $E > 100$ MeV) as a function of η for $p > 1.4$ GeV/c, Fig. (b) shows the E/p cut efficiency as a function of momentum and Fig. (c) shows the HT trigger efficiency as a function of p_T.

tracks) in embedding are projected to the BEMC. In case when a MC track is matched to the BEMC, a different tower than in the case of the reconstructed track can be chosen. This tower will have different energy deposited in it, which will influence the BEMC matching efficiency, the E/p cut efficiency and the efficiency of the HT trigger.

Figure 5.10 shows the BEMC matching efficiency, the E/p cut efficiency and the HT trigger efficiency for single electrons from the embedding, reconstructed tracks are in red and Monte Carlo tracks are in blue. The BEMC matching efficiency includes the cut on BEMC energy $E > 0.1$ GeV, the matching is shown as a function of η for $p > 1.4$ GeV/c. The E/p cut efficiency is calculated by applying the $E/p > 0.5$ cut in the embedding analysis. The HT trigger efficiency from the embedding is calculated as a fraction of electrons from the J/ψ decay that satisfy the trigger conditions, i.e. pass dsmAdc cut. There is almost no difference for the

HT trigger efficiency, the BEMC matching efficiency is a bit higher for reconstructed than for Monte Carlo tracks matched do the BEMC, and in a case of the E/p cut efficiency there is a small difference of about 2% for higher momenta.

Table 5.9 show systematic uncertainties on the J/ψ polarization from the TPC pointing resolution effect on the BEMC matching.

Id	Systematic uncertainty source	Systematic uncertainty on λ_θ		
		$2 < p_T < 3$ GeV/c	$3 < p_T < 4$ GeV/c	$4 < p_T < 6$ GeV/c
10	TPC pointing resolution	0.008	0.002	0.007

Table 5.9: Systematic uncertainty from the TPC effect on the BEMC matching.

5.10 E/p cut efficiency

In total efficiency calculation, the $E/p > 0.5$ c cut (E is energy from a single BEMC tower that a track projects to) is applied in the embedding analysis code, for $p > 1.4$ GeV/c. In order to account for differences between the simulated BEMC response and BEMC response during the data taking, the E/p cut efficiency is calculated from the data. A pure electron sample is used which is obtained by selecting photonic electrons. Following cuts are applied: -0.2 $< n\sigma_e < 2$ and invariant mass of a pair less than 15 MeV/c^2. Figure 5.11 shows E/p distributions for electrons from the embedding in red and the data in blue for two momentum bins. Some discrepancies are visible.

The E/p cut efficiency for single electrons, which is shown in Fig. 5.12a, is calculated from the data as a fraction of electrons matched to the BEMC that satisfy the $E/p > 0.5$ cut. For $p > 2.7$ GeV/c a constant functions is fitted. The efficiency obtained from the fit is 97.6 $\pm$ 0.3 %. For lower momenta there is a p dependence of the cut efficiency. Figure 5.12b shows the E/p cut efficiency obtained from the embedding, which is $\sim$ 5%. lower.

A systematic uncertainty on the J/ψ polarization is estimated by applying the E/p cut efficiency obtained from the data, instead of directly applying the cut in the embedding analysis. For $1.4 < p < 3$ GeV/c the efficiency from the distribution in 5.12a is applied, for $p > 3$ GeV/c

(a) $1.5 < p < 2$ GeV/c

(b) $3.5 < p < 4$ GeV/c
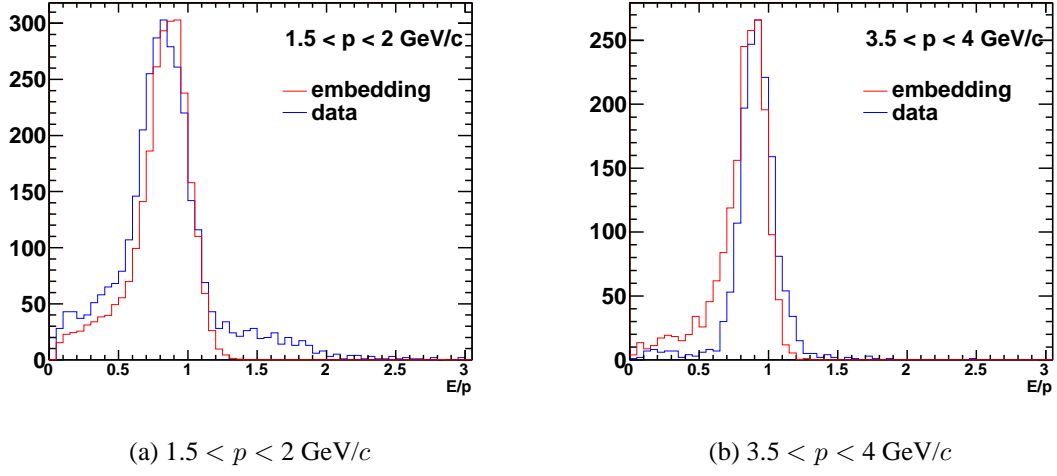
Figure 5.11: Electrons E/p distributions from the embedding in red and the data in blue. Figure (a) is for $1.5 < p < 2$ GeV/c and Fig. (b) is for $3.5 < p < 4$ GeV/c.

(a) Data

(b) Simulation
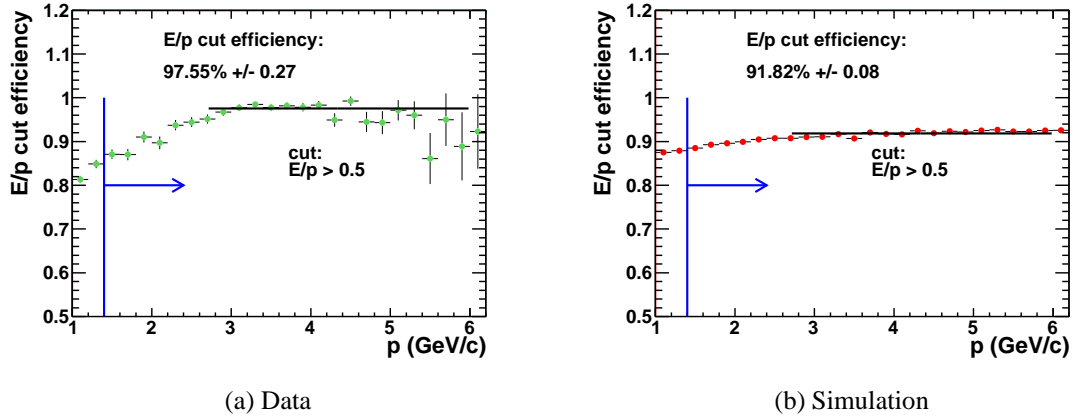
Figure 5.12: The $E/p > 0.5$ cut efficiency from the data, Fig. (a), and from the simulation, Fig. (b). For $p > 3$ GeV/c a constant function is fitted. The vertical line represents the p range where the cut is used.

the efficiency from the constant fit is taken.

Table 5.10 shows the systematic uncertainty on the J/ψ polarization.

Id	Systematic uncertainty source	Systematic uncertainty on λ_θ		
		$2 < p_T < 3$ GeV/c	$3 < p_T < 4$ GeV/c	$4 < p_T < 6$ GeV/c
11	E/p cut efficiency	0.034	0.024	0.068

Table 5.10: Systematic uncertainty from the E/p cut efficiency.

5.11 HT trigger efficiency

In the data analysis the trigger simulator is used in order to decide if an electron fired the HT trigger. The decision is based on dsmAdc value in a BEMC tower. The BHT0*VPDMB*!BHT2 trigger requirement is $11 < dsmAdc \leq 18$. The same dsmAdc cut was applied in the embedding analysis code for the total efficiency calculation. In order to estimated a systematic error on the HT trigger efficiency Adc and dsmAdc distributions from the data and embedding are compared to check if the simulation represents the data well.

Figure 5.13 shows dsmAdc distribution from the data in blue and from the embedding in red. The data distribution is for all electrons, the second peak is for electrons that fired the trigger, the first one in for other electrons that did not fire the trigger. The embedding distribution is for electrons that fired the trigger (passed the dsmAdc cut) and with $2 < p_T < 5$ GeV/c. There is a good agreement between dsmAdc distributions from the data and the embedding. As it can be also seen in Fig. 5.14 which shows dsmAdc for electrons that fired the trigger in two p_T bins: 2 $< p_T < 3$ GeV/c and $3 < p_T < 4$ GeV/c.

Adc distributions from the data and embedding also agree with each other quite well. Figure 5.16b shows Adc distributions from the data and the embedding. Again, the data distribution is for all electrons and the embedding distribution is for electrons that fired the trigger. When we compare the distribution is narrower p_T bin, small differences in distributions' means are visible. Adc distributions for the data and embedding, for electrons that fired the HT trigger, are shown in Fig. 5.16 for two p_T bins: $2 < p_T < 3$ GeV/c and $3 < p_T < 4$ GeV/c. The difference between the data and embedding distributions are extracted by fitting Gaussian functions to the
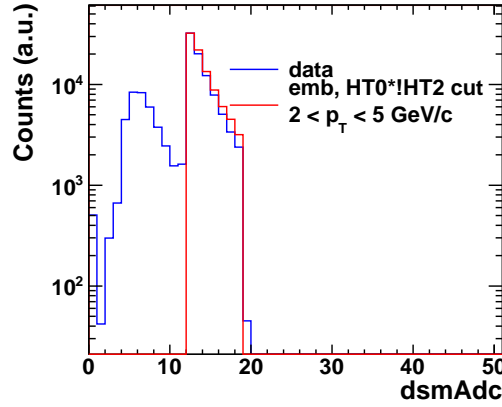
Figure 5.13: dsmAdc distribution from the data in blue and from the simulation in red. The data distribution is for all electrons, the simulated distribution is for electrons that fired the HT trigger.

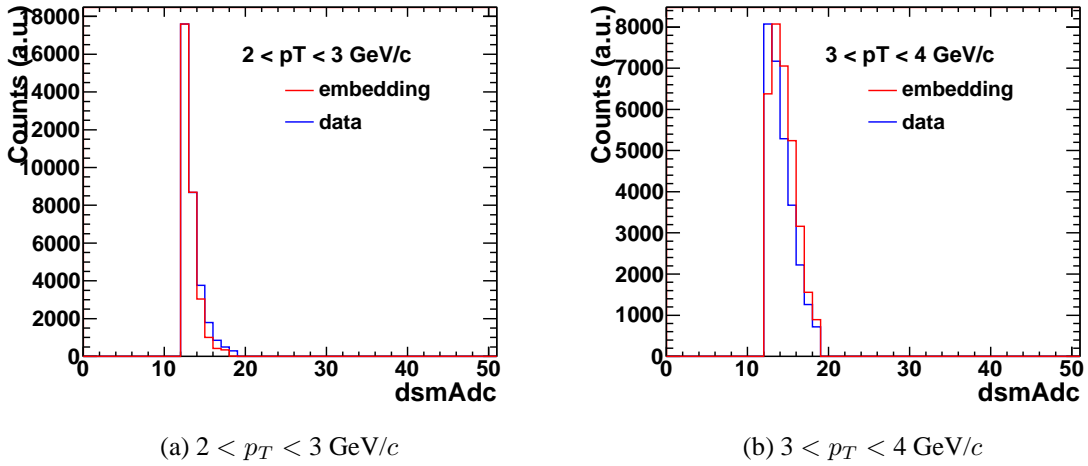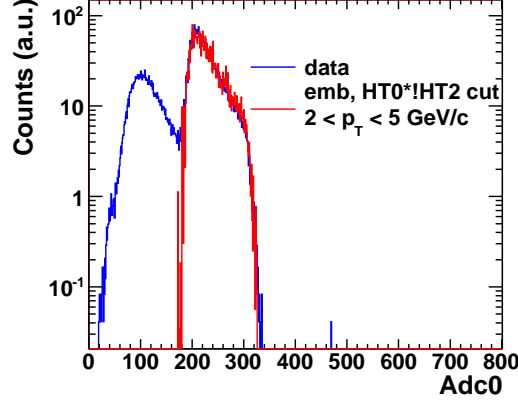(a) $2 < p_T < 3$ GeV/c

(b) $3 < p_T < 4$ GeV/c

Figure 5.14: dsmAdc distributions for electrons that fired the HT trigger from the data in blue and the simulation in red. Figure (a) is for $2 < p_T < 3$ GeV/c and Fig. (b) is for $3 < p_T < 4$ GeV/c.

Figure 5.15: Adc distributions from the data in blue and from the simulation in red. The data distribution is for all electrons, the simulated distribution is for electrons that fired the HT trigger.

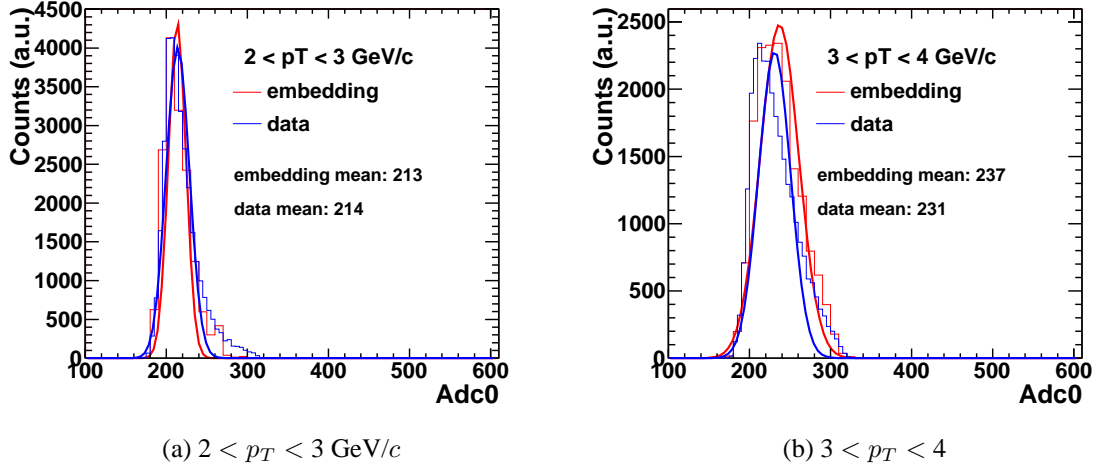(a) $2 < p_T < 3$ GeV/c

(b) $3 < p_T < 4$

Figure 5.16: Adc distributions for electrons that fired the HT trigger from the data in blue and the embedding in red. Figure (a) is for $2 < p_T < 3$ GeV/c and Fig. (b) is for $3 < p_T < 4$ GeV/c.

Adc distributions. The maximum difference between Gaussian functions means is $\sim 3\%$.

Since dsmAdc only takes integer values from the small range of $11 < dsmAdc \leqslant 18$, it is hard to account for small differences between the data and the embedding in dsmAdc. Therefore, in order to estimate the systematic uncertainty, Adc cut in the embedding and the data analysis is applied in addition to the dsmAdc cut and varied. Adc cut that corresponds to the dsmAdc cut is $180 \leq Adc0 \leq 330$. Then the lower and upper thresholds of the Adc cut are also varied by $\pm$ 3%, which corresponds to the biggest difference between means of Adc distributions from the data and embedding. The maximum deviation from the central value of the polarization parameter is considered as a systematic uncertainty on the J/ψ polarization. The

systematic uncertainty on the J/ψ polarization is shown in Tab. 5.11.

Id	Systematic uncertainty source	Systematic uncertainty on λ_θ		
		$2 < p_T < 3$ GeV/c	$3 < p_T < 4$ GeV/c	$4 < p_T < 6$ GeV/c
12	HT trigger efficiency	0.049	0.006	0.003

Table 5.11: Systematic uncertainty from the HT trigger efficiency.

5.12 Summary

Values of λ_θ are:

- $2 < p_T < 3$ GeV/c

  - $\lambda_\theta = 0.145 \pm 0.331$ (stat.) ± 0.350 (sys.)

- $3 < p_T < 4$ GeV/c

  - $\lambda_\theta = \text{-}0.476 \pm 0.158$ (stat.) ± 0.143 (sys.)

- $4 < p_T < 6$ GeV/c

  - $\lambda_\theta = \text{-}0.617 \pm 0.179$ (stat.) ± 0.076 (sys.)

In a table 5.12 the systematic uncertainties on λ_θ are summarised. The uncertainties are symmetric. It is assumed that all described sources of systematic uncertainties are uncorrelated and the final systematic uncertainty is calculated by adding all contributions in quadrature.

Id	Systematic uncertainty source	Systematic uncertainty on λ_θ		
		$2 < p_T < 3$ GeV/c	$3 < p_T < 4$ GeV/c	$4 < p_T < 6$ GeV/c
1	polarization from the simulated lineshape	0.270	0.135	0.003
2	weighting of the input J/ψ p_T shape	0.018	0.007	0.019
3	weighting of the input J/ψ y shape	0.043	0.002	0.014
4	input J/ψ polarization	0.184	0.018	0.013
5	errors from the simulation	0.077	0.028	0.004
6	tracking efficiency	0.024	0.009	0.008
7	$n\sigma_e$ cut efficiency	0.009	0.006	0.012
8	TOF matching efficiency	0.055	0.013	0.003
9	$1/\beta$ cut efficiency	0.015	0.012	0.014
10	BEMC pointing resolution	0.008	0.002	0.007
11	E/p cut efficiency	0.034	0.024	0.068
12	HT trigger efficiency	0.049	0.006	0.003
	Total	0.350	0.143	0.076

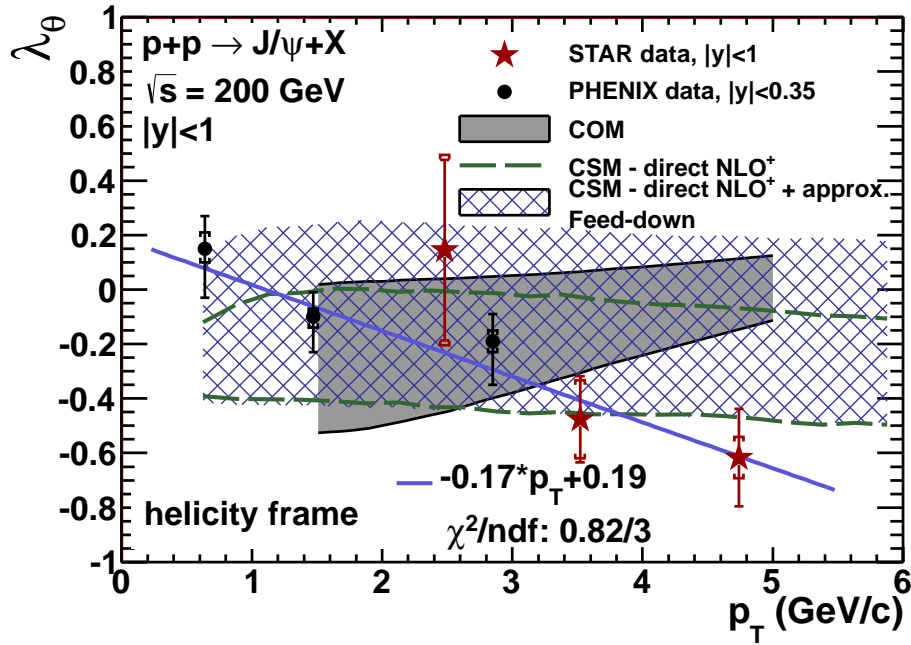Table 5.12: Systematic uncertainties.

Chapter 6

Conclusions

Figure 6.1: The polarization parameter λ_θ as a function of J/ψ p_T (red stars) for $|y| < 1$ in p+p collisions at $\sqrt{s} = 200$ GeV. The result is compared with two model predictions: NLO^+ Color Singlet Model (CSM) (green dashed lines represent a range of λ_θ for the direct J/ψ and hatched blue band is an extrapolation of λ_θ for the prompt J/ψ) [27] and NRQCD calculations with color octet contributions (COM) [47] (gray shaded area). For a comparison the PHENIX result is shown as black filled circles [32]. The blue solid line represents a linear fit to the RHIC results.

In this work a first measurement of the J/ψ polarization, λ_θ, in the STAR experiment is shown. J/ψ polarization is measured in $p + p$ collisions at $\sqrt{s} = 200$ GeV in the helicity frame at $|y| <$

1 and $2 < p_T < 6$ GeV/c. The analysis is done for the inclusive J/ψ production, the analyzed sample includes directly produced J/ψ as well as the J/ψ from the feed-down from the higher excited states, χ_C and ψ', and from the B meson feed-down. The direct J/ψ production is 59$\pm$10% [28] of the observed J/ψ.

The measured polarization parameter λ_θ goes towards negative values with increasing p_T, for $p_T > 3$ GeV/c STAR observes longitudinal J/ψ polarization in the Helicity Frame. The STAR result is compared with the low-p_T PHENIX polarization measurement at mid-rapidity [32] for inclusive J/ψ production. The measurements are consistent with each other in the overlapping p_T region. At higher p_T, our result can be compared with the CDF polarization measurement at mid-rapidity for prompt J/ψ at $\sqrt{s} = 1.96$ TeV [35]. At $p_T \sim 5$ GeV/c CDF observes almost no polarization, $\lambda_\theta \sim 0$ (the polarization becomes slightly longitudinal as p_T increases) while STAR observes a strong longitudinal polarization in that p_T region. However, in terms of x_T ($x_T = 2p_T/\sqrt{s}$) the CDF result at $p_T \sim 5$ GeV/c is comparable with the RHIC result at $p_T < 2$ GeV/c, $x_T \sim 0.2$.

The data are compared with two model predictions for the λ_θ at mid-rapidity: $NLO^+ CSM$ [27] and COM [47]. The $NLO^+ CSM$ model under-predicts the measured J/ψ cross-section [80] but is in agreement with the previous RHIC polarization measurement from the PHENIX experiment [32]. However, the PHENIX measurement is limited to low p_T, where the data are not able to distinguish between the COM and CSM predictions regarding the J/ψ polarization, since models have almost the same predictions. The COM model [47] for directly produced J/ψ, describes observed J/ψ yield [18][35] and J/ψ polarization at low p_T in PHENIX [32] well. However, at high p_T the model predicts different polarization than at low p_T (transverse) [46] and is in disagreement with the result from the CDF experiment [35] at $\sqrt{s} = 1.96$ TeV.

For lower p_T COM and CSM models have similar predictions of longitudinal J/ψ polarization. Thus, it is especially important to measure the J/ψ polarization at higher p_T, where CSM and COM predict different polarization.

In Fig. 6.1 green dashed lines represent a range of λ_θ for the direct J/ψ production from the $NLO^+ CSM$ prediction and an extrapolation of λ_θ for the prompt J/ψ production is shown as the hatched blue band [27]. The $NLO^+ CSM$ shows a weak p_T dependence of λ_θ, and although the data shows a trend of decreasing λ_θ, the STAR result is consistent with the $NLO^+ CSM$ model prediction, within the experimental and theoretical uncertainties.

The prediction of $NRQCD$ calculations with color octet contributions (COM) [47] for

direct J/ψ production, gray shaded area, goes towards the transverse J/ψ polarization as p_T increases. The trend in the data is different, the STAR and PHENIX results go towards the longitudinal J/ψ polarization with increasing p_T. The linear fit (blue line) to the RHIC data has the negative slope parameter of -0.17 $\pm$ 0.05. Thus the trend in the data disfavours the COM.

In order to provide better constraints for the models, further measurements with larger statistics and for J/ψ with higher p_T are essential. An integrated luminosity of the data taken in year 2011 at $\sqrt{s}$ = 500 GeV is much higher than what is used for this analysis. This newer data at $\sqrt{s}$ = 500 GeV will allow to measure J/ψ with p_T up to $\sim$ 15 GeV/c with a reasonable statistics for the J/ψ polarization measurement. The data at $\sqrt{s}$ = 500 GeV may help to further distinguish between the J/ψ production models.

The ongoing STAR upgrade can provide more insight into the J/ψ production and polarization. The Muon Telescope Detector (MTD) and the Heavy Flavor Tracker (HFT) will be installed and gathering data starting in 2014. With the MTD it will be possible to analyzed the J/ψ production via its di-muon decay channel at mid-rapidity. Muons advantage over electrons is that they do not come from the γ conversion, the Dalitz decay contribution is much smaller and they are less affected by radiative losses in the detector material. In addition, the HFT will help to distinguish prompt J/ψ from the non-prompt, from the B decay, using a topological method.

This thesis presents the first STAR measurement of the J/ψ polarization which already sheds some light on the J/ψ production mechanism by discarding the COM. A newer data at $\sqrt{s}$ = 500 GeV, taken in 2011 with much higher luminosity, may help to further distinguish between the J/ψ production models and may allow to perform analysis of the full angular distribution of the leptons from the J/ψ decay and extract the frame invariant parameter. On the theoretical side, one needs to stress that the uncertainties of the models need to be reduced in order to draw more precise conclusions.

Another direction of this analysis is related to the fact that colliding at RHIC protons are polarized. Therefore it would be very interesting, with more statistics, to look at the J/ψ polarization as a function of the polarization of a proton beam. It may allow to further discriminate among the models, which can be sensitive to spin observables that could be measured at STAR, such as beam polarization or correlations of the beam polarization and the direction of the outgoing positron.

Other aspect of the polarization study is an analysis of the J/ψ polarization in high energy

heavy ion collisions, where a formation of a new state of matter, Quark-Gluon Plasma (QGP) is expected. In this case the situations is more complicated. The J/ψ polarization could be modified in the QGP. It was also predicted that in the presence of the QGP, the charmonia production will be suppressed due to the color screening of the binding potential [81]. At RHIC energies the temperature may not be sufficiently high to "melt" the J/ψ state, while excited states χ_C and $\psi^{'}$ are expected to dissociate just above the critical temperature T_C [82]. If the excited states are indeed suppressed in the RHIC heavy ion collisions and J/ψ survives in the QGP, it would allow to analyze the polarization of the direct J/ψ . The J/ψ polarization measurement in heavy ion collisions could also be used as a test of quarkonia sequential suppression. A change of the observed prompt J/ψ polarization from proton-proton to central heavy ion collisions may provide a strong indication for charmonium sequential suppression in the quark-gluon plasma (assuming that J/ψ polarization is not modified by the QGP) [83]. However, more theoretical input is needed for this.

Appendices

Appendix A

$n\sigma_e$ distributions

A.1 $n\sigma_e$ distributions for photonic electrons

Below are shown $n\sigma_e$ distributions for photonic electrons, for different momentum ranges used in the analysis. The black distribution (unlike-like, full circles) is a high purity electron sample which is obtained by subtracting the like-sign distribution from the unlike-sign distribution. The σ_e distribution for electrons (black distribution) is fitted with the Gaussian function (the green function) without any constraints applied on the fit. Obtained values of the μ and σ of the Gaussian fit for electrons are used as constraints for the electron fit in the inclusive electrons analysis.

(a) $0.4 < p < 1$ GeV/c

(b) $1 < p < 1.5$ GeV/c

(c) $1.5 < p < 2$ GeV/c

(d) $2 < p < 2.5$ GeV/c
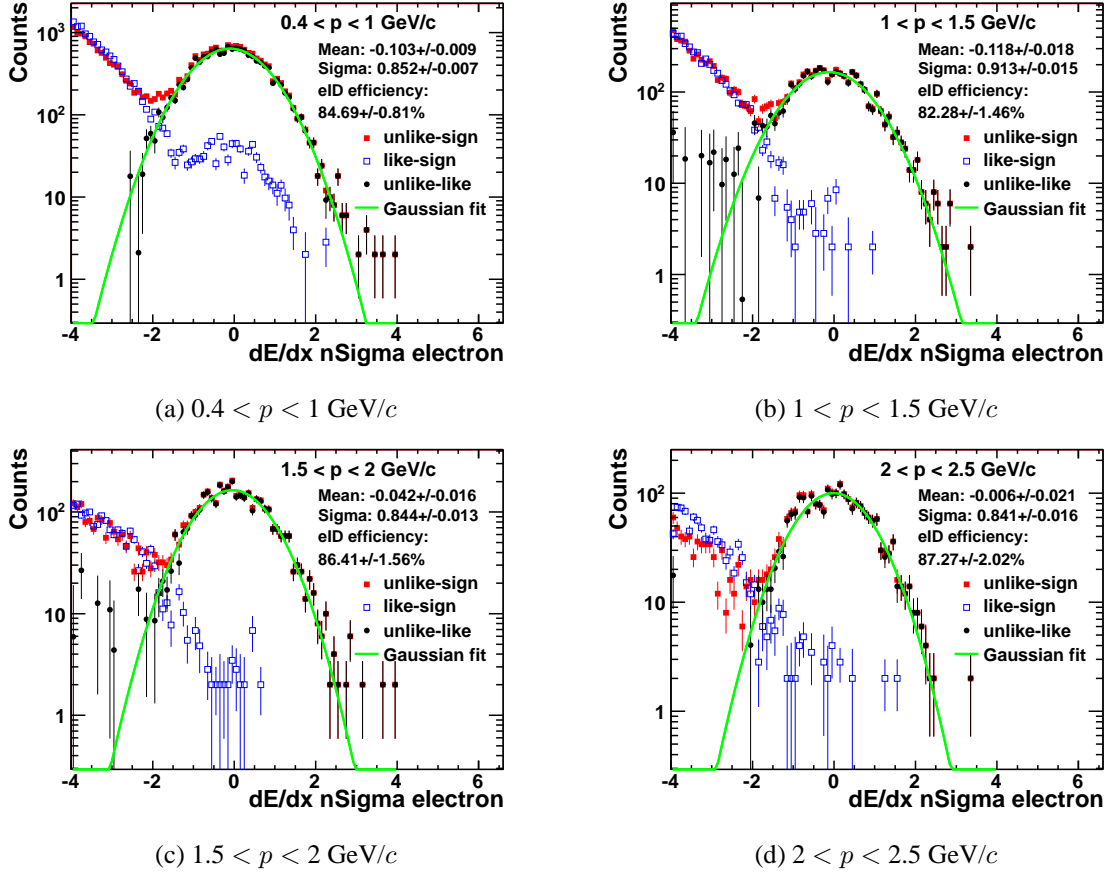
Figure A.1: $n\sigma_e$ distributions for photonic electrons for different momentum ranges. The black distribution is a high purity electron sample (the unlike-sign distribution after the like-sign distribution subtraction) with the Gaussian function fitted

(a) $2.5 < p < 3$ GeV/c

(b) $3 < p < 3.5$ GeV/c

(c) $3.5 < p < 4$ GeV/c

(d) $4 < p < 4.5$ GeV/c

(e) $4.5 < p < 10$ GeV/c
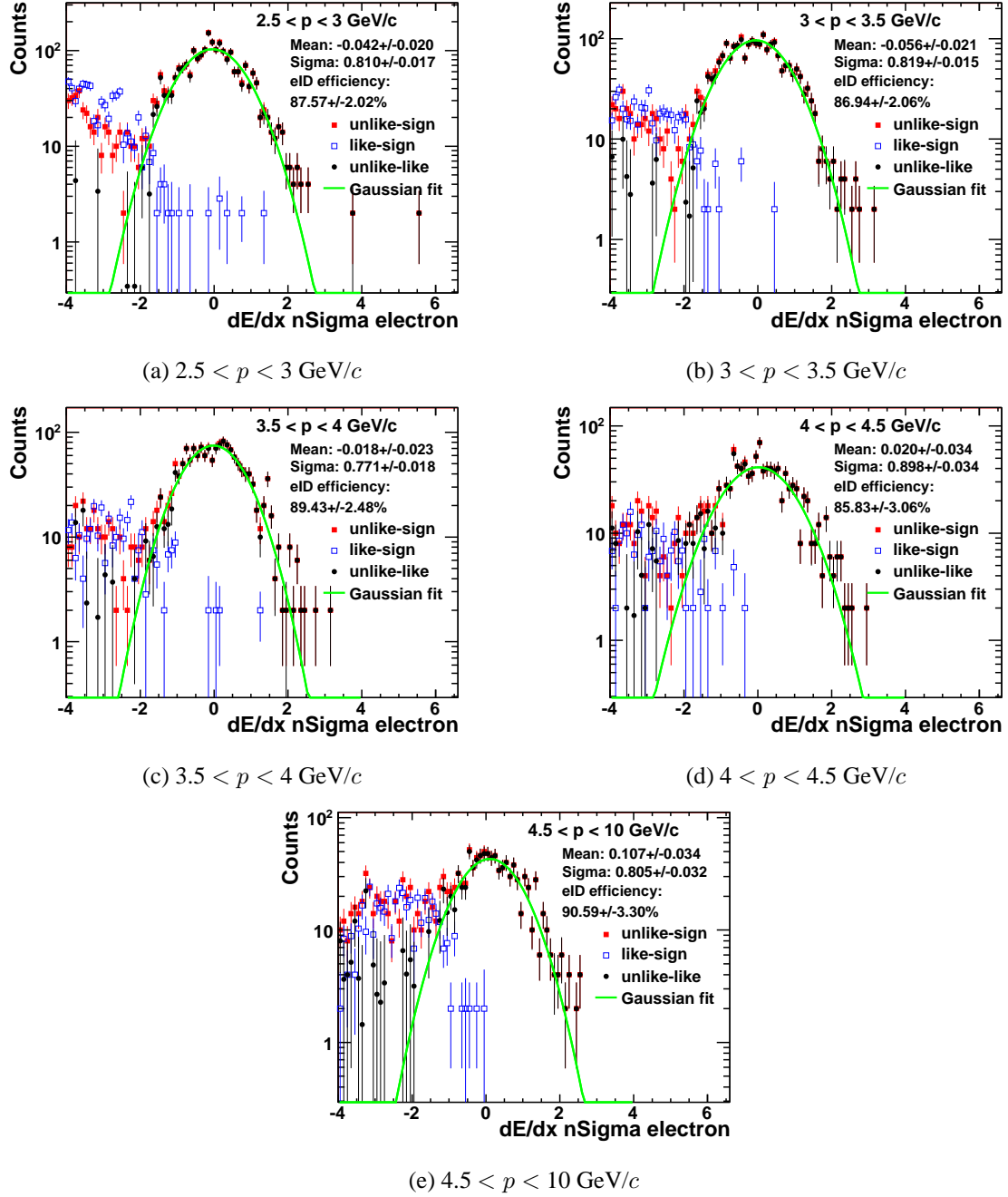
Figure A.2: $n\sigma_e$ distributions for photonic electrons for different momentum ranges. The black distribution is a high purity electron sample (the unlike-sign distribution after the like-sign distribution subtraction) with the Gaussian function fitted

A.2 $n\sigma_e$ multi-Gaussian fit for electrons

Below are shown $n\sigma_e$ distributions particles after TOF and BEMC electron identification cuts. The sum of three Gaussian functions is fitted to the $n\sigma_e$ distribution. The red Gaussian is for electrons, the blue one is for pions and the green Gaussian is for protons, kaons dE/dx merges with other hadrons. Ranges of Gaussian parameters for the electron fit are constrained based on the values obtained in the photonic electrons analysis. Gaussian functions for hadrons are guided using predictions of the Bischel functions.
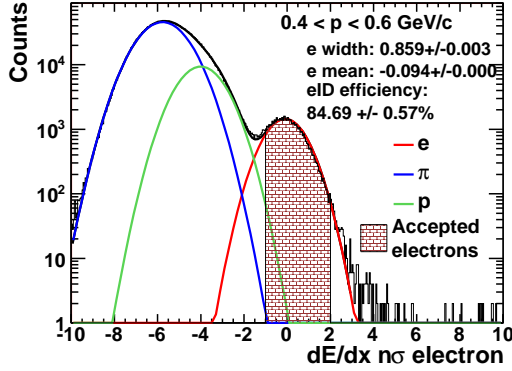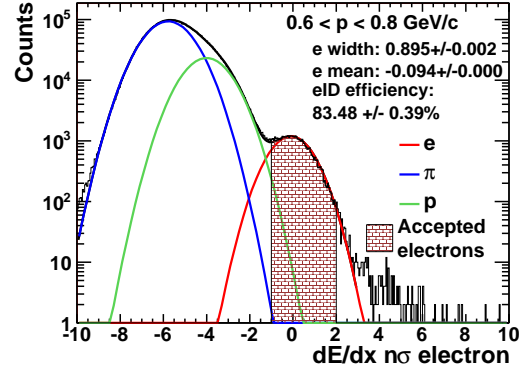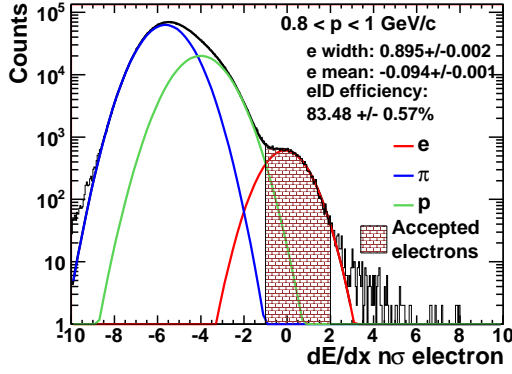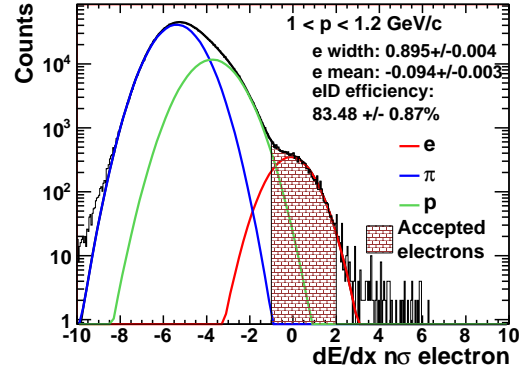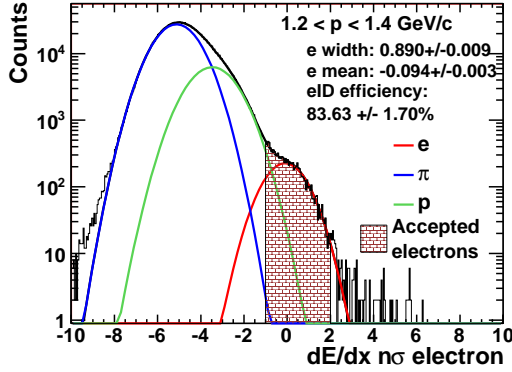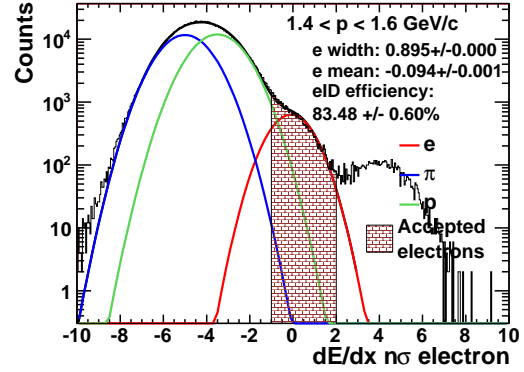
Figure A.3: $n\sigma_e$ distributions in black for different momentum ranges with the sum of three Gaussian functions fitted. The red Gaussian is for electrons, the blue one is for pions and the green Gaussian is for protons, kaons dE/dx merges with other hadrons. The shaded area are electrons after all electron identification cuts.
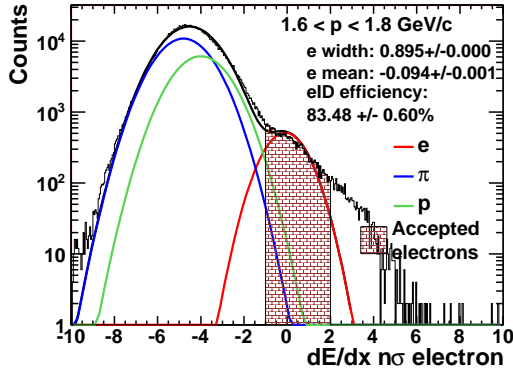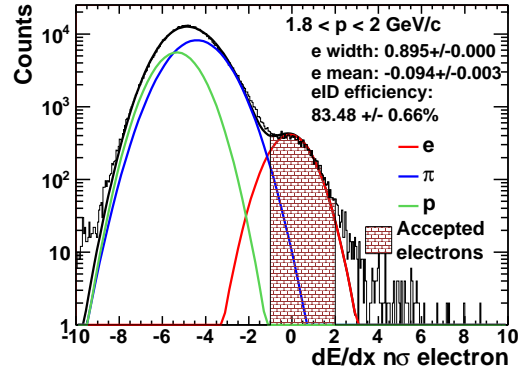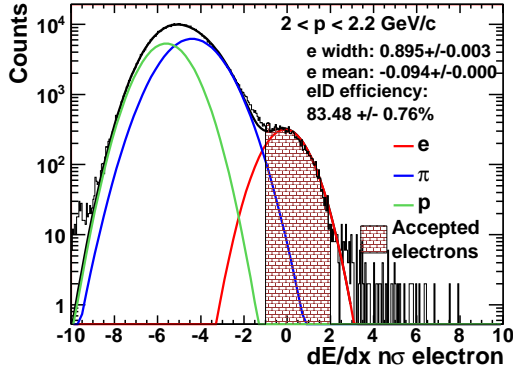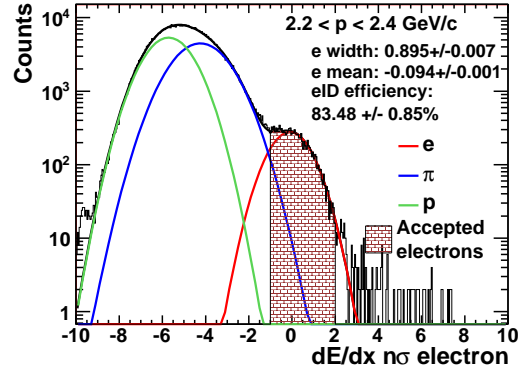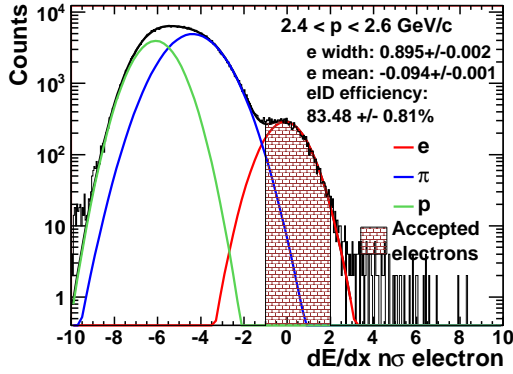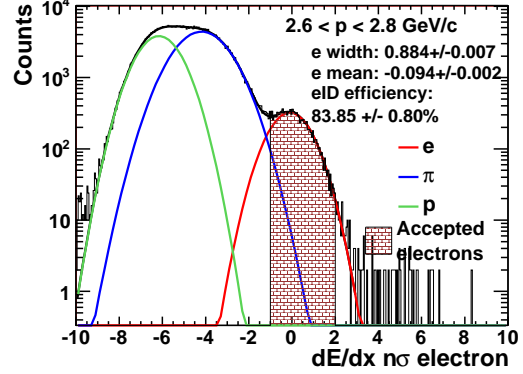
(a) $1.6 < p < 1.8$ GeV/c

(b) $1.8 < p < 2$ GeV/c

(c) $2 < p < 2.2$ GeV/c

(d) $2.2 < p < 2.4$ GeV/c

(e) $2.4 < p < 2.6$ GeV/c

(f) $2.6 < p < 2.8$ GeV/c

Figure A.4: $n\sigma_e$ distributions in black for different momentum ranges with the sum of three Gaussian functions fitted. The red Gaussian is for electrons, the blue one is for pions and the green Gaussian is for protons, kaons dE/dx merges with other hadrons. The shaded area are electrons after all electron identification cuts.

(a) $2.8 < p < 3$ GeV/c

(b) $3 < p < 3.2$ GeV/c

(c) $3.2 < p < 3.4$ GeV/c

(d) $3.4 < p < 3.6$ GeV/c
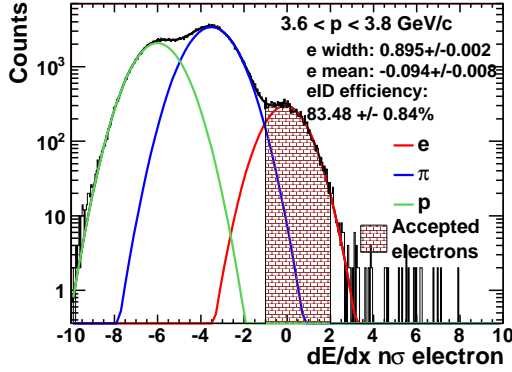
(e) $3.6 < p < 3.8$ GeV/c
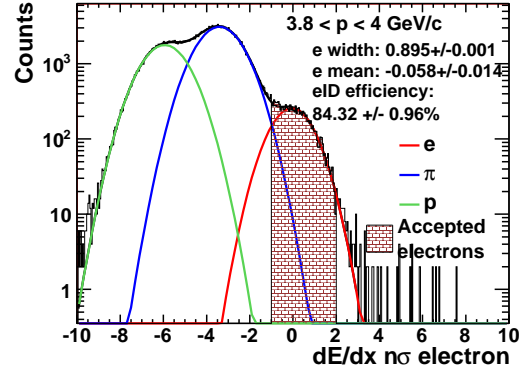
(f) $3.8 < p < 4$ GeV/c

Figure A.5: $n\sigma_e$ distributions in black for different momentum ranges with the sum of three Gaussian functions fitted. The red Gaussian is for electrons, the blue one is for pions and the green Gaussian is for protons, kaons dE/dx merges with other hadrons. The shaded area are electrons after all electron identification cuts.
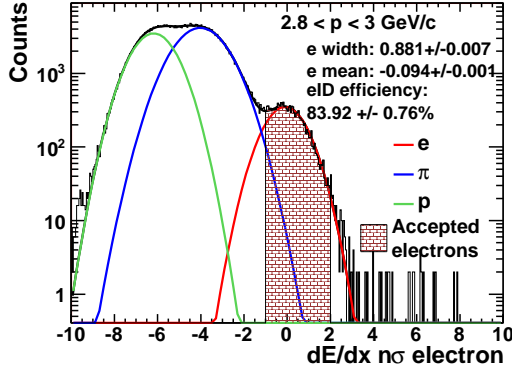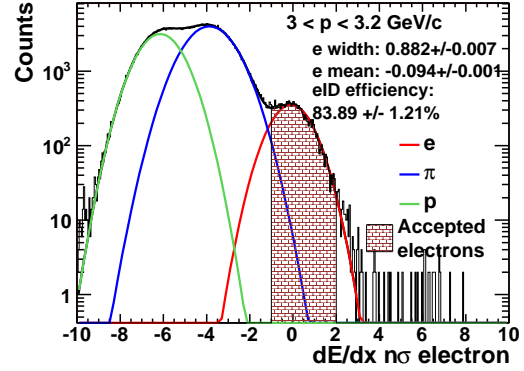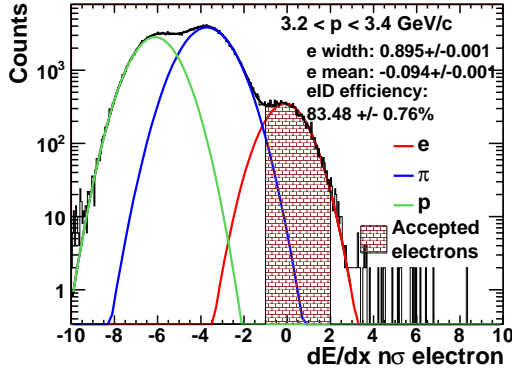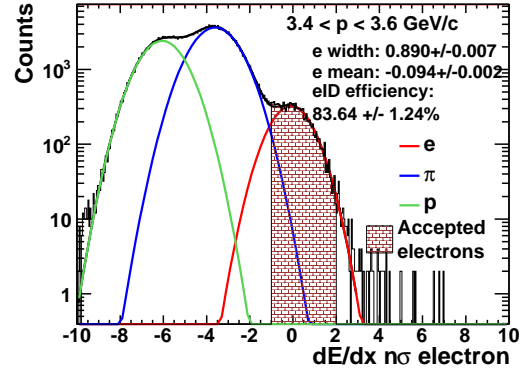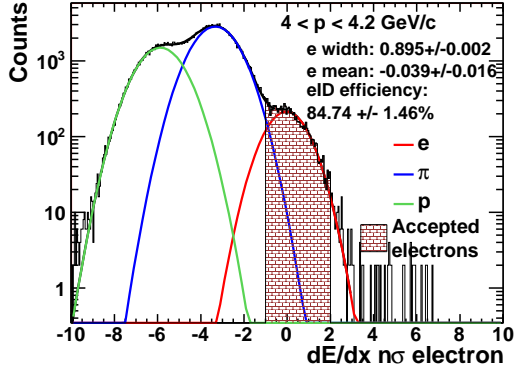
(a) $4 < p < 4.2$ GeV/c
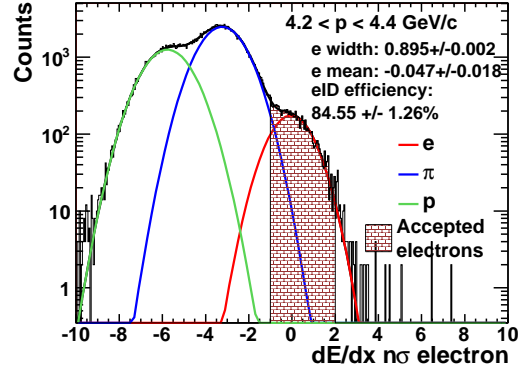
(b) $4.2 < p < 4.4$ GeV/c
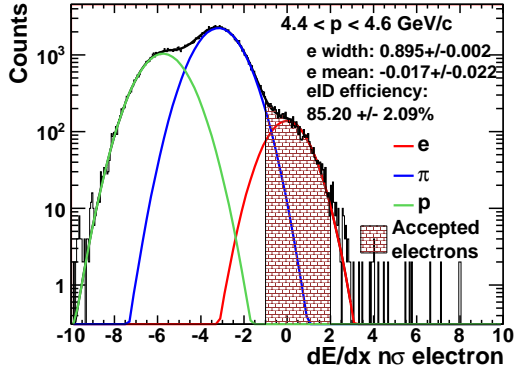
(c) $4.4 < p < 4.6$ GeV/c
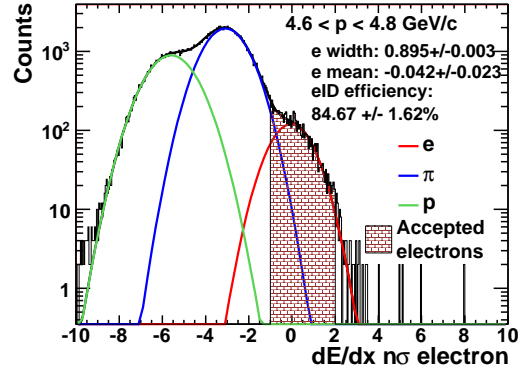
(d) $4.6 < p < 4.8$ GeV/c
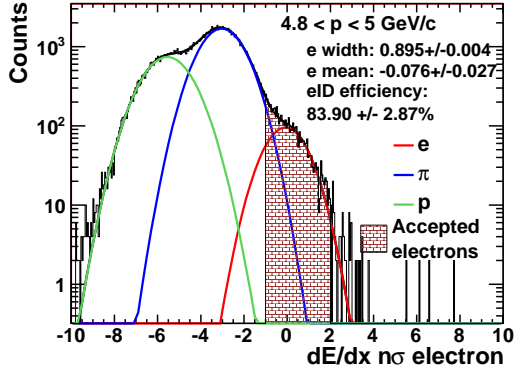
(e) $4.8 < p < 5$ GeV/c
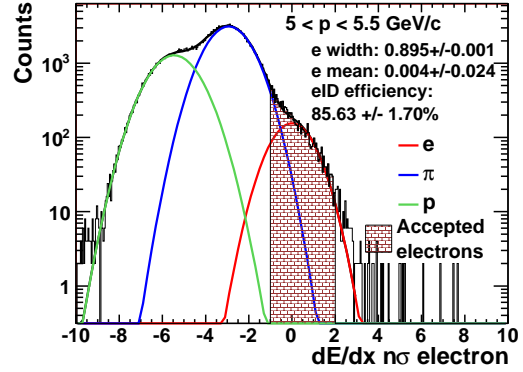
(f) $5 < p < 5.5$ GeV/c

Figure A.6: $n\sigma_e$ distributions in black for different momentum ranges with the sum of three Gaussian functions fitted. The red Gaussian is for electrons, the blue one is for pions and the green Gaussian is for protons, kaons dE/dx merges with other hadrons. The shaded area are electrons after all electron identification cuts.

(a) $5.5 < p < 6$ GeV/c

(b) $6 < p < 7$ GeV/c

(c) $7 < p < 8$ GeV/c
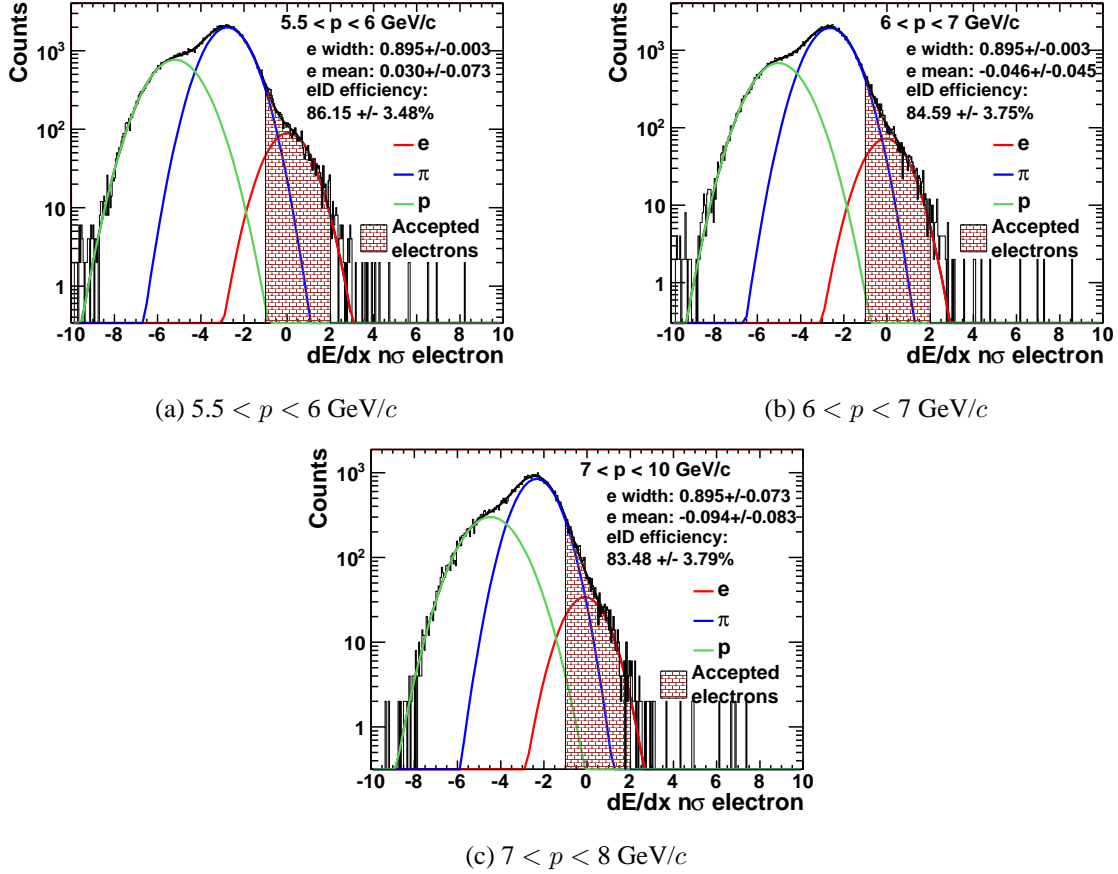
Figure A.7: $n\sigma_e$ distributions in black for different momentum ranges with the sum of three Gaussian functions fitted. The red Gaussian is for electrons, the blue one is for pions and the green Gaussian is for protons, kaons dE/dx merges with other hadrons. The shaded area are electrons after all electron identification cuts.

A.2.1 Gaussian fit parameters

Figure A.8 shows μ, σ and a scale of Gaussian fits for electrons, pions and proton obtained from the fits, as a function of momentum.

(a) Gaussian mean, μ

(b) Gaussian width, σ
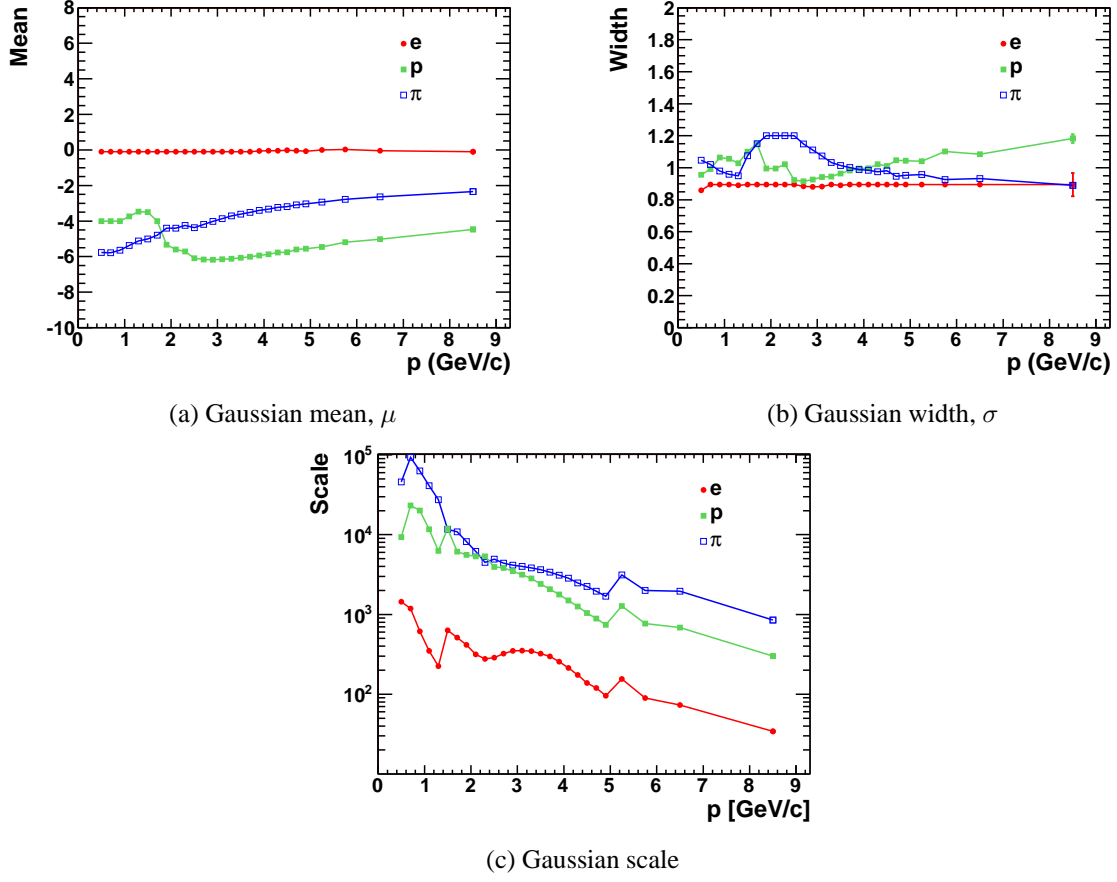
(c) Gaussian scale

Figure A.8: μ, σ and a scale of Gaussian fits for electrons, pions and proton as a function of p.

Appendix B

Signal significance

The signal significance (sig) or the effective signal, S_{eff}, is a useful measure to judge the quality of a signal in the presence of a background. It takes into account both, the signal strength and the background level.

Assume that S is a signal, B is a background and T is total counts, so the actual signal is:

$$S = T - B \tag{B.1}$$

The significance of a signal is commonly expressed as a ratio of the signal to the statistical uncertainty of the signal, and is expressed in terms of σ.

$$sig = S/\delta S \tag{B.2}$$

Assuming that the errors are Gaussian distributed and using Gaussian error propagation the error of S in Eq. B.1 is:

$$\delta S = \sqrt{(\frac{\partial S}{\partial T}\delta T)^2 + (\frac{\partial S}{\partial B}\delta B)^2} = \sqrt{(\delta T)^2 + (\delta B)^2} \tag{B.3}$$

$T = S + B$, $\delta S = \sqrt{S}$ and $\delta B = \sqrt{B}$

$$\delta S = \sqrt{S + 2B} \tag{B.4}$$

So the signal significance is:

$$sig = \frac{S}{\delta S} = \frac{S}{\sqrt{S + 2B}} \tag{B.5}$$

Bibliography

[1] J. Beringer, et al. (Particle Data Group Collaboration), Phys. Rev. D 86, 010001 (2012)

[2] D. H. Perkins, Introduction to High Energy Physics, Cambridge University Press, 2000

[3] G. Sterman et al. Handbook of perturbative QCD, Rev. Mod. Phys., 67(1):157–248 (1995)

[4] S. Eidelman et al. (Particle Data Group Collaboration), Phys. Lett. B 592, 1 (2004)

[5] F. Englert, R. Brout, Phys. Rev. Lett, 13, 321-323 (1964)
      P.W. Higgs, Phys. Rev. Lett. 13, 508-509 (1964)
      G.S. Guralnik, C.R. Hagen, T.W.B. Kibble, Phys. Rev. Lett. 13, 585-587 (1964)

[6] http://home.web.cern.ch/about/updates/2013/03/new-results-indicate-new-particle-higgs-boson

[7] T. Appelquist, A. De Rujula, H. D. Politzer, S.L. Glashow, Phys. Rev. Lett. 34, 365 (1975)

[8] L. Kluber, H. Satz, arXiv:0901.3831/hep-ph

[9] J. J. Aubert et al. (E598 Collaboration), Phys. Rev. Lett. 33, 1404 (1974)

[10] J.E. Augusting et al. (SLAC-SP-017 Collaboration), Phys. Rev. Lett. 33, 1406 (1974)

[11] J.D. Bjorken, S.L. Glashow, Phys. Lett. 11, 255 (1964)

[12] S.L. Glashow, J. Iliopoulos, L. Maiani, Phys. Rev. D 2, 1285 (1964)

[13] F. Karsch, M.-T. Mehr, H. Satz, Z. Phys. C 37, 617 (1988)

[14] S. Jacobs, M. G. Olsson and C. Suchyta, Phys. Rev. 33, 3338 (1986)

[15] S. X. Oda et al., J. Phys. G 35, 104134 (2008)

[16] P. Faccioli et al., J. High Energy Phys. 10, 004 (2008)

[17] F. Abe et al., Phys. Rev. Lett. 79, 578 (1997)

[18] L. Adamczyk, et al. (STAR Collaboration), Phys. Lett. B 722, 55 (2013)

[19] P. Faccioli, C. Laorenco, J. Seixas, H.K. Wohri, Eur. Phys. J. C 69, 657 (2010)

[20] J.P. Lansberg, Int. J. Mod. Phys. A 21, 3857-3916 (2006)

[21] E. Braaten, S. Fleming, T.C. Yuan, Ann. Rev. Nucl. Part. Sci 46, 197 (1996)

[22] E. Braaten, M.A. Donchelski, S. Fleming, M.L. Mangano, Phys. Lett. B 333, 548 (1994)

[23] The CDF Collaboration, arXiv:hep-ex/9412013

[24] J. Campbell, F. Maltoni, F. Tramontano, Phys. Rev. Lett. 98, 252002 (2007)

[25] H. Haberzettl, J.P. Lansberg, Phys. Rev. Lett. 100, 032006 (2008)

[26] J.P. Lansberg, H. Habarzettl, AIP Conf. Proc. 1038, 83 (2008), arXiv:0806.4001[hep-ph]

[27] J.P. Lansberg, Phys. Lett. B 695 (2011) 149-156 and private communication

[28] S.J. Brodsky, J.P. Lansberg, Phys. Rev. D 81 (2010) 051502(R)

[29] A.Adare et al., Phys. Rev. Lett. 98, 232002 (2007)

[30] C.L. da Silva, Nucl. Phys. A 830, 227C (2009)
L.L. Levy, Nucl. Phys. A 830, 353C (2009)

[31] B.I. Abelev, et al. (STAR Collaboration), Phys. Rev. C 80, 41902 (2009)

[32] A. Adare, et al. (PHENIX Collaboration), Phys. Rev. D 82, 012001 (2010)

[33] A. Adare, et al. (PHENIX Collaboration), Phys. Rev. D 85, 092004 (2012)

[34] B. Trzeciak (for the STAR Collaboration), Nucl. Phys. A, 607 (2013), arXiv:1302.7293 [hep-ex]

[35] A. Abulencia, et al. (CDF Collaboration), Phys. Rev. Lett. 99, 132001 (2007)

[36] S. P. Baranov, Phys. Rev. D 66, 114003 (2002)

[37] H. Fritzsch, Phys. Lett. B 67, 217 (1977)

[38] F. Halzen, Phys. Lett. B 69, 105 (1977)

[39] J.F. Amudson, O.J.P. Eboli, E.M. Gregores, F. Halzen, Phys. Lett. B 390, 323 (1997)
A. Brandenburg, O. Nachtmann and E. Mirkes, Z. Phys. C 60 697 (1993)

[40] W.E. Caswell, H.P. Lepage, Phys. Lett. B 167, 437 (1986)

[41] G.T. Bodwin, E. Braaten, G.P. Lepage, Phys. Rev. D 51, 1125 (1995) [Erratum-ibid. D 55, 5853 (1997)]

[42] P.L. Cho, A.K. Leibovich, Phys. Rev. D 53, 150 (1996)

[43] P.L. Cho, A.K. Leibovich, Phys. Rev. D 53, 6203 (1996)

[44] M. Beneke, I.Z. Rothstein, M.B. Wise, Phys. Lett B 408, 373 (1997)

[45] C-Y. Wong, Phys. Rev. D 60, 114025 (1999)

[46] E. Braaten, B.A. Kniehl and J. Lee, Phys. Rev. D, 62, 094005 (2000)

[47] H.S. Chung, C. Yu, S. Kim, J. Lee, Phys. Rev. D 81, 014020 (2010)

[48] P. Cho and M. Wise, Phys. Lett. B 346, 129 (1995)
M. Beneke and I.Z. Rothstein, Phys. Lett. B 372, 157 (1996); 389, 769 (1996);

[49] M. Beneke, M. Kramer, Phys. Rev. D 55, 5269 (1997)

[50] E. Braaren, Y-Q. Chen, Phys. Rev. D 54, 3216 (1996)

[51] A. Leibovich, Phys. Rev. D 56, 4412 (1997)

[52] E. Braaten, B. Kniehl, J. Lee, Phys. Rev. D 62, 094005 (1999)

[53] B. Gong, X.Q. Li, J. Wang, Phys. Lett. B 673, 197 (2009) [Erratum-ibid. B 693, 612 (2010)]

[54] A. Abulencia, et al. (CDF Collaboration), Phys. Rev. D 78, 054006 (2008)

[55] Y.-Q. Ma, K. Wang, and K.-T. Chao, Phys. Rev. D 84, 114001 (2011), and private communication (2012)

[56] M. Butenschon and B. A. Kniehl, Phys. Rev. Lett. 106, 022003 (2011)

[57] Z. Tang (for the STAR Collaboration), J. Phys. G: Nucl. Part. Phys. 38, 124107 (2011), arXiv:1107.0532 [hep-ex]

[58] C.S. Lam, W.K. Tung, Phys. Rev. D 18, 2447 (1978)

[59] J.C. Collins, D.E. Soper, Phys. Rev. D 16, 2219 (1977)

[60] K. Gottfried, J.D. Jackson, Nuovo Cim. 33, 309 (1964)

[61] T. Kempel, arXiv:1107.1293 [nucl-ex]

[62] P. Faccioli, C. Lourenco, J. Seixas, H.K. Wohri, Phys. Rev. Lett. 102, 151802 (2009)

[63] P. Faccioli, C. Lourenco, J. Seixas, Phys. Rev. D 81, 111502(R) (2010)

[64] P. Faccioli, C. Lourenco, J. Seixas, Phys. Rev. Lett. 105, 061601 (2010)

[65] P. Faccioli, C. Lourenco, J. Seixas, H.K. Wohri, Phys. Rev. D 83, 056008 (2011)

[66] K.H. Ackermann, et al. (STAR Collaboration), Nucl. Instrum. Meth. A 499, 624 (2003)

[67] M. Anderson, et al., Nucl. Instrum. Meth. A 499, 659 (2003)

[68] F.Bergsma, et al., Nucl. Instrum. Meth. A 499, 633 (2003)

[69] W.J. Llope for the STAR TOF Group, Nucl. Instrum. Meth. B 241, 306 (2005)

[70] B.Bonner, et al., Nucl. Instrum. Meth. A 508, 181 (2003)
M.Shaom, et al., Nucl. Instrum. Meth. A 492, 344 (2002)

[71] W.J. Llope, et al., Nucl. Instrum. Meth. A 522, 252 (2004)
Jianhang Zhou, Construction of a new detector, and calibration strategies, for start timing in the STAR experiment at RHIC. M.S. thesis, Rice University, 2007 http://drupal.star.bnl.gov/STAR/theses/masters/jianhang-zhou

[72] B.Beddo, et al., Nucl. Instrum. Meth. A 499, 725 (2003)

[73] http://en.wikipedia.org/wiki/Moliere_radius

[74] J. Abele, et al., Nucl. Instrum. Meth. A 499, 692 (2003)

[75] M. Shao, et al., Nucl. Instrum. Meth. A 558, 419 (2006)

[76] GEANT - Detector Description and Simulation Tool, CERN Program Library Long Write-up W5013, 1994

[77] H. Bichsel - Comparison of Bethe-Bloch and Bichsel functions - STAR Note SN0439

[78] T. Ullrich, Z. Xu "Treatment of Errors in Efficiency Calculations", arXiv:physics/0701199v1

[79] D. M. Kaplan et al., Phys. Rev. Lett., 40, 435 (1978)

[80] B. I. Abelev et al., Phys. Rev. C 80, 041902 (2009)

[81] T. Matsui, H. Satz, Phys. Lett. B, 178, 416 (1986)

[82] F. Karsch, D. Kharzeev, H. Satz, Phys. Lett. B 637, 75 (2006)

[83] P. Faccioli, J. Seixas, Phys. Rev. D 85, 074005 (2012)